The Astrophysical Journal, 692:1623–1661, 2009 February 20 doi:10.1088/0004-637X/692/2/1623

DYNAMICAL EVOLUTION OF AGN HOST GALAXIES—GAS IN/OUT-FLOW RATES IN SEVEN NUGA GALAXIES

Sebastian Haan[1,2], Eva Schinnerer[1], Eric Emsellem[3,4,5], Santiago García-Burillo[6], Francoise Combes[7], Carole G. Mundell[8], and Hans-Walter Rix[9]
[1] Max-Planck-Institut für Astronomie (MPIA), Königstuhl 17, 69117 Heidelberg, Germany; haan@mpia.de, schinner@mpia.de
[2] Spitzer Science Center, California Institute of Technology, Pasadenca, CA 91125, USA; haan@ipac.caltech.edu
[3] Université de Lyon, Université Lyon 1, Observatoire de Lyon, 9 avenue Charles André, Saint-Genis Laval, F-69230, France; emsellem@obs.univlyon1.fr
[4] CNRS, UMR 5574, Centre de Recherche Astrophysique de Lyon, France
[5] Ecole Normale Supérieure de Lyon, France
[6] Observatorio Astronomico Nacional (OAN)-Observatorio de Madrid, Alfonso XII, 3, 28014-Madrid, Spain; burillo@oan.es
[7] Observatoire de Paris, DEMIRM, 61 Av. de l Observatoire, 75914-Paris, France; francoise.combes@obspm.fr
[8] Astrophysics Research Institute, Liverpool John Moores University, Twelve Quays House, Egerton Wharf, Birkenhead, CH41 1LD, UK; cgm@astro.livjm.ac.uk
[9] Max-Planck-Institut für Astronomie (MPIA), Königstuhl 17, 69117 Heidelberg, Germany; rix@mpia.de
Received 2008 July 10; accepted 2008 October 15; published 2009 February 24

ABSTRACT

To examine the role of the host galaxy structure in fueling nuclear activity, we estimated gas flow rates from several kpc down to the inner few 10 pc for seven nearby spiral galaxies, selected from the NUclei of GAlaxies sample. We calculated gravitational torques from near-infrared images and determined gas in/out-flow rates as a function of radius and location within the galactic disks, based on high angular resolution interferometric observations of molecular (CO using Plateau de Bure interferometer) and atomic (H I using the Very Large Array) gas. The results are compared with kinematic evidence for radial gas flows and the dynamical state of the galaxies (via resonances) derived from several different methods. We show that gravitational torques are very efficient at transporting gas from the outer disk all the way into the galaxies centers at ∼100 pc; previously assumed dynamical barriers to gas transport, such as the corotation resonance of stellar bars, seem to be overcome by gravitational torque induced gas flows from other nonaxisymmetric structures. The resulting rates of gas mass inflow range from 0.01 to 50 $M_{\odot}$ yr^{-1} and are larger for the galaxy center than for the outer disk. Our gas flow maps show the action of nested bars within larger bars for three galaxies. Noncircular streaming motions found in the kinematic maps are larger in the center than in the outer disk and appear to correlate only loosely with the in/out-flow rates as a function of radius. We demonstrate that spiral gas disks are very dynamic systems that undergo strong radial evolution on timescales of a few rotation periods (e.g., 5×10^8 yrs at a radius of 5 kpc), due to the effectiveness of gravitational torques in redistributing the cold galactic gas.

Key words: accretion, accretion disks – galaxies: active – galaxies: individual (NGC3368, NGC3627, NGC4321, NGC4736, NGC5248, NGC6951, NGC7217) – galaxies: ISM – galaxies: kinematics and dynamics – galaxies: Seyfert – radio lines: galaxies

Online-only material: color figures

1. INTRODUCTION

The study of gas inflow rates has long been recognized to be important for understanding the secular evolution of galaxies, star formation, and nuclear activity. Generally, gas inflow can be caused by two different dynamical mechanisms, gravitational and hydrodynamic mechanisms: galaxy interactions and asymmetries in galactic potentials remove angular momentum through torques, while hydrodynamic mechanisms, such as turbulence in the interstellar medium (ISM), remove angular momentum through gas dynamical effects (e.g., viscous torques or shocks). Here, we focus on the first mechanism with emphasis on the gas response to gravitational torques exerted by the stellar potential. It is well established that asymmetries in galactic potentials, such as large-scale bars, transport gas very efficiently inward (e.g., Mundell & Shone 1999; Combes 2003; Jogee 2006), and that bars can fuel powerful starbursts (e.g., Jogee et al. 2005; Schinnerer et al. 2006; Hunt et al. 2008). Further, the inflow of gas from the outer regions of a galaxy is necessary to maintain nearly constant star formation in the inner disks of spirals (Blitz 1996) and to form (and refuel) an active galactic nuclei (AGN) accretion disk around a central black hole (Rees 1984; Shlosman et al. 1990).

However, searches for low-luminosity AGN fueling mechanisms have not found any strong correlation between the presence of morphological features, e.g., bars and AGN activity (see for a review Combes 2001; Shlosman 2003; Knapen 2005; Jogee 2006). High spatial resolution studies in the near-infrared (NIR) have shown that most galaxies are barred (60%–80%), almost irrespective of their nuclear activity, and that a significant number of Seyfert host galaxies exist in which no bar can be distinguished at practically all length scales (Knapen et al. 2000; Laine et al. 2002). One explanation might be that smaller-scale phenomena are responsible for AGN fueling. Thus, only observations with very high spatial resolution provide the possibility to find correlations between AGN fueling and dynamical perturbations. Martini & Pogge (1999) suggested that nuclear spiral dust lanes may be the channels by which gas from the host galaxy disks is being fed into the central engines. But also a high spatial resolution study with the *Hubble Space Telescope* (*HST*) of the circumnuclear region (on 100 pc scales) has still not found a significant difference between AGN and control samples, at least not for late-type galaxies (Martini et al. 2003; Simões Lopes et al. 2007). Another possibility is that a hierarchy of mechanisms combine to transport the gas from the outer disk (kpc scales) down to the center (pc scales). As these

various mechanisms are working at different spatial scales, also the mass accretion involves different time scales (Shlosman et al. 1990; Combes 2003; Wada & Koda 2004). This time-scale conspiracy could explain the lack of any correlation between the presence of nonaxisymmetric perturbations and the onset of activity (Wada & Koda 2004; García-Burillo et al. 2005). Recent spectroscopic studies of the ionized gas in the central kiloparsec seem to confirm this picture by showing evidence for kinematic perturbations linked with Seyfert galaxies at small radii (Dumas et al. 2007). For larger scales (>1 kpc) first results of a detailed study of H I gas properties for active and nonactive disk galaxies indicate possible relationships between Seyfert activity and H I properties (Mundell et al. 2007; Haan et al. 2008).

As the neutral gas is distributed in a rotating disk and extends out to kpc scales, the problem of radial gas transport is basically a problem of angular momentum removal from the gas. To transfer angular momentum, effective torques are required. In particular, gravitational torques, exerted by the stellar and effective dark matter potential are expected to play a major role (see for an overview Lynden-Bell & Kalnajs 1972). In addition, viscous and magnetic torques might contribute significantly. For example, viscous torques are expected to be very efficient in high gas density regions such as the centers of galaxies (Lynden-Bell 1969; García-Burillo et al. 2005). However, normal viscosity is not efficient, due to the very low density of the gas. Even with macroturbulent viscosity, the time-scales are longer than the Hubble time at large radii, and could be effective only inside the central 1 kpc (Lynden-Bell & Kalnajs 1972). The role of magnetic torques is more uncertain since the interplay between magnetic fields and gas is still not very well understood. Although magnetic fields seem to pervade the interstellar gas in spiral galaxies (Beck et al. 1999; Beck 2004), it is more likely that magnetic fields follow the gas flow rather than acting as incitement.

The quest for a quantitative estimation of radial gas flows from observations has been pursued by different methods: one approach is to use the gas kinematics from radio-interferometric observations of moderately inclined spiral galaxies and a decomposition of the velocity field into Fourier components whose radial variations are used to search for evidence of radial gas flows (e.g., Schoenmakers et al. 1997; Schoenmakers 1999; Jogee et al. 2002b; Fathi 2004; Wong et al. 2004; Krajnović et al. 2006; Trachternach et al. 2009). This method has also been successfully applied using optical spectrography in order to search for perturbations in the stellar dynamics (Dumas et al. 2007; Dumas 2007; Emsellem et al. 2006). Using a slightly different approach, Boone et al. (2007) derived gravitational torques by fitting a model based on analytical solutions for gas particle orbits for the barred spiral galaxy NGC 4569. Spekkens & Sellwood (2007) developed a bisymmetric flow model for noncircular motions that can be fitted to data (applied to the galaxy NGC 2976) by a generalization of the technique developed by Barnes & Sellwood (2003). However, the conversion of the model derived from the velocity field into radial gas flows depends strongly on the chosen model for the gas orbits. As the gas orbits are generally not known, it is impossible to recover the velocity structure from the line-of-sight component of motion alone without further assumptions (e.g., using isophote fits on complementary optical images, Wong et al. 2004).

Another approach for measuring inflow velocities is to derive the gravitational potential on the basis of the observed NIR light distribution of a galaxy and then to compute the gravitational torques exerted by the stellar potential on the gas (Garcia-Burillo et al. 1993; Quillen et al. 1995; García-Burillo et al. 2005).

In combination with observed rotation curves this method does not depend necessarily on assumed mass-to-light ratios (hereafter M/L ratio) which are derived, e.g., by population synthesis techniques, and are inaccurate for the outer disk where dark matter is expected to have a significant contribution. Instead, the azimuthal-averaged calculated velocities from the derivatives of the gravitational potential can be scaled with the actual observed rotation curve and hence allow one to obtain a more realistic scaling of the gravitational potential (assuming a constant azimuthal M/L ratio).

In fact, gravitational torques arise from nonaxisymmetric components of the gravitational potential, such as stellar bars, spirals, and oval distributions. The effect of large-scale bars has been studied in detail by simulations which have successfully shown that bars are very efficient for transporting the gas toward the center (e.g., Sparke & Sellwood 1987; Athanassoula 1992; Shlosman & Noguchi 1993; Heller & Shlosman 1994; Athanassoula 2003). As these mechanisms may work on different spatial scales, secondary bars within large-scale bars (e.g., Shlosman et al. 1989; Friedli & Martinet 1993; Maciejewski & Sparke 2000; Heller et al. 2001; Shlosman & Heller 2002; Englmaier & Shlosman 2004), gaseous spiral density waves (e.g., Englmaier & Shlosman 2000; Maciejewski 2002, 2004a, 2004b), $m = 1$ perturbations (e.g., Shu et al. 1990; Junqueira & Combes 1996; García-Burillo et al. 2000), and nuclear warps (Schinnerer et al. 2000) have been suggested to transport the gas into the center.

In order to distinguish models for nuclear fueling, observations with high angular and velocity resolution are required. Therefore, the IRAM key project NUclei of GAlaxies (NUGA; see García-Burillo et al. 2003) was established—a spectroscopic imaging survey of gas in the centers of nearby low-luminosity AGN. As most of the gas in galaxy nuclei is in the molecular phase, the survey used millimeter CO lines to conduct a detailed mapping of molecular gas dynamics at high resolution (∼0.″5) in the central kiloparsec of AGN hosts. To provide a more complete view of gas dynamics from the outer disk to the center, the H I-NUGA project has been initiated: a spectroscopic imaging survey of the atomic gas distribution and kinematics over the entire galaxy disks (∼25 kpc) for 16 galaxies of the NUGA sample (Haan et al. 2008). Results of this study indicate that the type of nuclear activity (Seyfert/LINER) is linked to the gas distribution in the outer gaseous disk (at several kpc scales), suggesting a time evolution of AGN activity together with the redistribution of the neutral gas due to the nonaxisymmetric potential. As the dominant phase of the neutral ISM transitions from atomic to molecular gas toward the center of galaxies, the combined H I and CO NUGA observations cover all scale lengths from the outer disk at >10 kpc to the center at ∼100 pc.

In this paper, we are studying in detail the gas dynamics and the gas response to the gravitational potential for seven well chosen targets from the H I-NUGA sample. We present a novel approach to derive gas inflow rates via a combination of gravitational torque computation based on the stellar distribution and a kinematic analysis of the observed gaseous velocity fields. To derive gravitational torques, high spatially resolved maps of the stellar and gaseous distribution are required. Therefore, we have obtained for our seven galaxies Very Large Array (VLA) H I data with ∼7″ spatial and ∼10 km s^{-1} velocity resolution. Our sample and the observational setups (H I-, CO-line emission, and NIR data) are described in Section 2. The dynamical models, the geometric disk parameters, and the

Table 1
Sample Overview

Name	RA (J2000)	DEC (J2000)	Hubble Type	AGN HFS	AGN Kewley	v_{sys} (km s^{-1})	Dist (Mpc)
NGC 3368	10 46 46	+11 49 12	SB(rs)ab	L2	L	897	8.1
NGC 3627	11 20 15	+12 59 30	SB(s)b	L/S2	S	727	6.6
NGC 4321	12 22 55	+15 49 21	SB(s)bc	T2	L	1571	16.8
NGC 4736	12 50 53	+41 07 14	(R)S(r)ab	L2	L	308	4.3
NGC 5248	13 37 32	+08 53 08	(R)SB(rs)bc	H	H	1153	15.0
NGC 6951	20 37 14	+66 06 20	SB(rs)bc	S2	S	1424	24.1
NGC 7217	22 07 52	+31 21 33	(R)S(r)ab	L2	L	952	16.0

Notes. Summary of the properties of our seven galaxies. Listed are only parameters from LEDA and NED. The AGN classification listed in Column (6) is taken from Ho et al. (1997): S—Seyfert, L—LINER, T—transition object, H—H II galaxy and NED. In addition, our AGN classification (Haan et al. 2008) in Seyfert and LINER following the method of Kewley et al. (2006) is given in Column (7). The velocities listed in column (8) are the assumed systemic velocities.

amount of noncircular motions are derived in Section 3 from our observed velocity fields using the atomic and molecular gas kinematics. We have computed gravitational torques and estimated their efficiency to transport the gas over galaxy disks on the basis of NIR images (Spitzer, *HST*) and a combination of our H I data and NUGA CO data with ∼0.″5 spatial and ∼5 km s^{-1} velocity resolution. The methods used for this study and its results are described in Section 4. Finally, we compared in Section 5 the total amount of noncircular motions from our observed velocity fields to the noncircular motions that are induced by the gravitational torques and discuss our findings in the context of AGN fueling mechanisms. A summary is given in Section 6.

2. SAMPLE DESCRIPTION AND OBSERVATIONS

For our study we have used observations of the neutral gas component as traced by H I and CO, as well as the stellar component as described in the following.

2.1. Sample Description

For a detailed study of gas inflow rates, we selected seven galaxies from our H I-NUGA sample (Haan et al. 2008). The selection of the targets is based on the presence of bright H I emission as well as a fairly regular H I morphology (i.e., no highly disturbed gas disks). All the galaxies are spiral galaxies ranging in Hubble type from Sa to Sc and are barred, with the exception of NGC 7217. The distance of our sample targets ranges from 4 to 24 Mpc with a mean distance of ∼13 Mpc. A complete overview is given in Table 1. The galaxies host various kinds of nuclear activity:[10] LINERs (four galaxies), Seyferts (two galaxies), and starburst (one galaxy).

2.2. Atomic Gas Data

To trace the dynamics of the outer disk we observed the atomic gas distribution and kinematics in the H I emission line at 21 cm using the NRAO VLA. Previous data obtained with the VLA in C and D array configuration (∼20″ resolution) were already presented by Haan et al. (2008). For the seven galaxies analyzed here we combined these data with newly obtained VLA B-array data resulting in a final resolution of ∼7″. Two galaxies (NGC 3627, NGC 4736) were already observed as part of the THINGS project (Walter et al. 2008). The data reduction was performed using the Astronomical Image Processing System (AIPS; Greisen 2003) following the data reduction scheme of the previous CD array data (Haan et al. 2008). Flux calibrator measurements were performed at the beginning and at the end of each observation cycle. The phase calibrator was observed before and after each source cycle with a maximum angular distance between source and phase calibrator of 12°. The data have an average on-source integration time of 8.5 hr (B-array), 2.7 hr (C-array), and 2.8 hr (D-array). The correlator spectral setup used was set to line mode 4 with Hanning smoothing and 64 channels per 1.5625 MHz channel width per frequency band providing a frequency resolution of 24.414 kHz/channel (∼5.2 km s^{-1}). Calibration solutions were first derived for the continuum data set (inner 3/4 of the spectral band width) and then transferred to the line data. The bandpass solutions were determined from the phase calibrator measurements to account for channel-to-channel variations in phase and amplitude. The B and CD data have been combined. The CLEANing parameters are adjusted to the new combined BCD data, as described in the following. The cell size of each grid was set to 1.″3/pixel with a field of view (FOV) of ∼22′. We produced the CLEANed data cubes using robust weighted imaging with a velocity resolution of ∼10.4 km s^{-1} and an average angular resolution of ∼7″. To find the best compromise between angular resolution and RMS, several robust weighting parameters were tested and a robust parameter of 0.3 was selected. The RMS values and beam sizes are listed in Table 2 with an average achieved RMS value of 0.32 mJy beam^{-1}. The RMS flux sensitivity of 0.4 mJy/beam/channel corresponds to a 3σ detection limit of

Table 2
Parameters of the VLA H I Data

Name	Resolution Beam (″)	Resolution (kpc)	FWZI (km s^{-1})
NGC 3368	6.4 × 5.3	0.23	399
NGC 3627	5.3 × 5.1	0.17	431
NGC 4321	7.6 × 6.5	0.57	291
NGC 4736	5.6 × 5.2	0.11	284
NGC 5248	5.9 × 5.4	0.41	311
NGC 6951	14.4 × 12.5	1.57	338
NGC 7217	7.9 × 5.3	0.50	326

Notes. Overview of the spatial resolution of our VLA observations. The velocity resolution is ∼10.4 km s^{-1} for all galaxies. In addition, the full widths at zero intensity (FWZI) of the H I lines are listed for all galaxies.

[10] The nuclear classification is adopted from Haan et al. (2008) and based on optical emission line ratios following the method of Kewley et al. (2006).

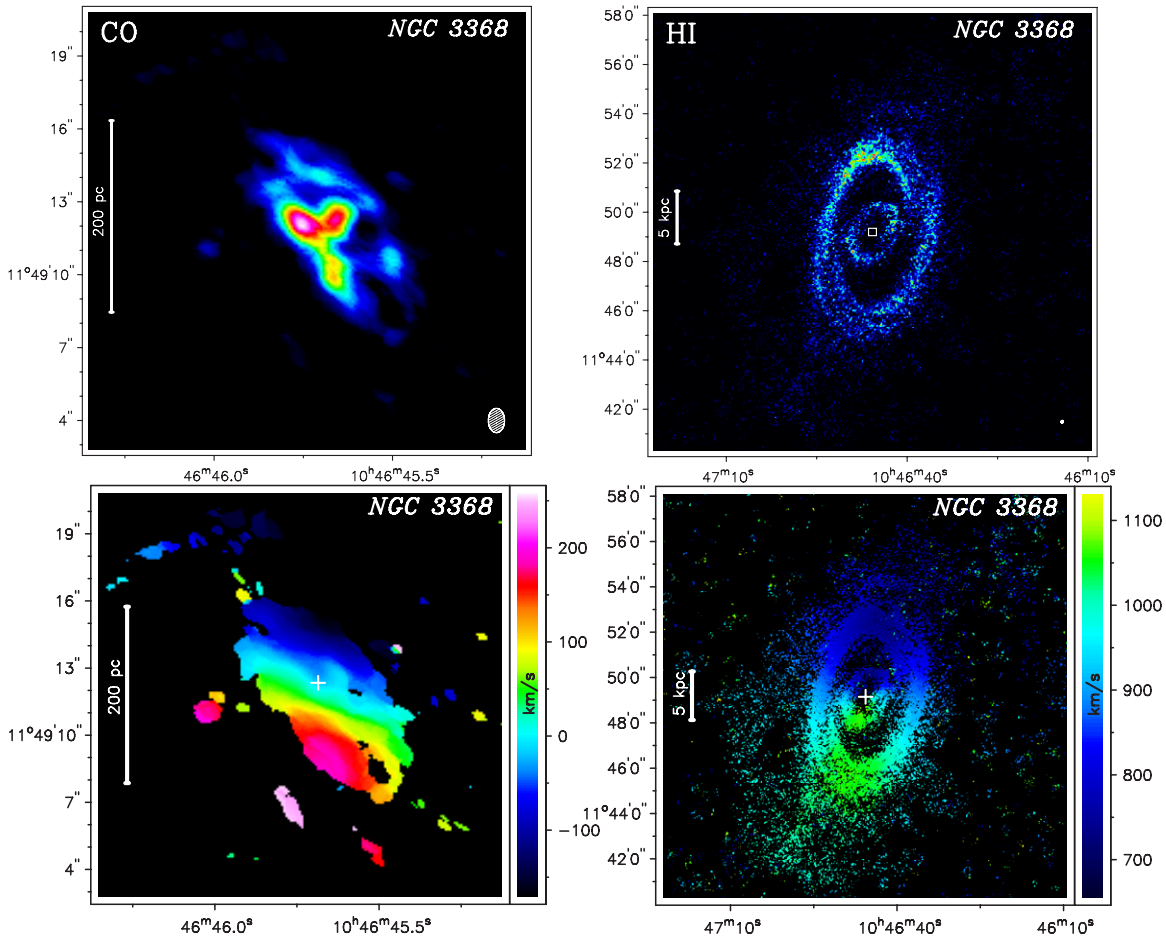

Figure 1. Overview of the intensity maps (top panels) and intensity-weighted velocity fields (bottom panels) for the molecular (left panels) and atomic gas (right panels). The beam is plotted in the bottom left corner and a scale length of 1 kpc (200 pc) is indicated as bar for the H I (CO) maps at the left. Only for NGC 5248 the bar indicates a scale length of 1 kpc for the CO map. The dynamical center is indicated by a cross in the velocity fields (bottom panels). Color bars are centered at $v_{\rm center} = 0$ for the molecular gas velocity fields (except for the BIMA-SONG observation of NGC 5248) or the systemic velocity ($v_{\rm center} = v_{\rm sys}$) for the atomic gas velocity fields. The square in the H I map indicates the FOV of the CO map. The molecular gas has been observed in the transition of the J = 1–0 line of ^{12}CO for almost all galaxies. Only for NGC 7217 the molecular gas observation in the J = 2–1 line of ^{12}CO is shown.

(A color version of this figure is available in the online journal.)

$\sim 0.55 \times 10^{19}$ cm^{-2} column density for the combined BCD array data. To separate real emission from noise, we produced masks by taking only into account those regions which show emission above a set level (3σ) in cubes that have been convolved to 30″ resolution (task CONVL). Using these masks, we blank areas that contain noise in our robust weighted data cubes (task BLANK).

The subsequent analysis has been done with the Groningen Image Processing System (GIPSY; van der Hulst et al. 1992). The channel maps were combined to produce zeroth (intensity map), first (velocity field), and second (dispersion map) moments of the line profiles using the task MOMENT. The RMS values have been measured in two regions where no line signal was apparent and averaged over all channels of the cubes. A flux cut-off of three times the channel-averaged RMS value was used for the moment maps. The velocity-integrated H I intensity maps are presented in Figure 1.

2.3. Molecular Gas Data

The spectroscopic imaging of CO lines provides information about the distribution and kinematics of the molecular gas. The molecular gas has been observed in the transition of the J = 1–0 and J = 2–1 lines of ^{12}CO with maximum angular ($\sim 0\farcs5$) and spectral resolution (3–6 km s^{-1}) using the IRAM Plateau de Bure mm-interferometer (PdBI) as part of the NUGA project and the larger NUGA supersample (García-Burillo et al. 2003). The primary beam size is $\sim 42''$ ($\sim 21''$) in all the CO 1–0 (2–1) line observations. Only for NGC 5248 no PdBI data were available. Therefore, we used for NGC 5248 the publicly available BIMA-SONG data (Helfer et al. 2003) which was observed in the CO (1–0) line with an angular resolution of $6\farcs1$ and spectral resolution of 10 km s^{-1} with the BIMA mm-interferometer. An overview of the observational parameters for the CO data is presented in Table 3.

2.4. Near-Infrared Images

Archival NIR images from *Spitzer, HST*, and ground-based telescopes have been used to estimate the stellar mass distribution in our galaxies. An overview of all NIR images used is presented in Table 4. Foreground stars have been removed using the software tool NFIGI (A. Baillard et al. 2009, in preparation) and, in case additional cleaning was necessary, by hand. In addition, background is subtracted from the NIR images by calculating the mean value in the outer region of the image outside the galaxy disk to ensure that no light contribution from the galaxy itself is subtracted. Other methods for background sub-

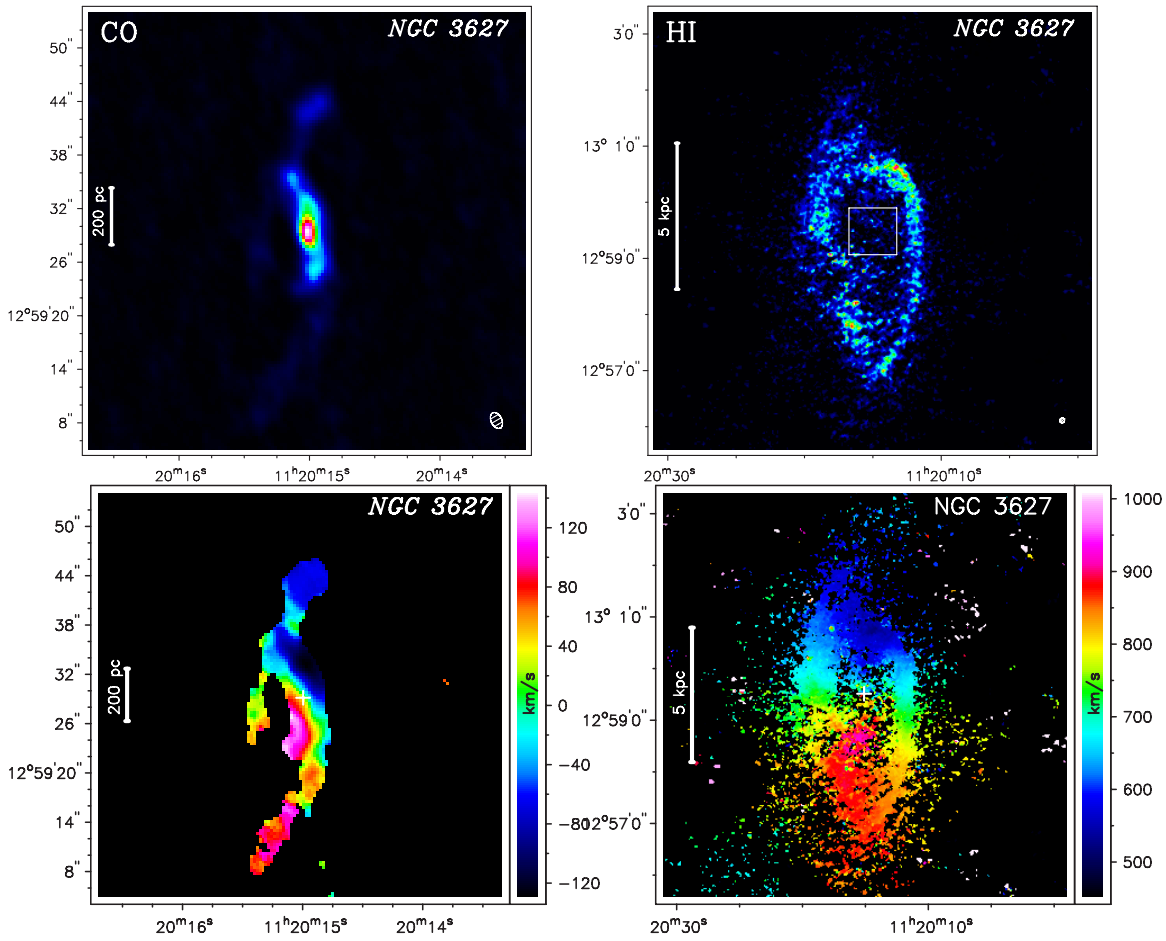

Figure 1. (Continued)

Table 3
Parameters of the CO Data

Name	CO 1-0 Beam (″)	CO 2-1 Beam (″)	Origin
NGC 3368	2.5 × 1.4	1.0 × 0.67	(PI. Schinnerer)
NGC 3627	1.9 × 1.2	0.9 × 0.6	(NUGA)
NGC 4321	2.2 × 1.3	···	(García-Burillo et al. 2005)
NGC 4736	2.1 × 1.7	···	(PI. Schinnerer)
NGC 5248	6.9 × 5.8	···	(Helfer et al. 2003)
NGC 6951	2.6 × 1.7	0.6 × 0.5	(García-Burillo et al. 2005)
NGC 7217	2.4 × 1.9	···	(Combes et al. 2004)

Notes. Overview of the angular resolution of our CO observations using the transition J = 1–0 and J = 2–1 of ^{12}CO. The velocity resolution is ∼5.2 km s^{-1} for all galaxies, except NGC 5248 which has a velocity resolution of ∼10 km s^{-1}. In addition, the origin of the data is listed.

traction have been tested (e.g., fitting the radial luminosity profile to find constant background value), but could not be applied successfully to all NIR images because of limited FOVs. After background subtraction all values below zero, which might be caused by small overestimation of the background value (case only for outer regions of image), were set to zero.

3. KINEMATIC MODELING

To search for kinematic evidence for noncircular motions and radial gas flows, we have performed a detailed kinematic analysis of our CO and H I velocity fields. In Section 3.1, we first estimate the basic disk orientation parameters that are required for our gravitational torque calculations. Then, we model noncircular motions and search for evidence of gas inflow or outflow by employing a Fourier analysis of the velocity fields as described in Section 3.2. The results of this study are presented in Section 3.3 and indicate, e.g., a higher ratio of noncircular to circular gas motions for the central (CO) than for the outer gaseous disk (H I).

3.1. H I and CO Kinematics

In preparation for our analysis of radial gas flows, we derived the following disk parameters by fitting tilted rings to the CO and H I velocity fields using the task ROTCUR within GIPSY.

1. The dynamical center and its offset from the optical center (taken from Hyperleda).
2. The systemic velocity v_{sys} in km s^{-1}.
3. The position angle (PA) in degrees, defined as the angle between the north direction on the sky and the receding half of the major axis of the galaxy in anti-clockwise direction.
4. The inclination (i) in degrees.

The kinematic parameters have been derived in an iterative way (Begeman 1989) as described in our analysis for the entire H I-NUGA sample (Haan et al. 2008). The parameters were assumed to be the same at all radii, except for the circular velocity. We weighted the obtained value in each ring with its standard deviations, in order to derive the mean parameter. For the fit we excluded data points within an angle of 20°

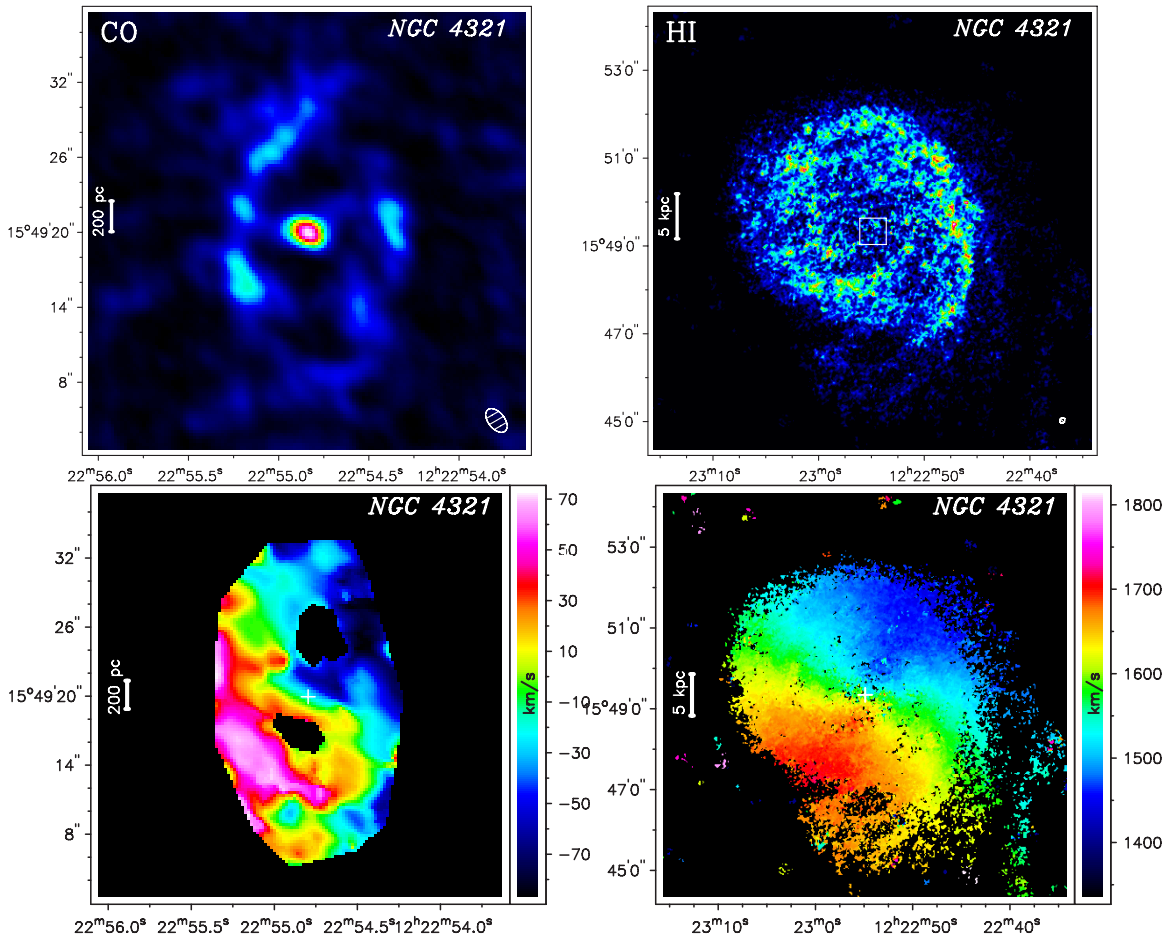

Figure 1. (Continued)

of the minor axis. The widths of the radii were set to 0.″4 (6″) which corresponds roughly to the angular resolution of our CO (H I) data. No radial velocity component was fitted as disk parameter. We have applied the same systemic velocity, inclination, and PA derived from our H I velocity field for the CO analysis as we assume that these disk orientation parameters are constant over the entire galaxy disk. We found no evidence for significantly warped disks in our sample using the derived inclination angle as a function of radius (see Figure 2). For the estimation of the dynamical center position we have taken into account only data of the inner third of the H I gas disk to exclude possible shifts of the kinematic center due to spiral arms and disturbances in the outer H I disk. In addition, we derived the center position from the CO kinematics for most galaxies of our sample. However, our derived values for the kinematic center show only small offsets from the photometric center with an average offset of ∼1.″5 which is similar to typical errors expected from photometric center fitting. An overview of all derived parameters for each galaxy is presented in Table 5. Finally, the rotation velocities were obtained for the atomic and molecular gas with fixed inclination, PA, center, and systemic velocity.

3.2. Description of Kinematic Modeling of Noncircular Motions

In this study, we attempt to detect noncircular motions and subsequently evidence for radial gas flow directly from the observed gas kinematics. In principle, one would expect that noncircular motions are caused by the nonaxisymmetric

Table 4
NIR Data

Name	Instrument	P.I.; Proposal ID	Instrument	P.I.; Program ID
NGC 3368	NICMOS F160w	J. Mulchaey; 7330	IRAC CH1	G. Fazio; 69
NGC 3627	NICMOS F160w	J. Mulchaey; 7330	IRAC CH1	R. Kennicutt; 159
NGC 4321	K-Band	Knapen et al. (2003)	IRAC CH1	R. Kennicutt; 159
NGC 4736	NICMOS F160w	R. Kennicutt; 9360	IRAC CH1	R. Kennicutt; 159
NGC 5248	NICMOS F160w	D. Maoz; 7879	IRAC CH1	G. Fazio; 69
NGC 6951	NICMOS F160w	J. Mulchaey; 7330	K-Band	Mulchaey et al. (1997)
NGC 7217	NICMOS F160w	M. Stiavelli; 7331	H-Band	Eskridge et al. (2002)

Note. Overview of all NIR images used.

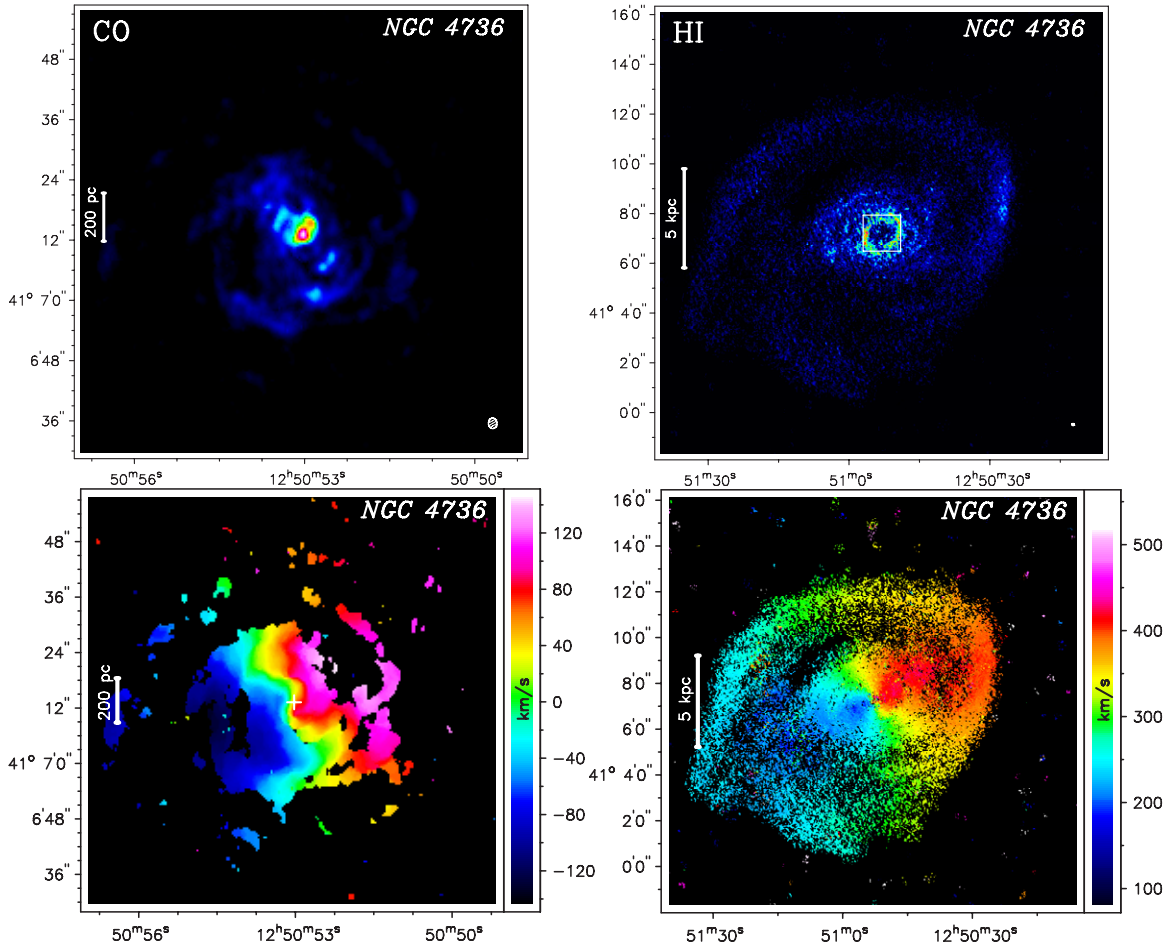

Figure 1. (Continued)

part of the gravitational potential. However in practice, other physical effects such as gas viscosity and shocks in the gas may have significant contributions to any observed noncircular motion. Furthermore, interactions with galaxy companions as well as AGN and star formation feedback might work as additional source for noncircular motions. To estimate the contribution from these effects, we compare the measurement of the noncircular motions with the results obtained via our gravitational torque analysis (see Section 5.3). To obtain a fair estimate of the circular and noncircular part of our gas velocity fields, we have used the GIPSY task RESWRI which performs a harmonic expansion of the velocity fields. This expansion is made by first fitting a tilted-ring model to the velocity field of the gas disk and subsequently decomposing the velocity field along each ring into its harmonic terms. Since the data points may not be uniformly distributed in azimuth, RESWRI performs a least-square fitting (singular value decomposition) rather than a direct Fourier expansion. In practice, after the convergence of the ROTCUR part, RESWRI makes a harmonic expansion of the line-of-sight velocity $v_{\rm los}$ along each ring,

$$v_{\rm los}(r) = v_{\rm sys}(r) + \sum_{n=1}^{k} [c_n(r)\cos(n\psi) + s_n(r)\sin(n\psi)]\,, \quad (1)$$

where k is the order of the fit, r is the radial distance from the center, ψ is the azimuthal angle, measured from the receding side of the line of nodes, and $v_{\rm sys}$ is the systemic velocity as zeroth harmonic component. The coefficients c_n and s_n are determined by making a least-squares fit to the data points up to third order, which requires three sine terms (s_1, s_2, s_3) and three cosine terms (c_1, c_2, c_3). Since the line-of-sight velocity is given in the most general case of a velocity field as

$$v_{\rm los}(r) = v_{\rm sys}(r) + v_\theta(r)\cos(\psi)\sin(i) + v_R(r)\sin(\psi)\sin(i), \quad (2)$$

where v_θ and v_R are the circular and radial components of the velocity field, respectively. Hencefore, $c_1 = v_\theta(r)\sin(i)$ reflects the observed circular velocity, whereas all other terms are contributions to noncircular motions (see for a detailed discussion of the harmonic terms Schoenmakers et al. 1997; Schoenmakers 1999). To estimate the total amount of noncircular motions we calculate the quadratically added amplitude of all noncircular harmonic components v_{nc} up to the order of $N = 3$ (see also Trachternach et al. 2009),

$$v_{nc}(r) = \sqrt{s_1^2(r) + c_2^2(r) + s_2^2(r) + c_3^2(r) + s_3^2(r)}, \quad (3)$$

which is basically the vector sum of all noncircular velocity contributions. The fraction $v_{nc}/v_{\rm rot}$ shows how the contribution of noncircular motions to the total velocity may vary with radius. At the corotation radii (R_{CR}) of a bar or spiral the s_3-terms become dominant over the s_1-terms (Canzian & Allen 1997).

3.3. Results of Our Kinematic Analysis

For the outer disk (probed by our H I gas kinematics), most of the galaxies in our sample exhibit fairly regular velocity

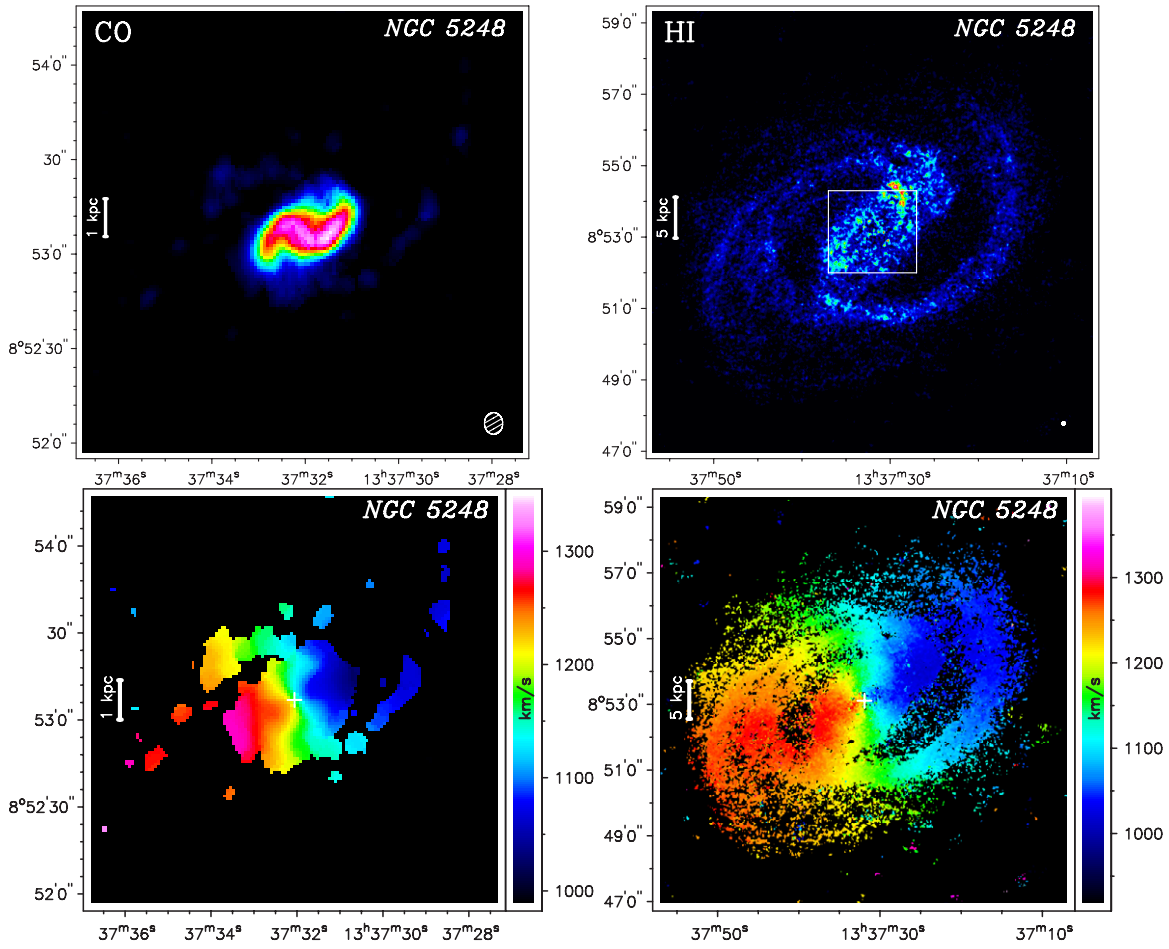

Figure 1. (Continued)

fields that are dominated by circular motions (see Figure 1). The ratio of noncircular motions to rotational velocity $v_{nc}/v_{\rm rot}$ averaged over the radius for H I is typically in the range of 0.05–0.09, except for NGC 3627 and NGC 4736 which exhibit a slightly larger ratio of 0.12 and 0.14, respectively. For NGC 3627, that can be explained by the fact that it belongs to the Leo Triplet and noncircular motions are very likely induced by the past encounter with NGC 3628 (Zhang et al. 1993). Although NGC 4736 exhibits a one-arm spiral in the outer H I disk which might be a hint for a previous interaction, no optical companion is obvious. The mean values of $v_{nc}/v_{\rm rot}$ are derived by weighting the data points with their standard deviations and are presented together with the standard deviation of the mean value in Table 6. Although the mean ratios $v_{nc}/v_{\rm rot}$ are quite small, the ratio of noncircular motions in H I is increasing to 40% as a function of radius, primarily in the inner- and outermost region of the H I disk. For the center at $\lesssim$1 kpc, a larger fraction of noncircular motions is derived from our CO velocity fields with typical values of (7–14)% for NGC 7217, NGC 5248, NGC 3368, NGC 6951 and very large fractions of (22, 33, 83)% for NGC 4736, NGC 4321, and NGC 3627, respectively. In particular, for NGC 3627 noncircular motions seem to dominate the velocity field not only in the center, but also have significant contributions in the outer disk.

In Figure 3, we plot the rotation curve $v_{\rm rot}$ and the fraction of noncircular motion to circular motion v_{nc}/v_{c_1} as a function of radius for each galaxy. The total power of noncircular motions v_{nc} is typically larger for the central (CO kinematics) than for the outer gaseous disk (H I) with mean values of 26% and 9%, respectively. A comparison of noncircular motions and radial flow directions obtained from our kinematics and the ones on the basis of gravitational torques is performed in Section 5.3. Further, we compare in Section 5.3 candidate radial gas flow regions derived from our velocity fields with the inflow/outflow rates due to gravity torques. In fact, all studies that have tried to determine an actual inflow/outflow on the basis of the harmonic decomposition method alone were not very successful so far. The main reason for that is that elliptical streaming in a bar or spiral potential seems to be the dominant contributor to noncircular motions (see Wong et al. 2004, for more details). To derive net inflow/outflow a phase shift between the gas and the gravitational potential has to be present, which is the underlying concept for our gravity torque study in the following section.

4. GRAVITATIONAL TORQUES

In this section, we focus on the study of gravitational torques exerted by the stellar potential on the gaseous disk. By definition, a torque is a vector $\boldsymbol{\tau}$, which points along the rotation axis it would tend to cause. It can be described mathematically as the cross product $\boldsymbol{\tau} = \boldsymbol{r} \times \boldsymbol{F}$ where r is the particle's position vector relative to the fulcrum and F is the force acting on the particles, or, more generally, as the rate of change of angular momentum, $\boldsymbol{\tau} = d\boldsymbol{L}/dt$ where $\boldsymbol{L}$ is the angular momentum vector and t stands for time. The efficiency with which gravitational torques drain the angular momentum of the gas depends first on the strengths of nonaxisymmetric components such as bars and oval distributions, but also, on the existence of significant phase

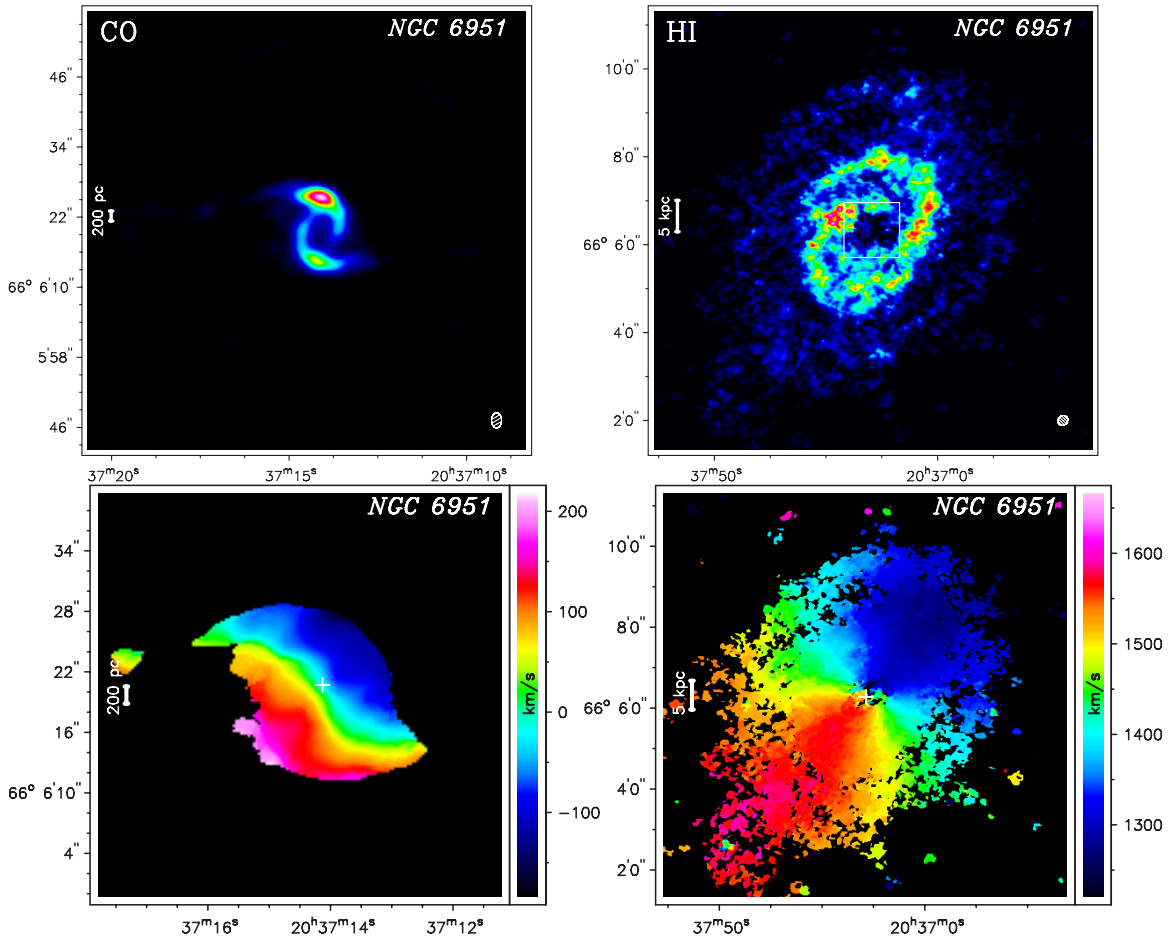

Figure 1. (Continued)

shifts between the gaseous and stellar distributions (García-Burillo et al. 2005). To calculate these phase shifts high spatial resolution images of the gas and stars are necessary. The method of mapping the gravitational potential and torques in a nonaxisymmetric galaxy is based on its appearance in NIR images using a Fourier transform method (Garcia-Burillo et al. 1993; Quillen et al. 1994; García-Burillo et al. 2005). These gravity torque maps are then utilized to determine the transport of angular momentum, gas inflow rates, and the efficiency of the feeding mechanism for the central black hole. For the computation of the potential and torques we have developed a software toolkit (PyPot) which makes use of the programming language Python and its associated software packages (e.g., Scipy).

The major fraction of the stellar mass of spiral galaxies is made up by old stars such as cool giants and dwarfs rather than from hot young stars which are bright and blue. As NIR images detect light primarily from these old stars due to their spectral energy distribution (SED), they better trace the mass distribution of a galaxy in comparison to optical images which are biased by the contribution of bright young stars (Aaronson 1977; Quillen et al. 1994). Furthermore, NIR images are less affected from dust extinction than optical ones and can reveal bars that are not easily observed in the optical (e.g., Quillen et al. 1994).

4.1. Method Description

A detailed description of estimating gravitational torques in spiral galaxies is given by García-Burillo et al. (2005). We used a similar method to derive gravitational torques which is briefly described below and consists of the following steps:

1. Evaluation of the stellar potential using high-resolution NIR images from the Spitzer telescope, ground-based telescopes, and *HST*. To obtain the total gravitational potential we scale the stellar potential with mass-to-light ratios which are estimated by fitting the gaseous rotation curves derived from our H I and CO observations (see Section 3.1). This implicitly assumes that the stellar disks are nearly "maximal."
2. Computation of gravitational forces and gravity torques based on the stellar potential.
3. Weighting of the torque field with the gas column density in order to link the derived torque field to angular momentum variations.
4. Estimation of the gas flows induced by these angular momentum variations using azimuthal averages of the torques at each radius.
5. Finally, the time-scales and gas masses associated with inflow/outflow are derived by estimating the average fraction of angular momentum transferred in one rotation.

As the average fraction of gas to dynamical mass for our sample is ∼5%, the total mass budget is expected to be dominated by the stellar contribution, so that we will neglect self-gravity of the gas.

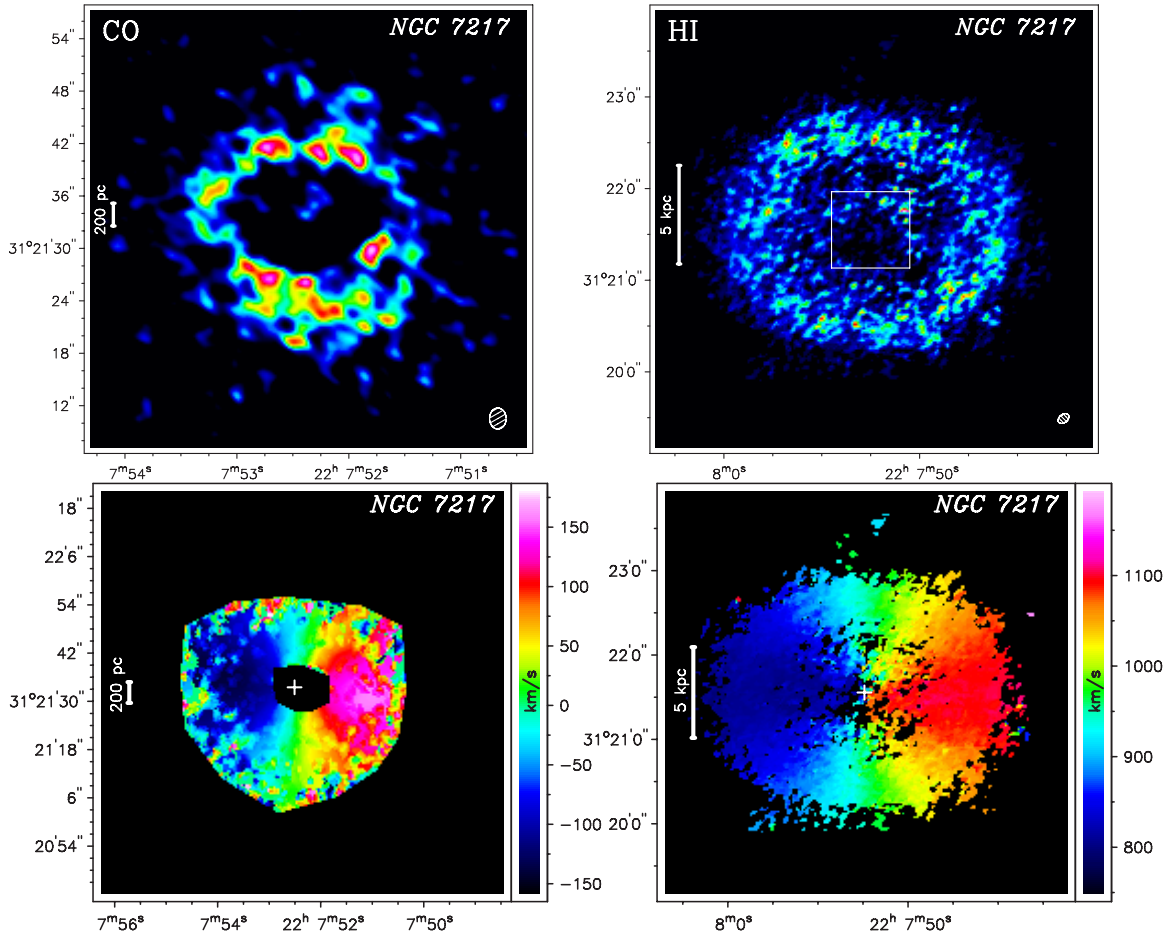

Figure 1. (Continued)

4.1.1. Computation of the Gravitational Potential

The gravitational potential is computed on a Cartesian grid based on the NIR images used as tracers for the stellar potential (following the method of Garcia-Burillo et al. 1993). First, we deproject the NIR and gas images using the inclination i and PA derived from our kinematic analysis (see Section 2.4). An estimation of systematic errors of our calculations due to possible parameter errors will be presented in Section 4.2. Since a bulge would be artificially elongated by the deprojection, the bulge component has to be excluded from the deprojection. Thus, a bulge model is created first using results from fitting a de Vaucouleurs and exponential function to the radial stellar profile representing the bulge and disk brightness profile, respectively. The bulge model is assumed to be spherical. Then the bulge component is subtracted from the NIR image. After the deprojection of the galaxy (without bulge), the bulge model (with the same scaling as before) is added again to the deprojected galaxy disk. The deprojected NIR and gas images are shown in Figure 4.

The gravitational potential of the galaxy,

$$\Phi(\mathbf{x}) = -G \int \frac{\rho(\mathbf{x}')d^3\mathbf{x}'}{|\mathbf{x} - \mathbf{x}'|}, \tag{4}$$

can be written as a convolution of the three-dimensional mass density $\rho(x, y, z)$ and the function $g(r) = 1/r$ (the gravitational potential of a pointlike source),

$$\Phi(x, y, z) = -G \cdot \rho(x, y, z) \otimes g(r), \tag{5}$$

where G is the gravitational constant. We use a smoothing length ϵ, to avoid singularities for distances close to or equal to 0. This results in a slight change of the convolution kernel to

$$g(r, \epsilon) = \frac{1}{\sqrt{r^2 + \epsilon^2}}, \tag{6}$$

and we find the normal $1/r$ function when ϵ goes to 0. Further, the thickness of the stellar component of galactic disks is not negligible. Observations have shown that the vertical scale height of stellar disks is roughly constant as a function of radius (van der Kruit & Searle 1982a, 1982b; Wainscoat et al. 1989; Barnaby & Thronson 1992). To take this into account we assume a noninfinitesimally thin disk and use a model for the vertical distribution $h(z)$, namely an isothermal plane with

$$h(z) = {}^1\!/_2\, h\, h^2(z/a), \tag{7}$$

and a constant scale height a, equal to $\sim 1/12$ of the radial scale length of the galaxy disk. In that case, the mass density distribution is written as

$$\rho(x, y, z) = \Sigma(x, y) \times h(z) \tag{8}$$

$$\text{with} \int_{-\infty}^{\infty} h(z) = 1\,. \tag{9}$$

To compute the potential in the equatorial plane, we integrate the contributions from all heights. This results in a convolution

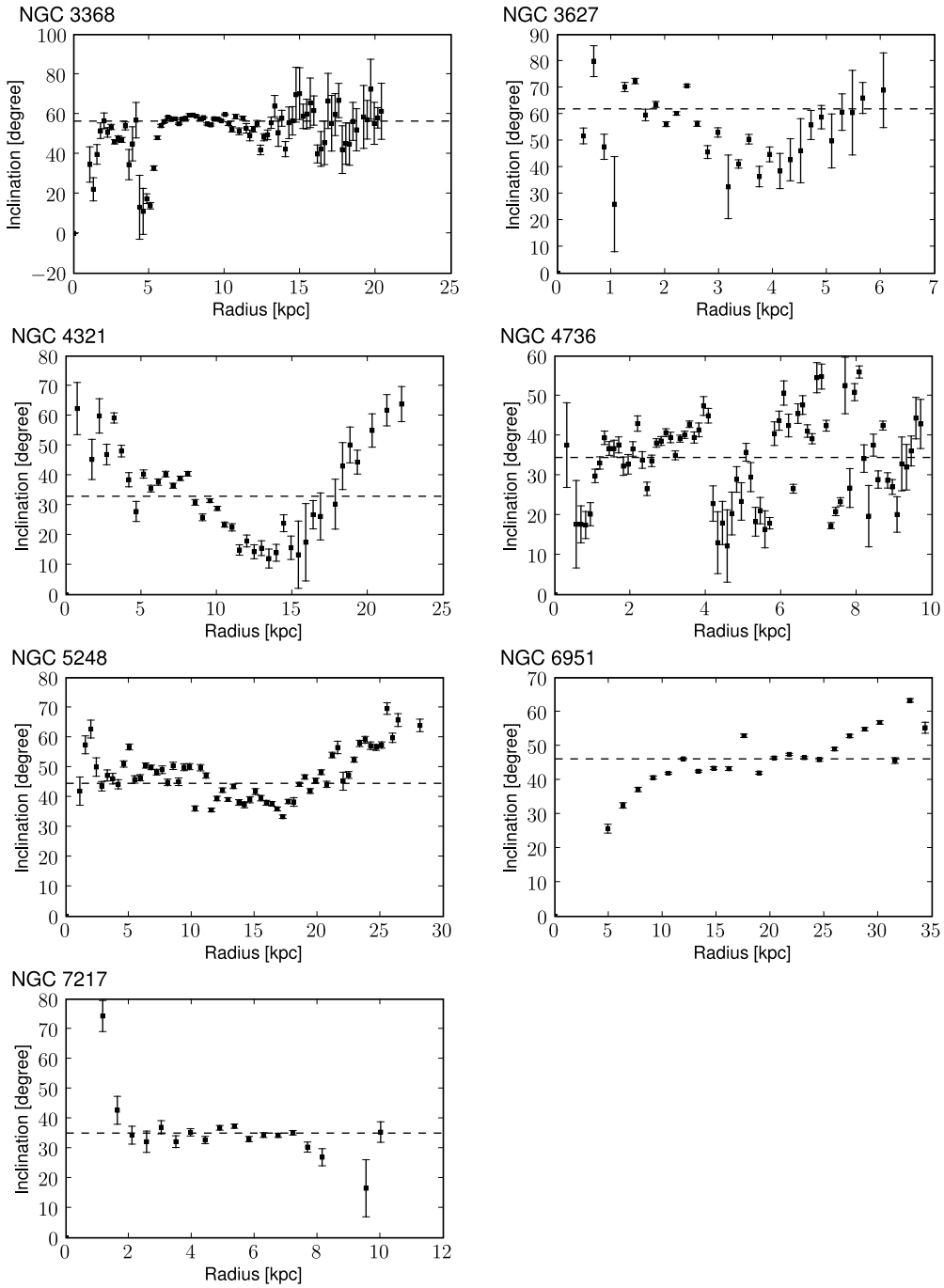

Figure 2. Overview of the inclination angle parameters as a function of radius derived from fitting the H I velocity field. The dashed line indicates the calculated mean inclination angle.

kernel function which can be written as

$$g(r,\epsilon) = \int_{-\infty}^{\infty} \frac{h(z)}{\sqrt{r^2+\epsilon^2+z^2}}\, dz\,. \tag{10}$$

Hence, we still can write the potential in a simple form, at least in the plane of the disk,

$$\Phi(x,\, y,\, z=0) = -G \cdot \Sigma(x,\, y) \otimes g(r,\epsilon)\,. \tag{11}$$

In practice, given the vertical thickening function $h(z)$ and the smoothing length ϵ, we tabulate the function $g(r,\epsilon)$ numerically at the beginning of our code. The convolution is then performed using fast Fourier transforms. Note that in order to avoid edge effects, we extend the grid to a factor of $\sim$4 times larger than the initial grid.

After that, the potential has to be factorized with the appropriate mass-to-light ratio which is calculated via comparing the observed rotation curve and the rotation velocities derived from the potential,

$$f_{\rm scal}(R) \equiv \frac{v_{\rm model}(R)}{v_{\rm rot}(R)}, \tag{12}$$

where $v_{\rm model}$ represents the circular velocity derived from the stellar potential and $v_{\rm rot}$ the rotation curve velocity of our combined and interpolated CO and H I rotation curve at the radius R. Then, we employed a fit on $f_{\rm scal}(R)$ as function of

Table 5
Disk and Kinematic Parameters

Source	x-offset ($''$)	y-offset ($''$)	v_{sys} (km s^{-1})	PA (°)	i (°)
NGC 3368	2.2 ± 0.7	−2.1 ± 0.9	895.5 ± 0.3	168.5 ± 0.5	56.5 ± 0.5
NGC 3627	−0.2 ± 1.0	1.1 ± 2.1	720.3 ± 2.2	174.2 ± 0.7	62.0 ± 2.2
NGC 4321	1.5 ± 0.5	0.4 ± 0.5	1577.5 ± 0.4	152.1 ± 0.4	33.0 ± 1.5
NGC 4736	0.4 ± 0.3	0.5 ± 0.4	309.0 ± 0.5	299.0 ± 0.9	34.5 ± 1.2
NGC 5248	1.6 ± 0.6	−1.1 ± 0.6	1151.3 ± 0.3	113.2 ± 0.5	44.6 ± 0.9
NGC 6951	1.5 ± 1.0	−1.7 ± 1.0	1424.6 ± 0.8	138.1 ± 0.9	46.2 ± 1.1
NGC 7217	−0.3 ± 0.5	0.3 ± 0.4	951.8 ± 0.2	265.3 ± 2.0	35.1 ± 0.6

Notes. Overview of the disk and kinematic parameters derived from the observed velocity field by fitting tilted rings to the velocity field: the offset of the dynamical center of the H I disk to the photometric centers from NED, the systemic velocity v_{sys}, the PA, and the inclination i are listed for all galaxies. Note that the errors are statistical errors and are interdependent for each galaxy.

Table 6
Kinematic Analysis

Source	$\langle v_{nc}/v_{rot}\rangle$	
	CO	H I
NGC 3368	0.132 ± 0.211	0.071 ± 0.120
NGC 3627	0.832 ± 2.571	0.120 ± 0.084
NGC 4321	0.330 ± 0.867	0.068 ± 0.064
NGC 4736	0.221 ± 0.153	0.130 ± 0.300
NGC 5248	0.115 ± 0.042	0.098 ± 0.063
NGC 6951	0.137 ± 0.029	0.066 ± 0.293
NGC 7217	0.071 ± 0.093	0.054 ± 0.056
Mean	0.26	0.09

Note. Overview of the ratio of noncircular motion to rotation velocity v_{nc}/v_{rot} with the standard deviation of the mean value for CO and H I.

radius using a decomposition into disk, bulge, and dark matter component. The derived scaled circular velocities from the gravitational potential match very well the observed circular velocities within ±5% along the radial axis.

4.1.2. Computation of Gravitational Forces and Torques

At first, the forces per unit mass in x- and y-direction $F_{x,y}$ for our derived gravitational potential are calculated at each pixel,

$$F_{x,y}(x, y) = -\nabla_{x,y}\Phi(x, y)\,. \tag{13}$$

The gravity torques (per unit mass) $\boldsymbol{\tau}$ are defined as

$$\boldsymbol{\tau} = \boldsymbol{r} \times \boldsymbol{F}\,, \tag{14}$$

and calculated in the plane

$$\tau(x, y) = xF_y - yF_x. \tag{15}$$

The positive or negative sign of the torque $\tau(x, y)$ defines whether the gas accelerates or decelerates. An example of the gravitational potential and torque is presented in Figure 5 for NGC 6951. The link between torque field and angular momentum variations is made through the observed distribution of gas (García-Burillo et al. 2005) as explained in the following. At first we assume that the CO and H I emission lines are good tracers of the total gas column density in the central and outer disk, respectively. The reason for using two different lines is due to the fact that the neutral ISM undergoes a phase transition from atomic to molecular gas toward the center of a galaxy (Young & Scoville 1991). Since the gas distribution is the convolution of the gas density with the orbit path density, the gas distribution is indirectly equivalent to the time spent by the gas clouds along the orbit paths. Thus, we implicitly average over all possible orbits of gaseous particles. To do this link between the derived torque field and angular momentum variations, the torques are weighted with the gas column density $N(x, y)$ and averaged over the azimuth,

$$\tau(R) = \frac{\int_\theta \left[N(x, y) \cdot (xF_y - yF_x)\right]}{\int_\theta N(x, y)}\,. \tag{16}$$

By definition, $\tau(R)$ represents the azimuthal-averaged time derivative of the specific angular momentum L of the gas, i.e.,

$$\tau(R) = \left.\frac{dL}{dt}\right|_\theta. \tag{17}$$

The positive or negative sign of $\tau(R)$ defines whether the gas may gain or loose angular momentum, respectively. The fueling efficiency can be estimated by deriving the average fraction of the gas specific angular momentum transferred in one rotation (T_{rot}) by the stellar potential, as a function of radius, defined as

$$\frac{\Delta L}{L} = \left.\frac{dL}{dt}\right|_\theta \cdot \left.\frac{1}{L}\right|_\theta \cdot T_{rot} = \frac{\tau(R)}{L_\theta} \cdot T_{rot}\,, \tag{18}$$

where the azimuthal-averaged angular momentum L_θ is assumed to be well represented by its axisymmetric average, i.e., $L_\theta = R \cdot v_{rot}$. The inverse of $\Delta L/L$ determines how long it will take (in terms of orbital time periods) for the gravitational potential to transfer the equivalent of the total gas angular momentum. The mass inflow/outflow rate of gas per unit length $d^2M(R)/(dRdt)$ (in units of $M_\odot$ yr^{-1} pc^{-1}) is calculated as follows:

$$\frac{d^2M(R)}{dRdt} = \left.\frac{dL}{dt}\right|_\theta \cdot \left.\frac{1}{L}\right|_\theta \cdot 2\pi R \cdot N(x, y)|_\theta, \tag{19}$$

where $N(x, y)|_\theta$ is the gas column density of the atomic (H I) and molecular gas using the conversion factor from CO to H_2 typical for galaxy nuclei of $X = N(H_2)/I(CO) = 2.2 \times 10^{20}$ cm^{-2} K^{-1} km^{-1} s (Solomon & Barrett 1991). Then, the integrated inflow/outflow rates $dM(R)/dt$ are derived by integrating from $R = 0$ out to a certain radius R,

$$\frac{dM(R)}{dt} = \sum_0^R \left[\frac{d^2M(R)}{dRdt} \cdot \Delta R\right], \tag{20}$$

with ΔR as radial binning size (in units of pc).

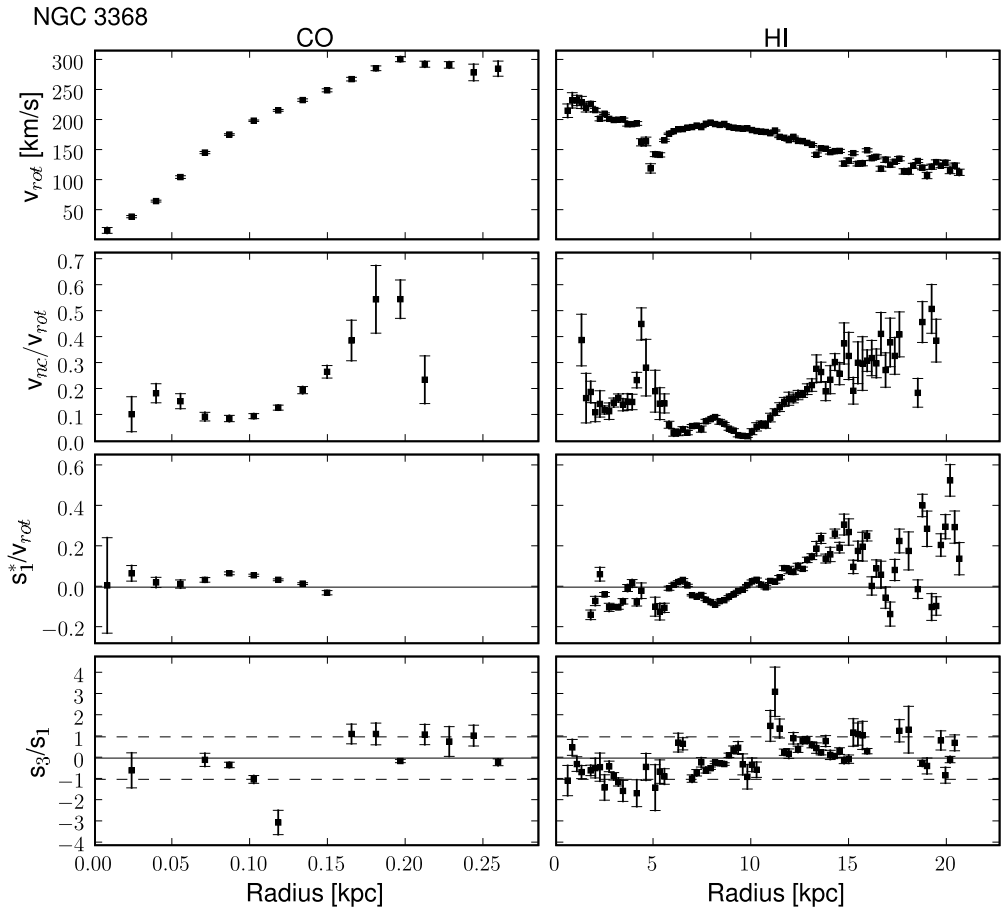

Figure 3. Overview of the modeling results based on the CO (left panels) and H I (right panels) velocity fields. From the top to the bottom panels: the rotation curve $v_{\rm rot}$, the ratio of noncircular motion to rotation velocity $v_{nc}/v_{\rm rot}$, the ratio of the amplitude of the first sine term to the rotation velocity $s_1^*/v_{\rm rot}$, and the ratio of s_3/s_1 as a function of radius for each galaxy. Candidate radial gas outflow and inflow are characterized by a positive and negative sign of the $s_1^*/v_{\rm rot}$ term as long as $|s_3/s_1| \ll 1$. Data with error bars larger than three (two) times the median of the data set are clipped for H I (CO). At the CR radius R_{CR} the dominance switches from the s_1- to the s_3-terms (Canzian & Allen 1997) as indicated by the horizontal dashed lines at $s_3/s_1 = \pm 1$.

4.2. Robustness of the Method: Parameters and Errors

In order to examine the reliability of our results, we estimated how small errors in our assumed fitting parameters will affect the results. One main source for errors arises from uncertainties in the input parameters that were derived from our kinematic study (see the previous section). First, we checked the parameters that describe the geometry of the disk given by inclination i, PA, and position of the center (x, y). We assume that these parameters do not vary with radius. To evaluate the effects of changes in these parameters on the derived gravity torque map, we tested two simple disk models (see Figure 6): (1) an exponential disk which produces no torque pattern because of its axisymmetrical distribution, and (2) an exponential disk plus an additional constant oval distribution mimicking a barred galaxy, which produces a typical torque that changes sign between the four quadrants. The oval distribution has a minor-to-major axis ratio of 0.5 and a constant surface brightness of 20% of the maximum brightness of the exponential disk. For comparison, typical torque patterns without parameter errors are presented in Figure 7 for different disk models. We tested the robustness of the results from our code with uncertainties based on our kinematic analysis (Section 3):

1. An inclination error of 3° at a typical inclination of 45°: the result shows an additional torque pattern that changes sign between the four quadrants. This pattern corresponds to one induced by a small oval contribution. Because of its axisymmetry and uniform gas distribution no contribution in the radial profile is seen. In principle, an inclination error will produce a fake bar; or oval but it will be along one of the principal axes of the disk (major, minor) and hence might provide a way to disentangle this false pattern from a true one.
2. A PA error of 2°: here, the torque also changes sign between the four quadrants, causing a pattern similar to an oval distribution, but along an axis that is rotated by 45° to one of the principal axes.
3. An error of the center position of 1 pixel which corresponds to ∼50 pc at a distance of 10 Mpc and a pixel size of 1″ that results in a bimodal pattern, which increases the torque budget of one side of a torque pattern produced by an oval distribution, and decreases the torque at the opposite side.

Since this simple test does not take into account the gas distribution of a "real" galaxy which very likely differs from an homogeneous axisymmetric distribution, we also estimated the effects of these uncertainties using the NIR images and gas maps of a typical galaxy from our sample, namely NGC 6951. In order to estimate the errors in the radial torques, we compared the torque results using the best input parameters with those where typical errors of the input parameter were applied. The total error as a function of radius is shown in Figure 8. The

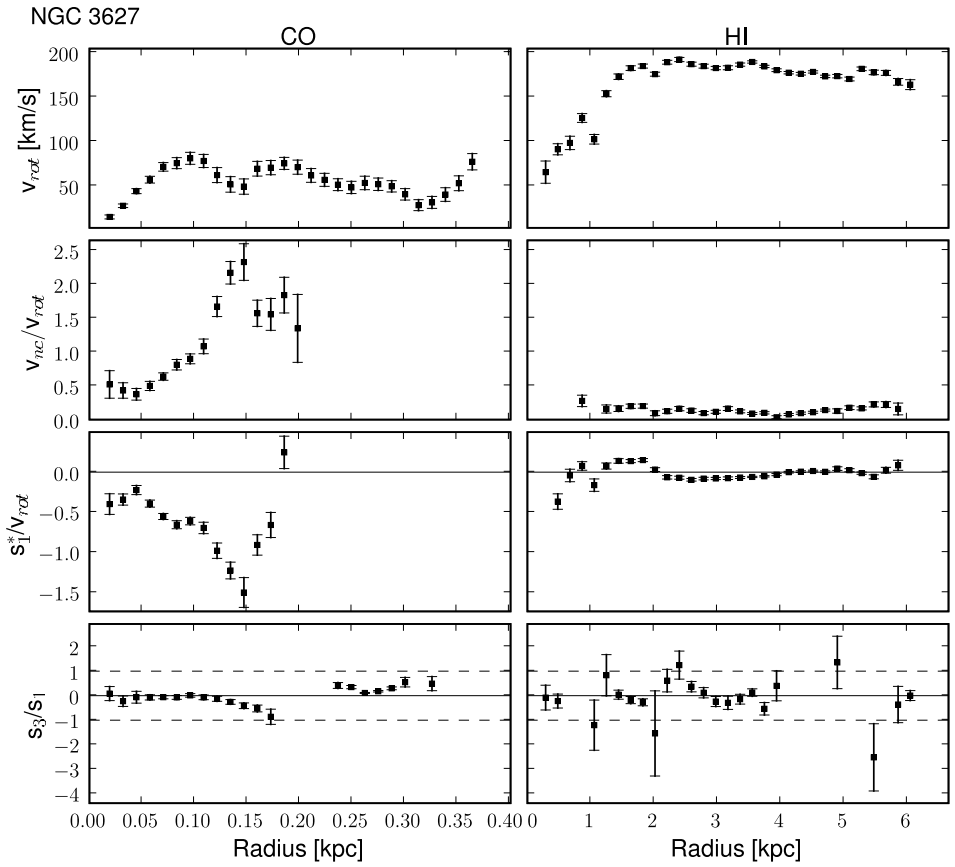

Figure 3. (Continued)

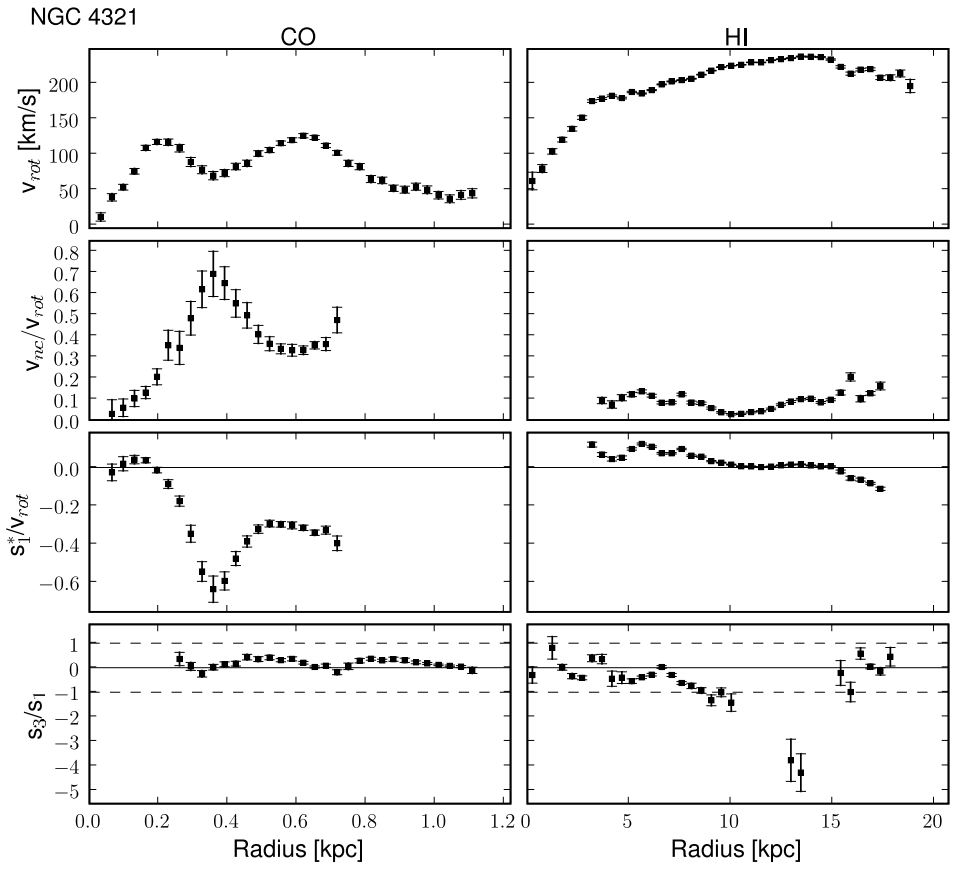

Figure 3. (Continued)

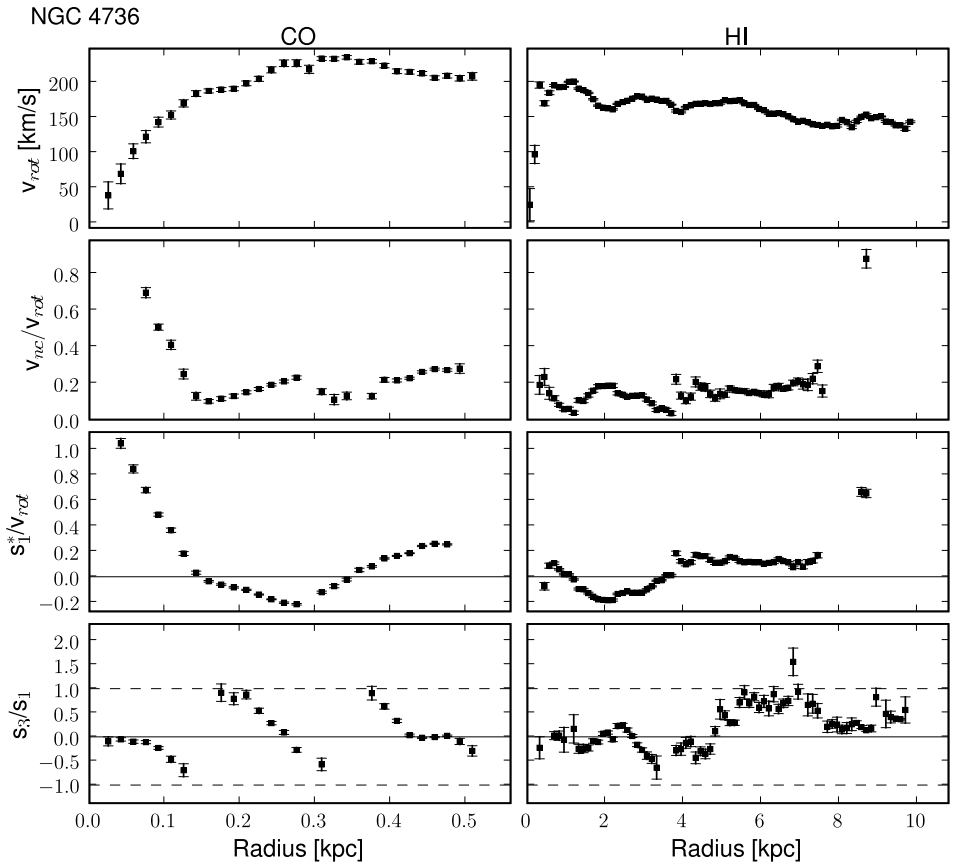

Figure 3. (Continued)

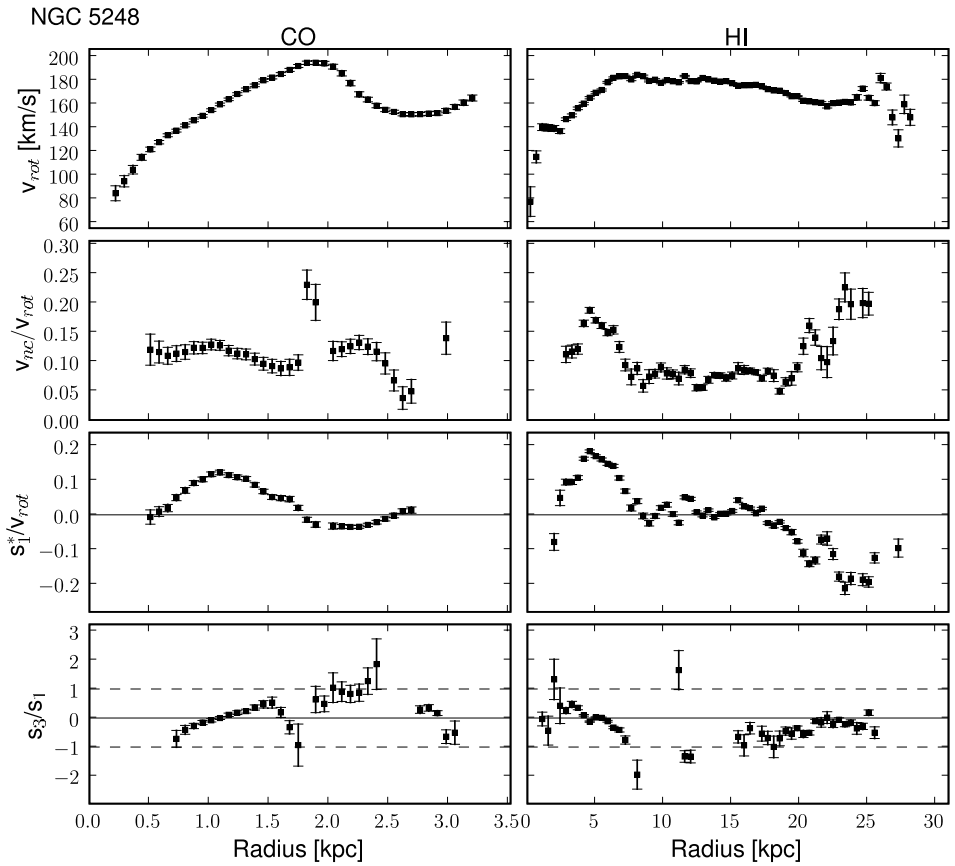

Figure 3. (Continued)

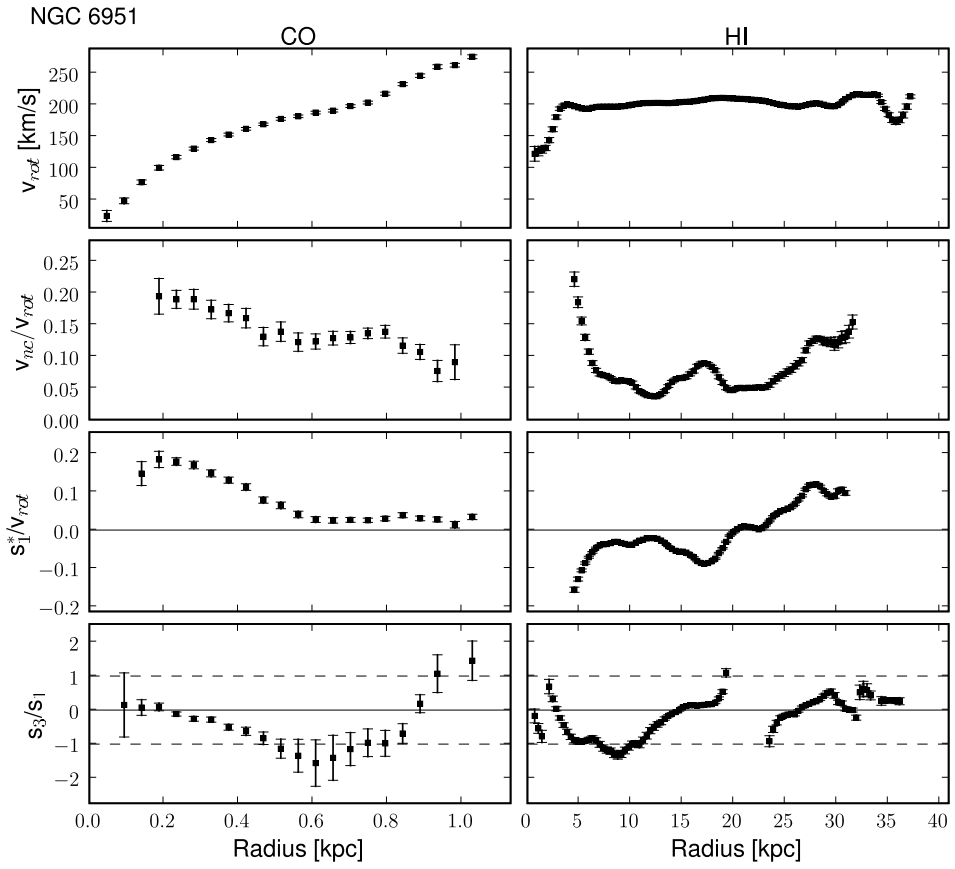

Figure 3. (Continued)

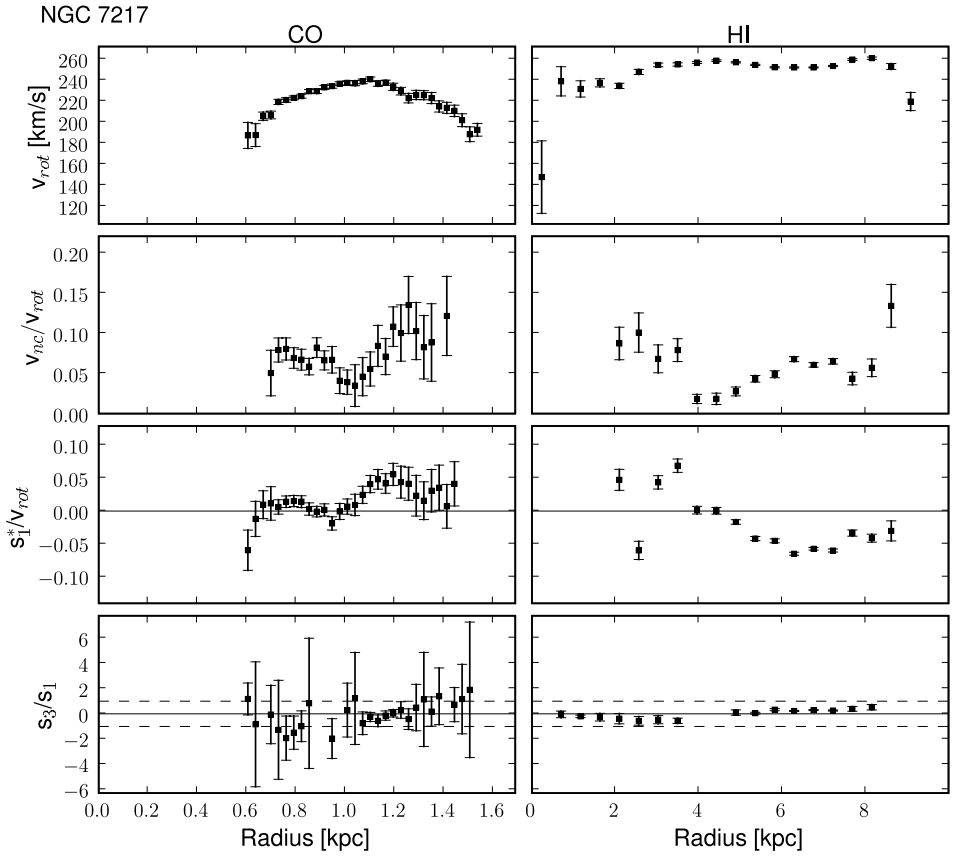

Figure 3. (Continued)

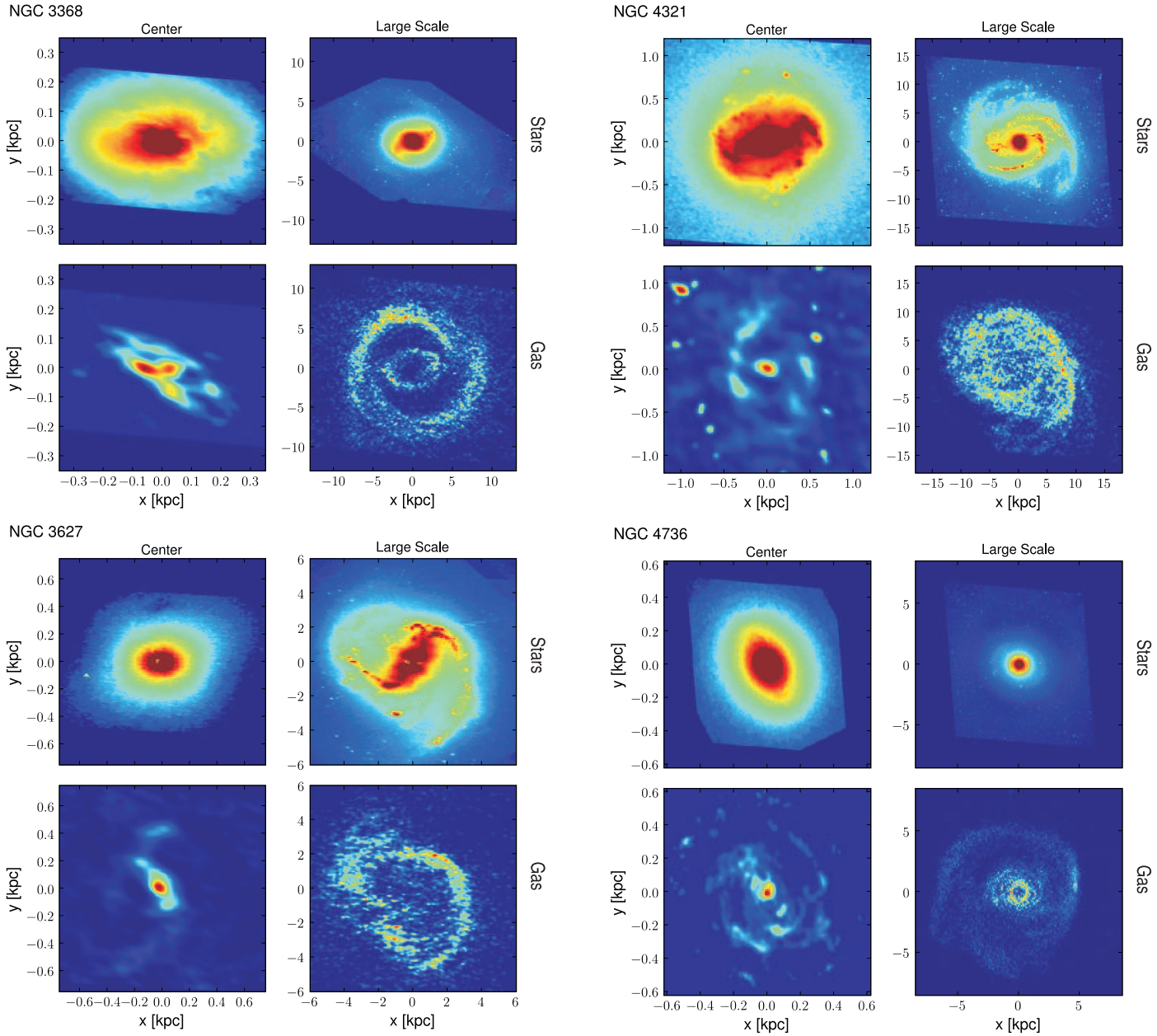

Figure 4. Overview of the deprojected stellar (top panels) and gaseous distribution (bottom panels) traced by our CO (left bottom panels) and H I observations (right bottom panels).

(A color version of this figure is available in the online journal.)

Figure 4. (Continued)

results of this test are summarized in Table 7, separately for the central CO based and outer H I-based torque calculation.

Not only geometric uncertainties can have an effect on our results, but also the assumed mass-to-light ratio. Since we scale our potential with the derived (deprojected) rotation curve from the velocity maps, our results do not depend on uncertainties in the mass-to-light ratio, e.g., derived from stellar population models. Instead, our method relies on a scaling factor between the circular velocity derived from the stellar potential and the combined CO and H I rotation curve as given by Equation (12). Since rotation curves are derived from azimuthal-averaged velocities, different mass-to-light contributions of nonaxisymmetric components such as spiral arms (cool supergiants or dust glowing star formation regions) and bars will affect the scaling. Furthermore, possible deviations from a constant inclination of the galaxy disk (i.e., warping disk) might have an impact. However, most spiral galaxies show only small variations in the inclination across the stellar disk and we found no evidence for a significant warped disk in our sample as described in Section 3.1.

Another possible source of error might be that the gas distribution is not 100% recovered at all spatial scales due to missing short spacings of the interferometer observations. As our H I observations are continuous and traces all spatial scales, H I is a good tracer for the atomic gas distribution in our galaxies. For CO, the PdBI observations do not trace all spatial scales, and thus, might miss some flux from short spacings. However, to estimate the effect of short spacing corrections, S. García-Burillo et al. (2008, in preparation) have compared the gravity torque results for NGC 4579 without (only CO PdBI-data) and with short spacing corrections using additional CO data obtained with the IRAM 30 m telescope. The result shows

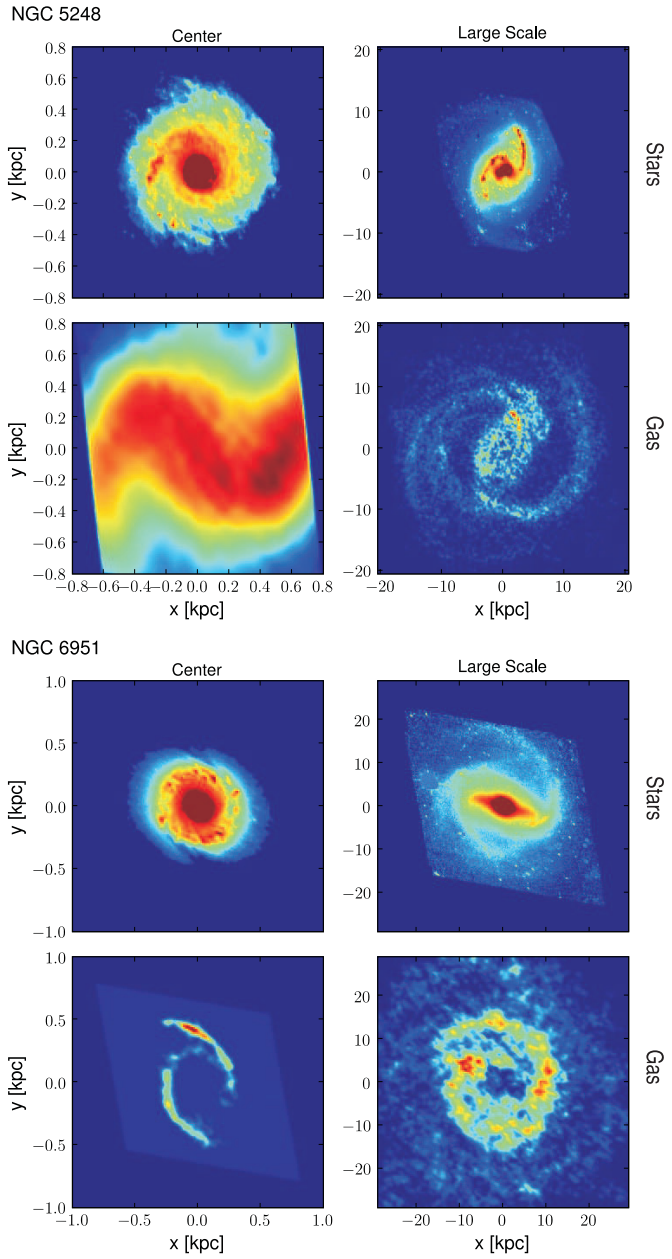

Figure 4. (Continued)

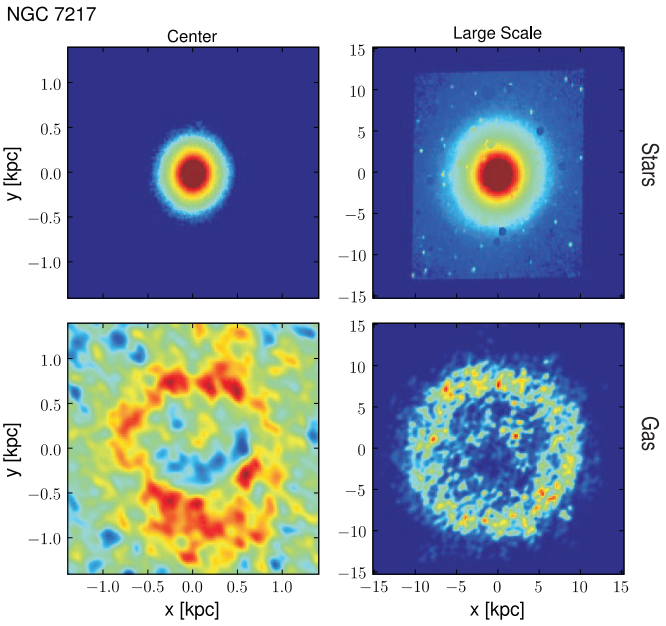

Figure 4. (Continued)

that the gravitational torques with short spacings are roughly (5–40)% larger than without short spacings.

4.3. Determining the Corotation Radii

The accurate determination of the corotation (corotation resonance (CR)) radii of density wave patterns is an important parameter for the characterization of the dynamical state of a galaxy and to understand the relation between morphologies and kinematics of galaxies. We have applied the potential density phase shift method (Zhang & Buta 2007) to derive the CR radii for our galaxies. This technique is based on the calculated radial distribution of an azimuthal phase shift between the stellar potential and a stellar density wave pattern which results in a torque action between the wave pattern and the underlying disk matter. Consequently, the material inside (outside) the CR radius looses (gains) angular momentum which causes an inflow (outflow). The validity of the phase-shift method is based on the global self-consistency requirement of the wave mode (i.e., both the Poisson equation and the equations of motion need to be satisfied at the same time). For a self-sustained global spiral mode, the radial density variation of the modal perturbation density, as well as the pitch angle variation, together determine that the Poisson equation will lead to the zero crossing of the phase-shift curve being exactly at the CR radius of the mode (see for more details Zhang & Buta 2007).

We calculated the CR radius using the method of Zhang & Buta (2007) as follows: the rate of angular momentum exchange between the density wave pattern and the axisymmetric part of the disk can be either expressed as (Zhang 1996)

$$\frac{dL}{dt}(r) = -\frac{1}{2\pi}\int_0^{2\pi} \Upsilon(r,\phi)\frac{\partial\Psi(r,\phi)}{\partial\phi}d\phi, \qquad (21)$$

with the perturbation density waveform Υ and the perturbation potential waveform Ψ, or as two sinusoidal waveform,

$$\frac{dL}{dt}(r) = \frac{m}{2}A_\Upsilon(r)A_\Psi(r)\sin\left[m\phi_0(r)\right], \qquad (22)$$

with the amplitudes of the density wave A_Υ and potential wave A_Ψ, the nonaxisymmetric mode number m (e.g., for two spiral arms or a bar: $m = 2$), and the phaseshift ϕ_0 between these two waveforms. Using these two equations, the phaseshift ϕ_0 can be calculated from

$$\phi_0(r,\phi) = \frac{1}{m}\sin^{-1}\left[\frac{1}{m}\frac{\int_0^{2\pi}\Upsilon(r,\phi)\frac{\partial\Psi(r,\phi)}{\partial\phi}d\phi}{\sqrt{\int_0^{2\pi}\Psi^2 d\phi}\sqrt{\int_0^{2\pi}\Upsilon^2 d\phi}}\right]. \qquad (23)$$

The potential Ψ and the density distribution Υ are taken from our gravity torque calculation (see Section 4.1). We assume that the phaseshift is positive when the potential lags the density wave in the azimuthal direction in the sense of the galactic rotation. For all of our galaxies we derived the phaseshift as a function of

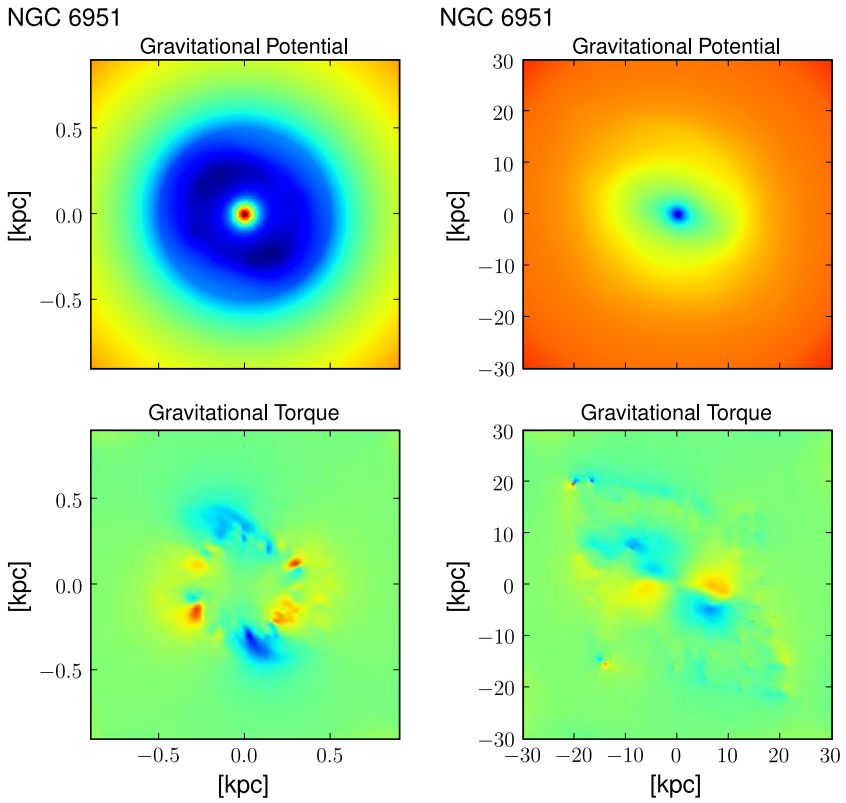

Figure 5. Example of the gravitational potential and torque (without weighting with the gas component) for the center (left panels) and the large scale (right panels) for NGC 6951.

radius and we defined the CR radii as the positive-to-negative crossings of the phaseshift ϕ_0 (see Figure 9). At this location the direction of angular momentum transfer between the disk matter and the density wave changes sign.

In fact, the phase shift method of Zhang & Buta (2007) is mathematically very similar to our gravity torque study as both rely on a phase shift between the gravitational potential and a density wave pattern. Thus, also the gravity torque is expected to change sign at each resonance with the gas as test particles for measuring the gravity torques. On the other hand, the gravity torque method might differ from the potential density phase shift in the case of a superposition of density patterns or a shift of gas due to viscosity. However, in the case of a strong dominating pattern, both methods are expected to reveal a similar location for the CR radius.

To verify our estimation of the CR radii we derived additionally the CR radii using the bar length and the method of Canzian (1993; see Section 3.2). A comparison of the results derived from these different studies is presented in Table 8 for all our galaxies. The CR radius is assumed to be 1.1–1.6 times the radius of the bar (Rautiainen et al. 2008) and is visually estimated directly from the deprojected NIR images (Figure 4) using the change in PA and the ellipticity of the bar. All three methods (Canzian, bar length, phase shift) reveal roughly the same radii for the CR of the bar. For our galaxies the phase-shift method appeared to be the most precise method with uncertainties of (5–10)% and the Canzian method the most unprecise one with uncertainties ranging up to 50%. The estimation of the CR using the bar length suffers from the uncertainty in the estimation of the bar length and its relation to the CR radius, which lies in the range of 10%–30%. The comparison between the CR radii determined by our gravity torques study and the phase-shift method of Zhang & Buta (2007) reveals significant differences for the location of the CR radii of the bar for NGC 3368, NGC4321, and NGC 6951 (see Table 8). One possible explanation for these differences is that all three galaxies exhibit a strong stellar bar as well as a spiral pattern (also visible in the NIR images) which might be superimposed.

To derive the location of the inner Lindblad resonance (ILR), the ultra harmonic resonance (UHR), and outer Lindblad resonance (OLR) we used a simple method presented in Figure 10 which is described in the following. The angular velocity Ω is calculated from a fit using a cubic spline interpolation to our measured CO and H I rotation curve. After determining the bar pattern speed at the location of the CR (taken from the phase-shift method), the frequency curves $\Omega \pm \kappa/2$ and $\Omega - \kappa/4$ are derived with the epicyclic frequency

$$\kappa = \sqrt{4\Omega^2 + R\frac{d\Omega^2}{dR}}\,. \tag{24}$$

The derived CR, ILR, UHR, and OLR are also listed in Table 8. Interestingly, the OLR caused by the bar seems to overlap for some galaxies (NGC 3368, NGC 6951) with the CR radius of the spiral determined by the phase-shift method, suggesting a coupling between bar and spiral resonances. However, as our uncertainties in the estimation of the OLR are quite large, this correlation is not very significant.

4.4. Results

We have derived neutral gas inflow rates for seven nearby spiral galaxies as a function of radius as well as location within the disks (see the top panel of Figure 11). By definition, the torque $\tau(R)$ represents the azimuthally-averaged time derivative of the specific angular momentum of the gas. The positive or

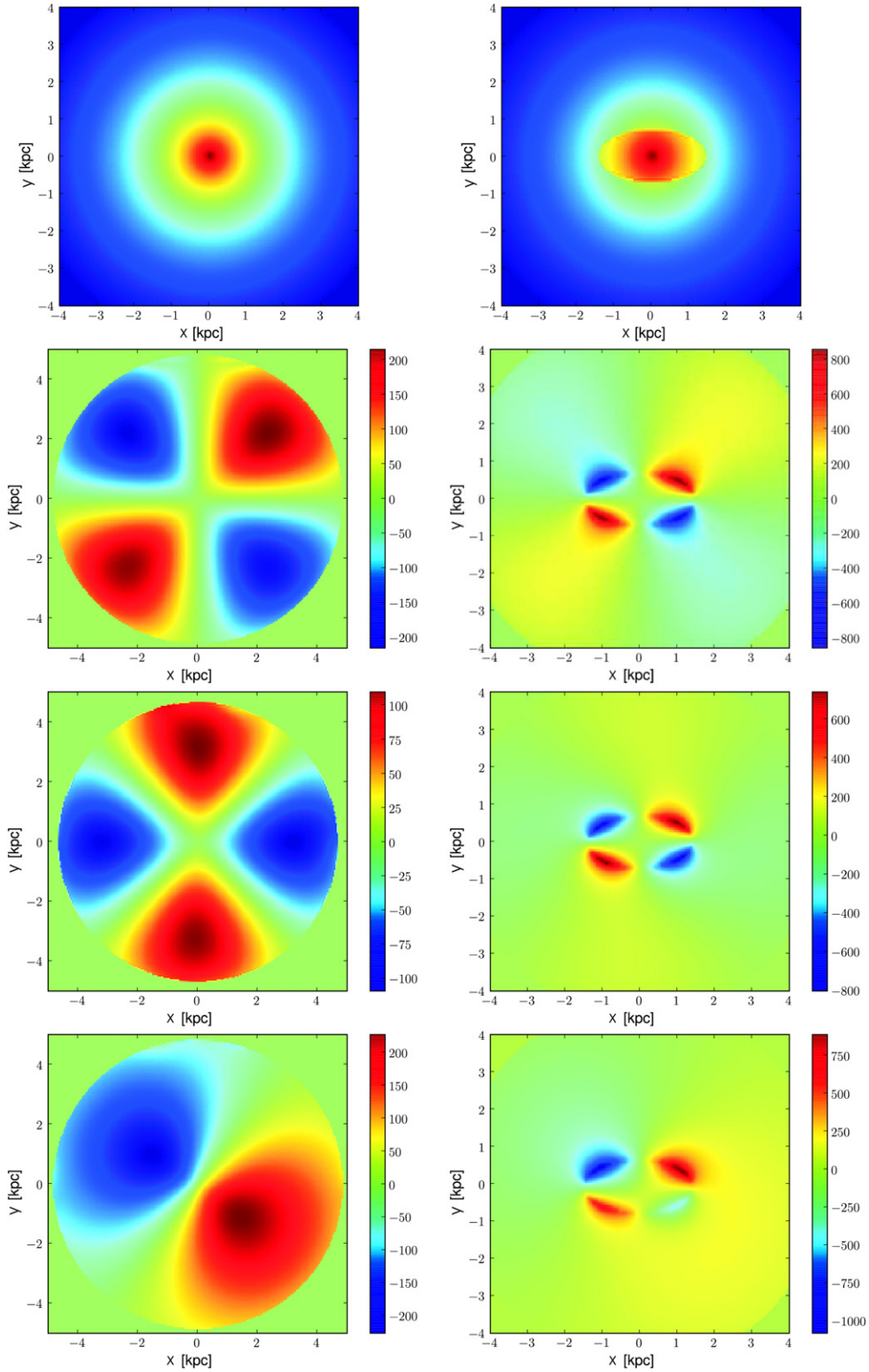

Figure 6. Overview of the error estimation from models. The computed torques are calculated for two models: (1) an exponential disk (top left panel) which produces no torque pattern because of its axisymmetric distribution, and (2) an exponential disk plus an additional constant oval distribution (top right panel). The torque calculation is tested with uncertainties of an inclination error of 3° (second row), a PA error of 2° (third row), and an error of the center position of 1 pixel $\simeq 1''$ (bottom row).

negative sign of $\tau(R)$ defines whether the gas may gain or loose angular momentum, respectively. For almost all galaxies of our sample the torque changes sign in different quadrants which corresponds to inflow and outflow in adjacent quadrants. As such a pattern is generally expected to be generated by $m = 2$ modes, (e.g., bar or oval potential), we conclude that this mode is the dominant mode in our sample. Only NGC 5248 shows a bipolar torque pattern for the center. In addition, the torque

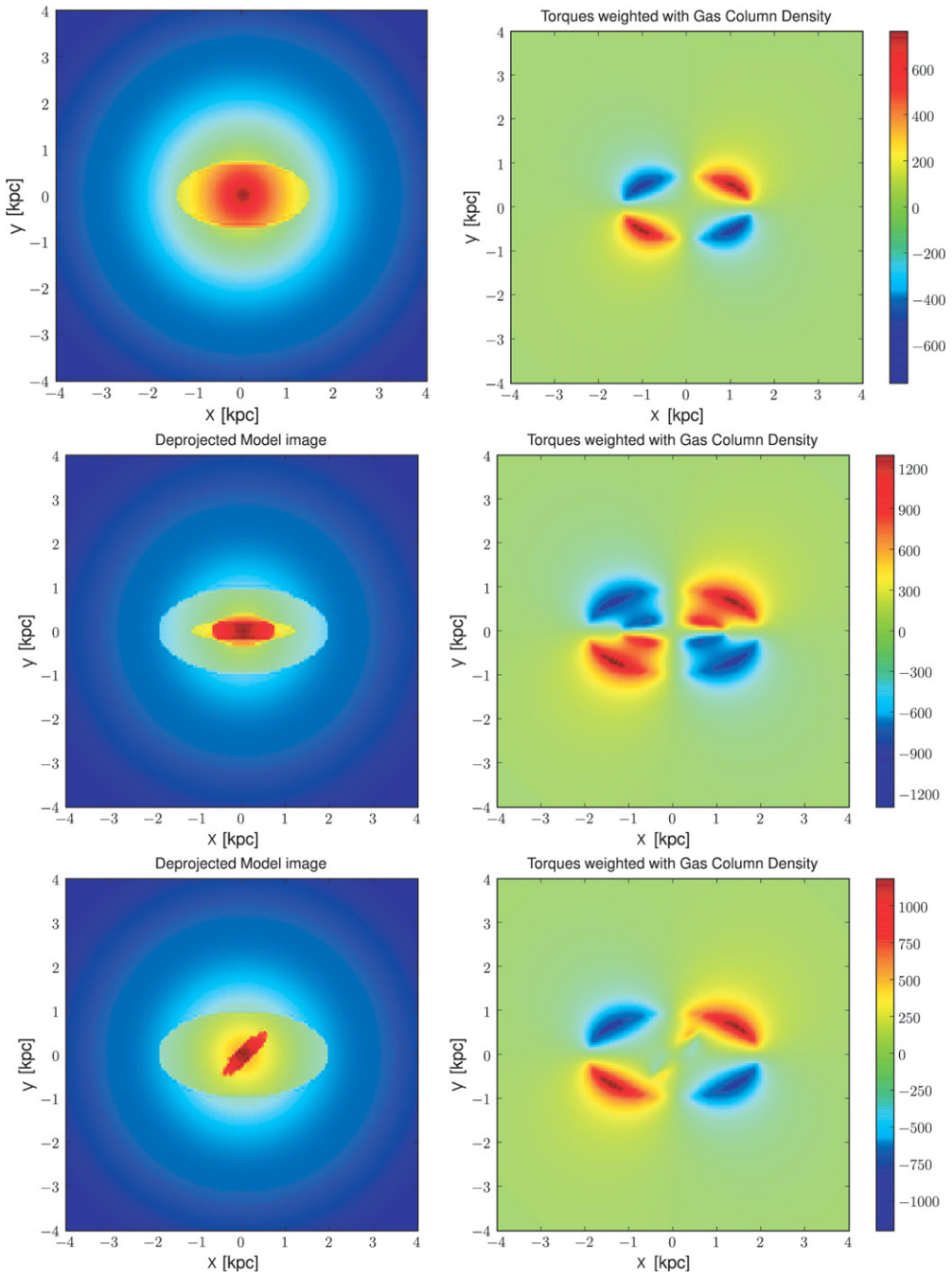

Figure 7. Comparison of the torque patterns (right panels) derived from three different models (left panels): (1) exponential disk plus a constant oval distribution (top row), (2) exponential disk plus three parallel aligned constant oval distributions/bars with different lengths and strengths (middle row), and (3) exponential disk plus a constant oval distribution and an inner bar with a difference in PA of 45° (bottom row).

pattern is very sensitive to the presence of stellar spiral arms which cause a positive (negative) torque on the side of the spiral arm toward (away from) the galaxy center. Such a torque pattern is present in all galaxies of our sample, except for NGC 7217 and NGC 4736.

To estimate radial gas flows and time scales we derived the azimuthally averaged torque $\tau(R)$ and the angular momentum transferred in one rotation $dL(R)/L$ as a function of radius which are presented in Figure 11. Similarly to the torque maps, a positive or negative sign of $\tau(R)$ and $dL(R)/L$ defines whether the gas may gain or loose angular momentum corresponding to gas outflow or inflow, respectively. The transferred angular momentum and gas masses averaged over the entire galaxy disk are listed in Table 9 for each galaxy. We found that the average-transferred angular momentum $\langle dL/L\rangle$ over the entire gas disk lies in the range of -0.04 (NGC 6951) to 0.06 (NGC 5248) for H I and -0.5 (NGC 3368) to 0.16 (NGC 3627) for CO. To estimate the mean amplitude of angular momentum exchange within the disk we derive the mean value of the absolute angular momentum transfer, $\langle|dL/L|\rangle$. This parameter is used later in Section 5 for a comparison to the noncircular motions identified in our analysis of the gas kinematics. We found values of $\langle|dL/L|\rangle$ in the range of 0.03 (NGC 7217) to 0.26 (NGC 3627) for H I and 0.03 (NGC 7217) to 0.55

Table 7
Error Estimation

Parameter	$d\tau$ (CO)	$d\tau$ (H I)
Position Angle (dPA = 2°)	4%	<1%
Inclination ($di = 2°$)	24%	<1%
Shift of IR Image (0.″2)	10–30%	∼13%
Shift of Gas Image (0.″3)	5–20%	5–20%
Background Subtraction	<5%	<1%
Bulge-Nobulge Subtraction	< 2%	3–10%
Rot. Vel. ($dv = 15$ km s^{-1})	20%	10%
Sum	60–80%	13–70%
Typical	67%	30%

Notes. Estimation of systematic errors in the radial torques for CO and H I of a typical galaxy from our sample, namely NGC 6951. For this exercise, the torque results using the best input parameters have been compared with those where typical errors of the input parameters were applied. Note that the errors have a radial dependency (see Figure 8)

(NGC 3368) for CO. Clearly, NGC 7217 exhibits the lowest torque strength and angular momentum transfer in our sample due to its nearly axisymmetric potential (Combes et al. 2004) whereas NGC 3627 and NGC 3368 exhibit the largest amplitude of angular momentum exchange. In general, the amplitude of $\langle|dL/L|\rangle$ is larger in the center (CO) than in the outer disk (H I).

To estimate the transferred gas mass at a certain radius, we derived the mass inflow/outflow rates $d^2M(R)/(dRdt)$ (in units of $M_\odot$ yr^{-1} pc^{-1}) as a function of radius (see Figure 12). In addition, we examined the net mass flow $dM(R)/(dt)$ (in units of $M_\odot$ yr^{-1}) outward to a given radius R by integrating over the gravitational torques of the molecular and atomic gas disk, separately. These values represent the net gas mass inflow/outflow within these regions and can be compared to the typical gas masses required by star formation and AGN fueling (see Section 5). A positive (negative) sign indicates gas outflow (inflow). The net gas mass flow for the entire molecular and atomic gas disks (integrated from 0 to $R_{\rm max}$) are listed in Table 9 with a range of −0.01 to 0.5 $M_\odot$ yr^{-1} for the atomic gas ($R_{\rm max} \simeq 20$ kpc) and much larger values of −23 to 50 $M_\odot$ yr^{-1} for the molecular gas in the center ($R_{\rm max} \simeq 1$ kpc). However, to study the redistribution of gas within the galaxy disk, e.g., caused by bar and spiral wave patterns, one has to examine the gas mass flow as a function of radius (see Figure 12). For example, the net gas mass flow over the entire disk can be zero while a large redistribution of gas may occur within the disk. This seems to be the case for, e.g., NGC 3627 where we found a large net gas mass inflow in a region of $0 < R < 3$ kpc ($\sum_0^{3\,\rm kpc} M_\odot$ yr$^{-1} = -1\ M_\odot$ yr^{-1}), and a similar value with the opposite sign (gas mass outflow) from 3 kpc to the outer region of the galaxy ($\sum_{3\,\rm kpc}^{6\,\rm kpc} M_\odot$ yr$^{-1} = 1 M_\odot$ yr^{-1}), so that the sum over the entire disk results coincidentally in an almost zero net gas mass flow ($\sum_0^{R_{\rm max}} M_\odot$ yr$^{-1} = -0.1 M_\odot$ yr^{-1}). In general, we found for our sample that the amplitude of the gas mass flow within the disk is much larger than the net gas mass flow over the entire gas disk. This indicates that the redistribution of gas within the galaxy exceeds the net gas mass outflow/inflow from the entire galaxy. The significant inflows and outflows within the disk are likely caused by the dynamical action of a stellar bar and/or spiral pattern.

To evaluate in more detail whether the angular momentum transfer changes sign at characteristic dynamical locations within the disk, we derived the corotation resonance (CR) radii as described in Section 4.3 (see Table 9 for an overview of all CR radii for our galaxies). The CR radius is defined as the radius where the density wave pattern (e.g., bar, spiral) and the differentially rotating disk have the same angular velocity. This leads to a gain of angular momentum outside and loss of angular momentum inside the regions close to the CR radius. Since galaxies can harbor several spiral and/or bar patterns, also multiple CR radii can exist within one galaxy. In Table 9, we listed all CR radii for our galaxies with a significant phaseshift inversion.

Summarizing, almost all galaxies of our sample (except the center of NGC 5248) exhibit torque patterns typical for $m = 2$

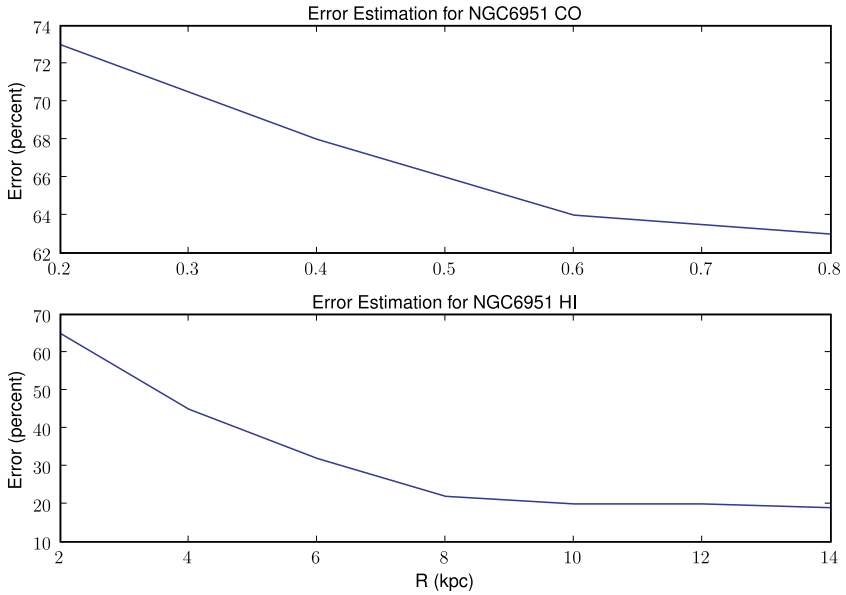

Figure 8. Error estimation for CO (top) and H I (bottom) based on radial torque calculation. The errors are the relative differences between the torque results using the best input parameters with those where typical errors of the input parameters were applied.

(A color version of this figure is available in the online journal.)

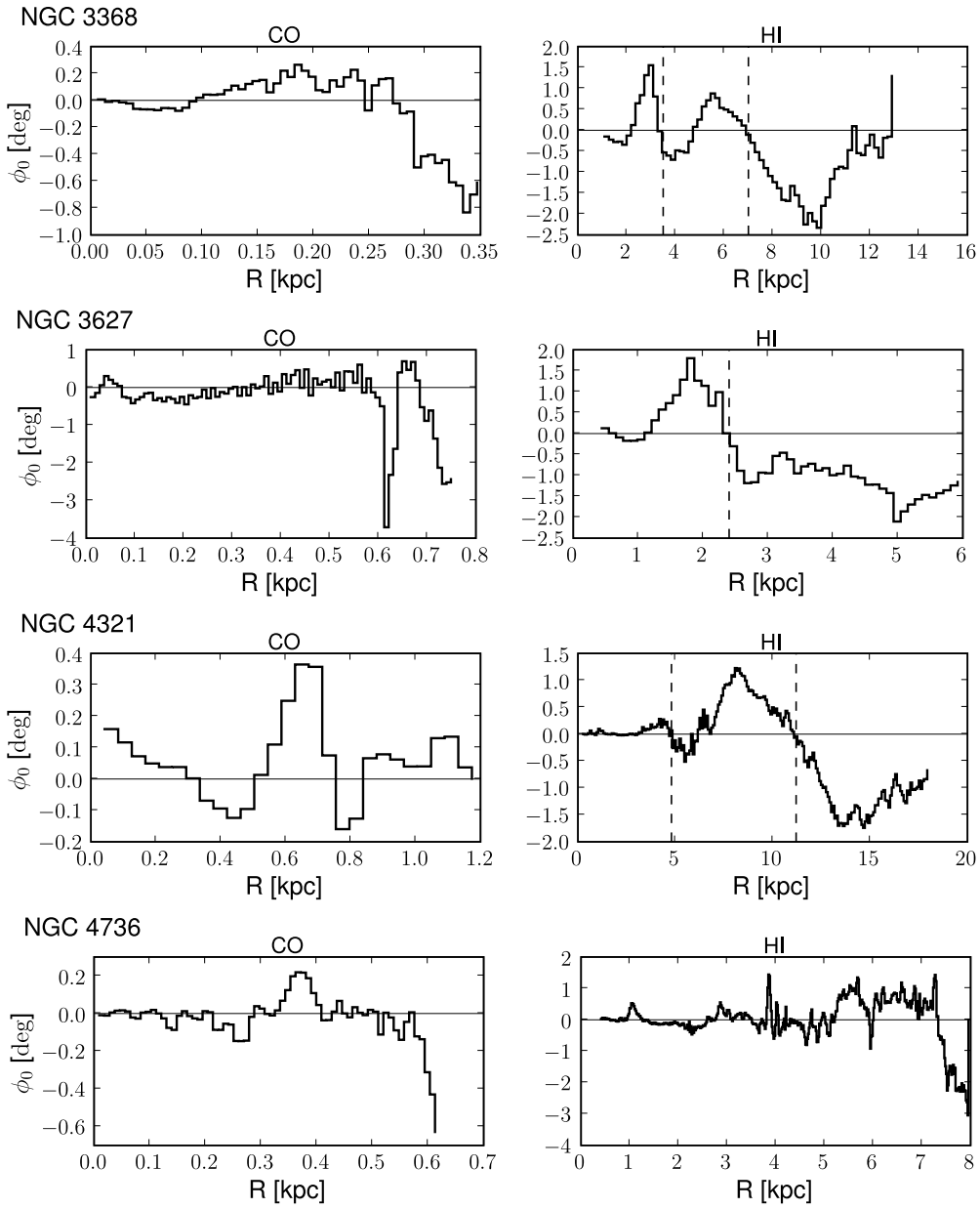

Figure 9. Overview of the phaseshift between the potential and density wave patterns for the center (left panels) and the large scale disk (right panels). The CR radii are defined as the positive-to-negative crossings of the phaseshift and indicated by dashed vertical lines.

modes (bars, spirals). NGC 3627 seems to have a very strong torque efficiency in the center ($dL/L > 0.6$) while NGC 7217 shows the lowest torque strength and angular momentum transfer in our sample. In general, we found that the transfer of angular momentum and the gas mass flow is larger in the center ($R \lesssim 1$ kpc) than in the outer disk ($R \gtrsim 1$ kpc).

5. DISCUSSION

5.1. Gas Flows in Individual Galaxies

In this section, we describe the gas flow for each of our seven galaxies and search for relations to their dynamical states and stellar and gaseous morphologies. As most of our galaxies are different in their morphology and kinematics, only case studies can provide information about the mechanisms that are acting. A general picture of the gas flow follows from a comparison of these individual studies and is described in Section 5.2.

5.1.1. NGC 3368

NGC 3368 has two stellar bars, an inner one with a radius of ∼1.0 kpc and an outer one with a radius of ∼3.2 kpc, which have a small offset of ∼25° between their PAs (see Figure 4). Two spiral arms are connected to the ends of the outer bar. The atomic gas distribution shows two gaseous spiral arms which are coincident with the stellar ones and an additional gaseous ring around the outer bar. We found that the two-dimensional torque maps of the central and the outer disk show the typical torque pattern that is expected from their stellar bars and spi-

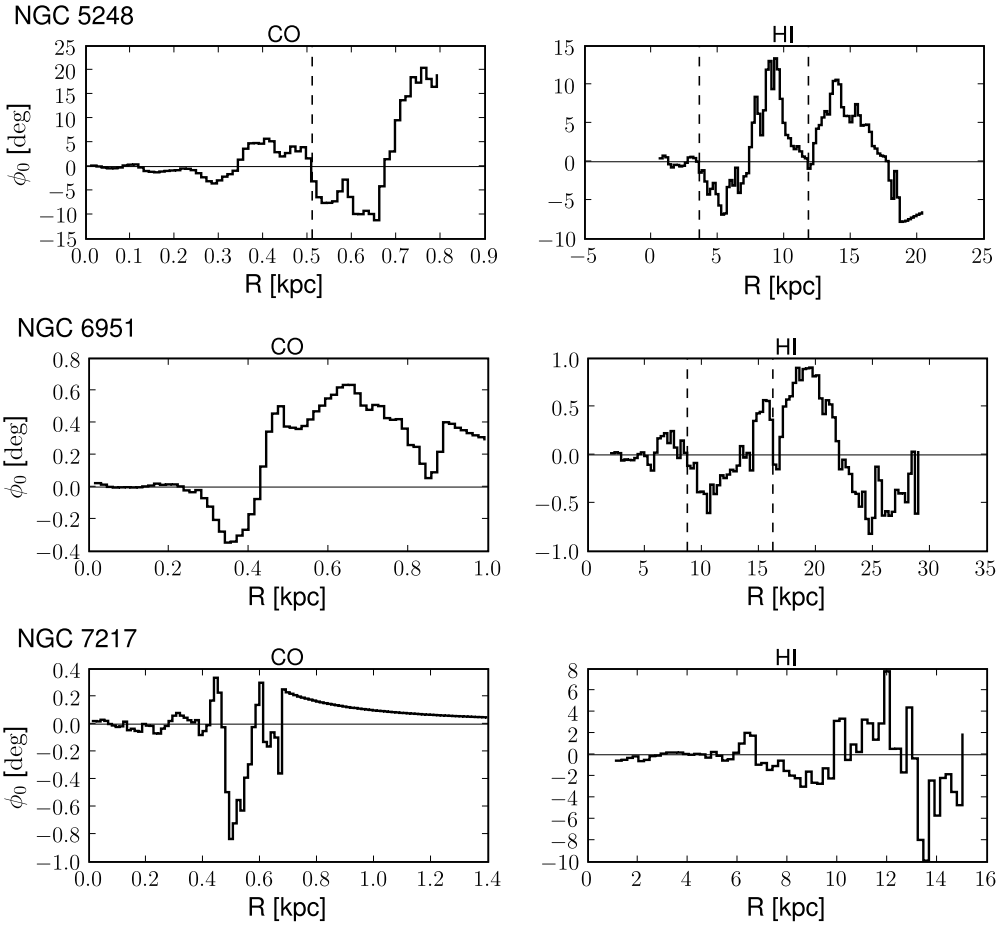

Figure 9. (Continued)

rals. On the basis of our radial torque profiles we found gas inflow for the outer disk region (7–10 kpc) with an average angular momentum transfer dL/L of 10% of the total angular momentum per rotational period at a given radius, while on intermediate disk scales (2–7 kpc) gas outflow is present (see Figure 11). Because of the switch from outflow to inflow, gas is expected to accumulate at this radius which is confirmed by our observed atomic gas distribution (see Figure 12). Interestingly, the shift at 7 kpc in the flow direction is directly contrary to the one that is expected by crossing the CR of the spiral at ∼7 kpc. The lack of a correlation between CR radius of the spiral and the expected gas flow can be likely

Table 8
Resonances

Source	$CR_{\rm Torque}$ (kpc)	$R_{\rm Bar}$ (kpc)	CR_C (kpc)	CR_{PS} (kpc)	$\Omega_{\rm Bar}$ (km s^{-1} kpc^{-1})	ILR (kpc)	UHR (kpc)	OLR (kpc)	Comments
NGC 3368	4.5	3.2	2.5–3.5	**3.5**	54	···	2.5	7.4	Outer Bar
			7	**7.0**					Outer Spiral
NGC 3627	2.7	1.5	2	**2.4**	79	···	0.4	3.7	Outer Bar
NGC 4321		5	8.5	**4.8**	39	···	1.7	13.0	Bar
	11.7			**11.2**					Outer Spiral
NGC 4736	···	···	5.5–7						Outer Oval
NGC 5248			1.7–2.0	**3.6**	41	2.3	2.7	8.9	Inner Spiral/Bar
	9.5–11	7	7.5–12	**11.8**					Outer Spiral/Bar
NGC 6951		7	5–7	**8.7**	23	(1.6, 2.5)	3.2	20.0	Bar
	11			**16.2**					Outer Resonance
			20–23	22.1					Outer Resonance
NGC 7217	5.5–7	···	···	···	···	···	···	···	No Bar or Spiral

Notes. Overview of the dynamical resonances derived from different methods: the CR radius from our gravity torque study (Column 2), the radius of the bar (Column 3), the CR using the method of Canzian (1993; Column 4), the CR on the basis of the phase-shift method of Zhang & Buta (2007; Column 5) and the associated angular speed of the bar $\Omega_{\rm Bar}$ (Column 6), the ILR at $\Omega_{\rm Bar} = \Omega - \kappa/2$ (Column 7), the UHR at $\Omega_{\rm Bar} = \Omega - \kappa/4$ (Column 8), and the OLR at $\Omega_{\rm Bar} = \Omega + \kappa/2$ (Column 9) of the bar. All radii are deprojected. The CR values printed in boldface are taken for further interpretation of our torque results as a function of the CR locations of spiral arms and bars.

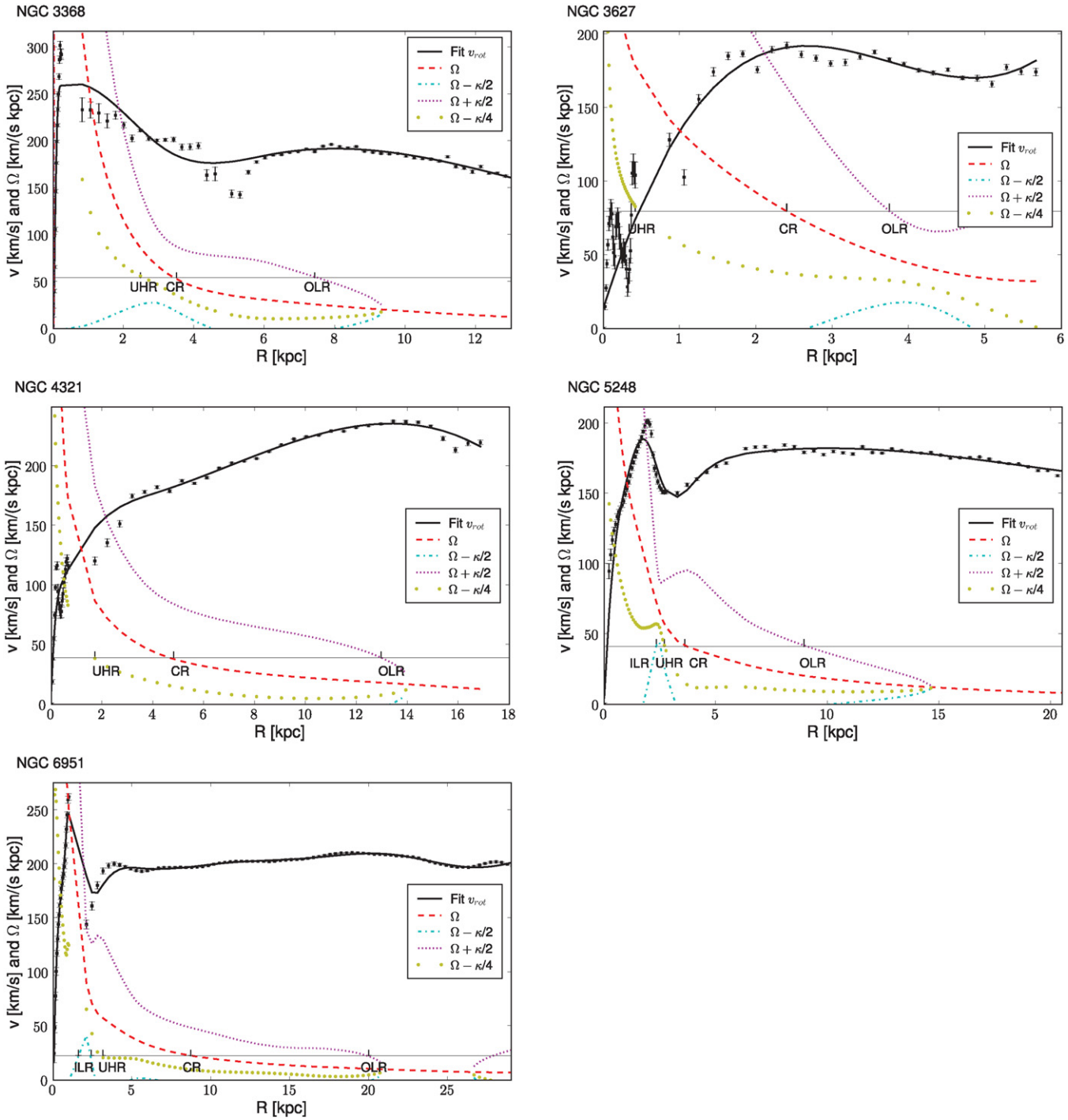

Figure 10. Overview of the CR of the bar and the associated bar pattern speed $\Omega_{\rm Bar}$ (horizontal solid line; see also Table 8), the ILR at $\Omega_{\rm Bar} = \Omega - \kappa/2$, the UHR at $\Omega_{\rm Bar} = \Omega - \kappa/4$, and the OLR at $\Omega_{\rm Bar} = \Omega + \kappa/2$ of the bar. The angular velocity Ω is calculated from a fit using a cubic spline interpolation (solid line) to our measured CO and H I rotation curve (points with error bars). NGC 4736 and NGC 7217 are not shown here as no large-scale bar or oval is present in these two galaxies. (A color version of this figure is available in the online journal.)

explained by the fact that the bar potential is still acting at this location and overlaps with the spiral pattern. The UHR ($R \simeq 2.5$ kpc) and OLR ($R \simeq 7.5$ kpc) of the bar seem to correlate with an expected accumulation of gas at $R = 2.5$ kpc and $R = 8$ kpc, respectively, also clearly visible in the radial atomic gas density profile (see Figure 12). For the center we found a large gas inflow from 2–0.08 kpc, that seems to transport the gas toward the AGN. Only for the very center from 0–0.08 kpc gas outflow is present, suggesting an accumulation of gas at a radial distance of 0.08 kpc, which is also visible as a small bump in the radial molecular gas density profile (see Figure 12).

5.1.2. NGC 3627

The stellar distribution of NGC 3627 exhibits two bars with a radius of 1.5 kpc and 0.2 kpc and two spiral arms at the ends of each of the bars. As the two bars have an offset between their PAs of ∼45° a possible decoupling of these two dynamical modes might influence the gas kinematics (S. García-Burillo

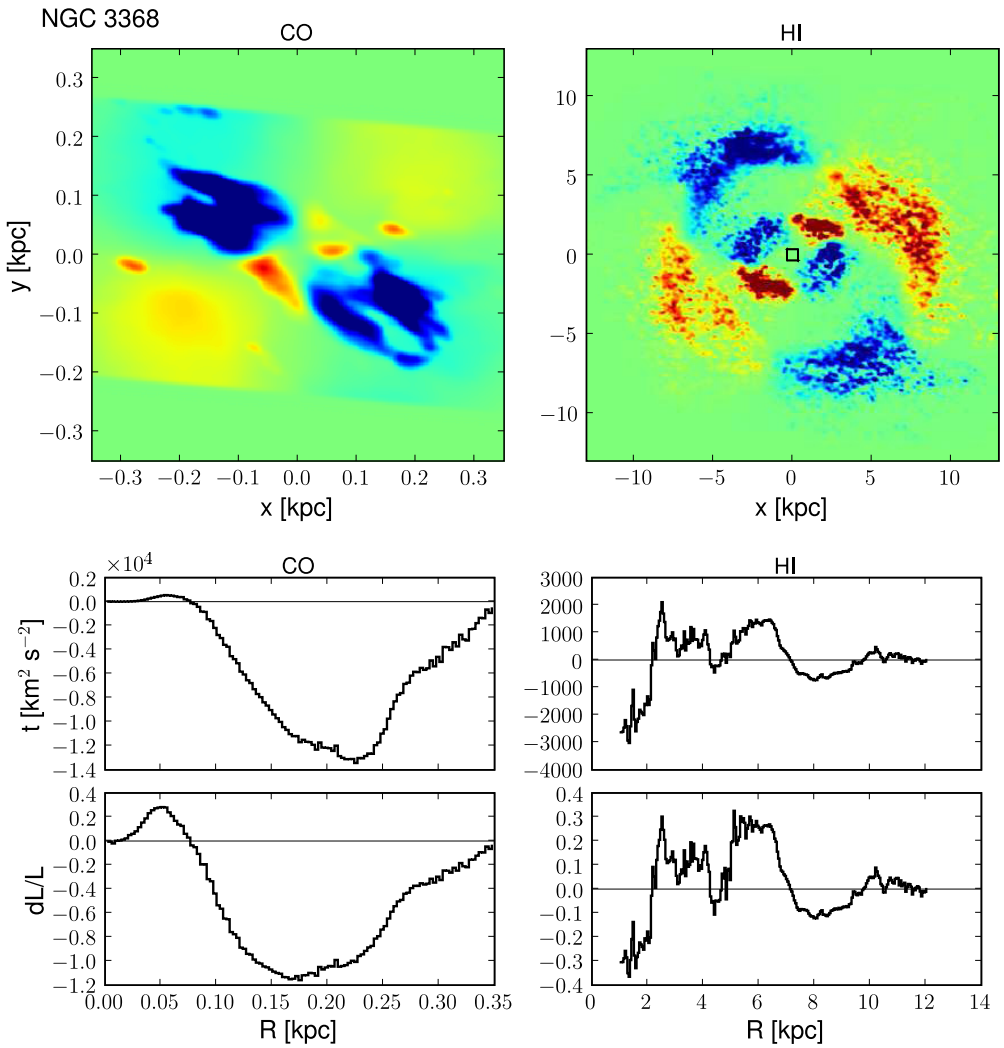

Figure 11. Overview of the torque results for the central (CO, left panels) and the large scale disk (H I, right panels). A positive (red colored) or a negative (blue colored) torque corresponds to an outflow or inflow of gas, respectively. The top panels show the gravitational torques weighted with the CO- (left top panel) and H I- (right top panel) gas column density and normalized to their the maximum values. The square in the H I-weighted torque map (right top panel) indicates the FOV of the CO-weighted torque map. The torque per unit mass averaged over azimuth $\tau(R)$ and the fraction of angular momentum dL/L transferred from/to the gas in one rotation are shown in the center and bottom panels, respectively.

(A color version of this figure is available in the online journal.)

et al. 2008, in preparation). We found that the torque pattern reflects the shift of the PAs between these two bars. For the outer disk the torques are dominated by the potential of the spiral arms with a CR radius at 2.5 kpc. Within this CR radius the gas is transported inward, while moving outward outside the CR radius, which is confirmed by our radial torque profile: a significant inflow ($dL/L \simeq 0.3$) from 2.8–0.7 kpc and outflow of gas ($dL/L \simeq 0.3$) from 2.8–5 kpc. For the central disk traced by our CO observation we found a large gas outflow ($dL/L \simeq 0.4$) from 0–0.5 kpc. Thus, gas accumulation might be possible at ∼0.5 kpc where the flow direction switches from outflow to inflow, which is also visible as a small peak in the radial molecular gas density profile (see Figure 12). This gas accumulation at ∼0.5 kpc seems also to overlap with the UHR of the outer bar at $R = 0.45$ kpc.

5.1.3. NGC 4321

The inner region of NGC 4321 has been extensively studied in the NIR (Knapen et al. 1995a, 1995b) and shows a prominent nuclear bar aligned with the large-scale stellar bar. The large-scale bar is coupled to four spiral arms. The gas flow follows the spirals in the outer disk and is increasingly dominated by the torques caused by the bar toward the center. For the outer disk (from 12–18 kpc) we found a significant outflow ($dL/L = 0.2$) and on intermediate scales (from 12–6 kpc) inflow. The switch from inflow to outflow is roughly occurring at the CR radius of the spirals at 11.2 kpc. At the CR radius of the bar no switch from inflow to outflow is found, suggesting that the standard CR determinations are not applicable for this case because of a superposition of bar and spiral wave pattern. While a shift from outflow (0.5–0.9 kpc) to inflow (1.0–0.9 kpc) is present at 0.9 kpc, no significant angular momentum transport occurs toward the very center of the galaxy (from 0.5–0 kpc). The comparison with a previous gravity torque study only for the center (García-Burillo et al. 2005) revealed a similar torque pattern but larger amplitudes. Although similar methods have been used, the difference in the amplitude can be likely explained by differences in the geometric parameters used for the disk (i, PA, and center) as well as a different method for the scaling with the mass-to-light ratios (García-Burillo et al. 2005: constant scaling; our study: scaling as function of radius).

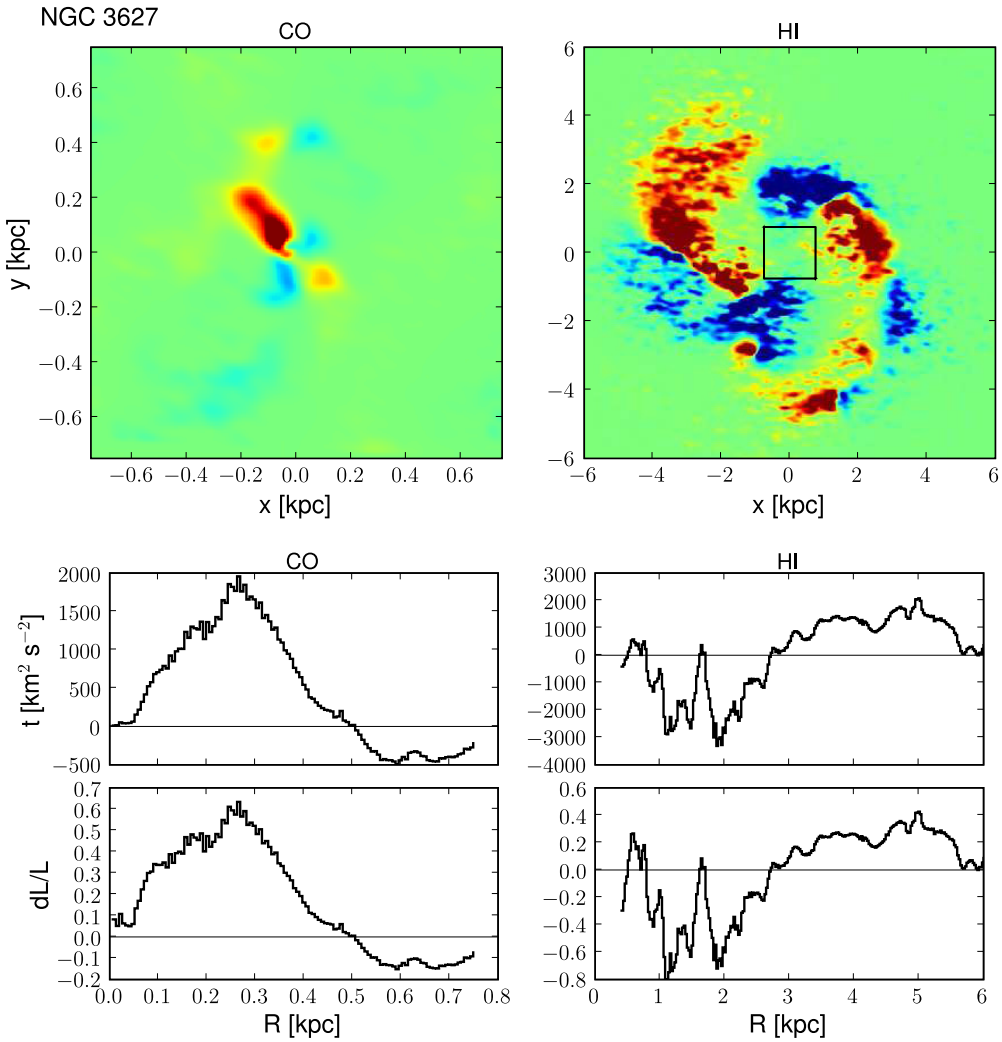

Figure 11. (Continued)

5.1.4. NGC 4736

For NGC 4736, we found that the direction of the torque rotates by about ∼60° in the region of 2–0 kpc. This is likely due to the presence of two oval stellar distributions whose major axes have an offset of ∼60° suggesting a decoupling between these two dynamical modes. These ovals are clearly visible in the NIR images (see Figure 4). The gravitational torque caused by the outer oval is still dominant in the region of the large gas spiral at 6.2 kpc producing a net outflow at this location (5.5–7 kpc). Averaged over the entire atomic gas disk, gas is transported outward.

5.1.5. NGC 5248

NGC 5248 shows a prominent stellar large-scale bar (Jogee et al. 2002a) visible in the NIR image and in the gaseous distribution as well (Haan et al. 2008). Further, two inner stellar spiral arms are present within the bar (Jogee et al. 2002b) and two outer ones continue from the ends of the bar to the outer disk at 15 kpc. The gravitational torque pattern seems to be a mix between the bar and spiral arm contributions. In particular, the outer disk exhibits an additional torque concentration at the end of the north-western spiral arm at a distance of 7 kpc from the center. For the outer disk we found outflow at distances from (11–15), (2–8) kpc, and inflow between ∼(11–8) kpc. The gravitational torques in the center are very small (maximum of $dL/L = 0.04$) and show no typical torque pattern for a bar or oval. Instead a bipolar pattern is present, but might be caused by a possible offset between the real center and our used values (see Section 4.2) or is alternatively suggesting the presence of a lopsided disk. Interestingly, NGC 5248 is the only galaxy in our sample without AGN activity, which might be linked to the absence of gravitational torques and/or a possible lopsided disk in the center. However, to test this finding in detail higher spatially resolved data of the molecular gas distribution with ∼0.″5 is necessary as for this galaxy only BIMA-SONG data with 6.″1 was available for our study.

5.1.6. NGC 6951

NGC 6951 is a representative galaxy with a combination of AGN activity, stellar bars (inner and large-scale) and spiral arms (visible in NIR image and H I map). The gas flow pattern from 15–28 kpc reflects the stellar spiral arms and is increasingly dominated by the gravitational torques caused by the bar toward the center (see Figure 11). The molecular gas distribution in the center shows two gaseous spiral arms whose gas flow underlie the gravitational torques caused by the inner bar. For the outer disk we found that the gas is transported outward ($dL/L \simeq 0.15$) from (19–27) kpc. On intermediate scales inflow occurs from (19–11) kpc, while outflow is dominant from (4–11) kpc. The radius where the gas flow is changing from inflow

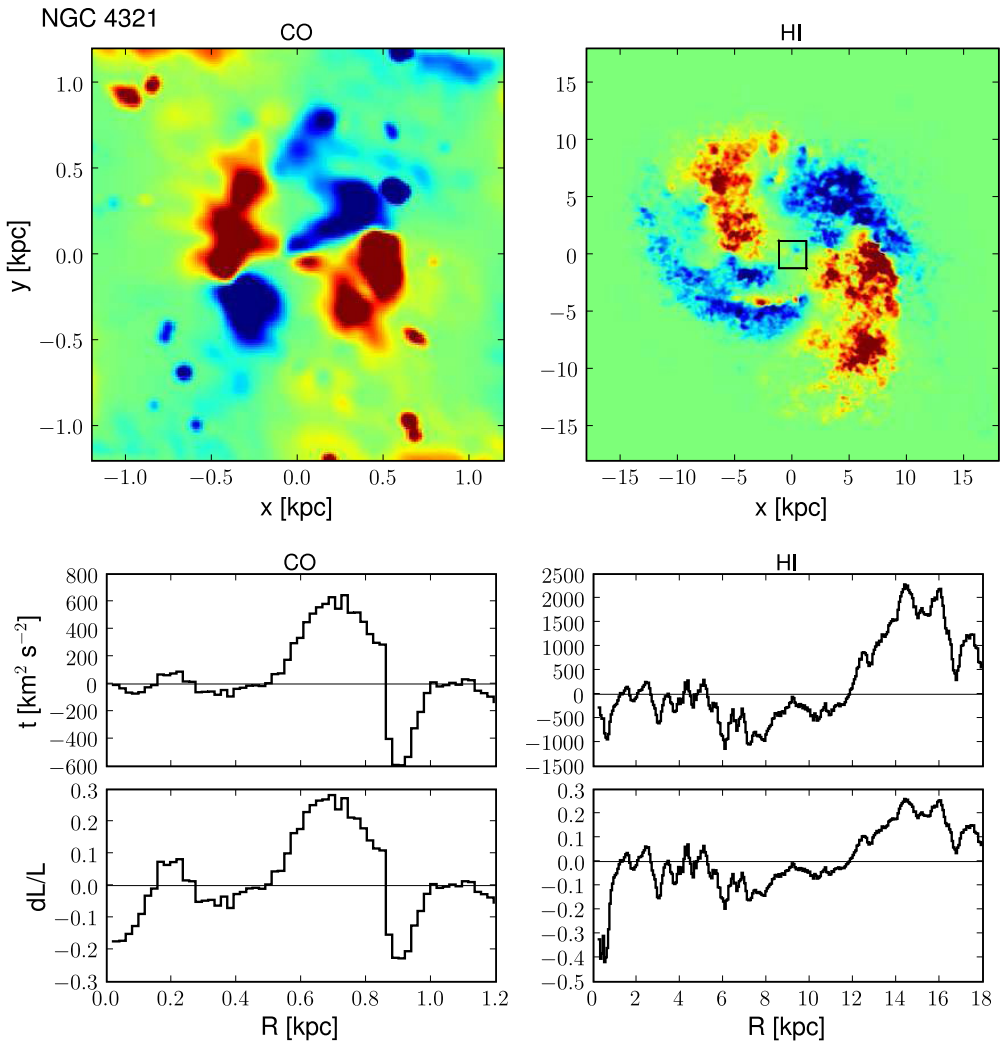

Figure 11. (Continued)

to outflow (11 kpc) does not overlap with any resonances of a single pattern (i.e., bar or spiral). We interpret this as gas is funneled inward across the CR radius of the bar (at ∼8.5 kpc) and that the gas can overcome the CR barrier. We can exclude this as being due to errors in the gravitational torque calculation or CR estimation, as neither the errors of our torque study (see Section 4.2) are large enough to eliminate such a significant inflow on the scale between (5–11) kpc, nor the possible range in the CR estimation of (5–9) kpc (including errors) could shift the CR radius to the switch from inflow to outflow at 11 kpc. Also viscous torques are not efficient enough at these large scales to change the flow direction, because of much smaller gas densities than in the center. The most likely explanation for the mismatch between the gravitational torque induced flow direction and the standard CR estimations of the bar is the presence of several pattern speeds (i.e., for bar and spiral wave pattern) that combine and allow the gas to overcome the standard CR barrier of a single pattern. For the center we found gas inflow from (0.8–0.45) kpc and outflow from (0.3–0.45) kpc, suggesting a gas accumulation at ∼0.45 kpc. This is roughly coincident with a significant peak in the radial gas density profile at this location (at 0.38 kpc) leading to two inner molecular gaseous spiral arms. The comparison with a previous gravity torque study only for the center (García-Burillo et al. 2005) revealed a similar torque pattern but much larger amplitudes than our study (about a factor of 5–10). This difference in amplitude might not only be caused by differences in the used geometric parameters of the disk (*i*, PA, and center) as well as a different method for the scaling with the mass-to-light ratios, but eventually also by the use of different NIR images (García-Burillo et al. (2005): J-band; our study: K-band). We tested our code with the NIR image and parameters used by García-Burillo et al. (2005) and found similar torque values as in García-Burillo et al. (2005), so that an error in our code can be excluded.

5.1.7. NGC 7217

The two-dimensional torque map shows a pattern typical for an oval potential. Although NGC 7217 has no bar, an oval stellar distribution is possible; however, it might be just an deprojection effect due to uncertainties in the inclination angle. The latter case seems to be plausible as the torque pattern is aligned with the major axis (PA = 265°5) in such a way as expected from an error in inclination angle (see Section 4.2). For the outer disk we found no strong evidence for gas transport caused by the gravitational torque. At the center we found only small evidence for gas inflow from (0.5–0.2) kpc with a maximum of $dL/L = 0.1$, but this is presumably due to the uncertainty in the inclination angle.

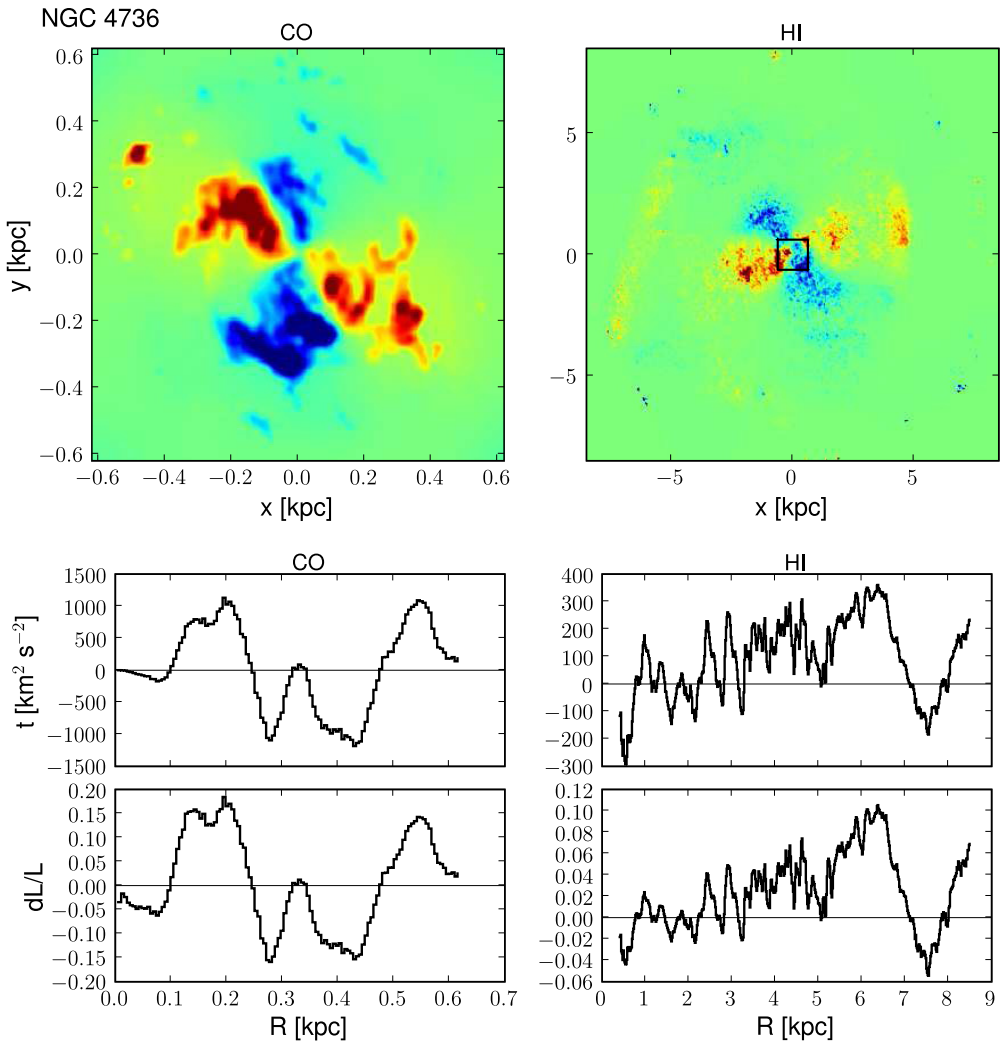

Figure 11. (Continued)

5.2. A General Picture of the Gas Flow from the Outer Disk to the Center

We found that the typical torque pattern changes sign in four quadrants. This typical butterfly pattern is characteristic for the action of an oval or barred gravitational potential. The orientation of the torque pattern in the center is coincident with the one of the outer disk (except for NGC 4736). Toward the outer disk, the gas flow is governed by the action of the stellar spiral arms, if present, which cause a positive (negative) torque on the side of the spiral arms toward (away from) the galaxy center. Thus, we conclude that for almost all galaxies in our sample a dominant $m = 2$ mode is present and has roughly the same orientation in the outer disk and the center. We found nested bars within large-scale bars for NGC 3368, NGC 3627, NGC 4736 whose major axes have an offset of 25°–60° to the large-scale bars. No signs for unidentified patterns (i.e., not showing up as a prominent feature in the NIR images) are found in the torque maps.

The radial profiles of dL/L and $d^2M(R)/(dRdt)$ reveal that torques are more efficient in the redistribution of gas in the center of galaxies than in the outer disks, presumably due to larger gravitational torques induced there by the bar component. We found for a majority of our galaxies (5/7) a significant reversal from outflow to inflow in radial direction at radial distances ranging between (0.1–0.9) kpc, leading to an increasing gravitational pressure on the gas at this position due to gravitational torques and in the case of stable orbits to an accumulation of gas at this position. A comparison of our radial gas density profiles and the torque profiles revealed for most of the outer disks (H I density) no correlation while for some central disks (CO density) an overlap or a shift between both profiles is found (see Figure 12 and Section 5.1). A possible explanation is that gravitational torques will redistribute the gas within a few orbital rotation periods. As the transport of angular momentum per rotation period is on average ∼0.3, the expected timescale for the redistribution of the total angular momentum for a given radius is ∼3 rotation periods (≅ 3×10^7 yr at a radius of 0.5 kpc). Another explanation might be that the gas is consumed in star formation and hence does not accumulate as expected. For the very center (0–0.1) kpc we found no significant gas transport toward the AGN due to gravitational torques, suggesting that other torques such as viscous torques might be become important for fueling the AGN (see also García-Burillo et al. 2005).

In the dynamics of galaxies the CR radius is expected to separate inflow (between ILR and CR) from outflow (between CR and OLR). However, in all galaxies of our sample the CR radius of the bar does not correlate with any inflow/outflow separation and thus, sets no barrier for gas transport within

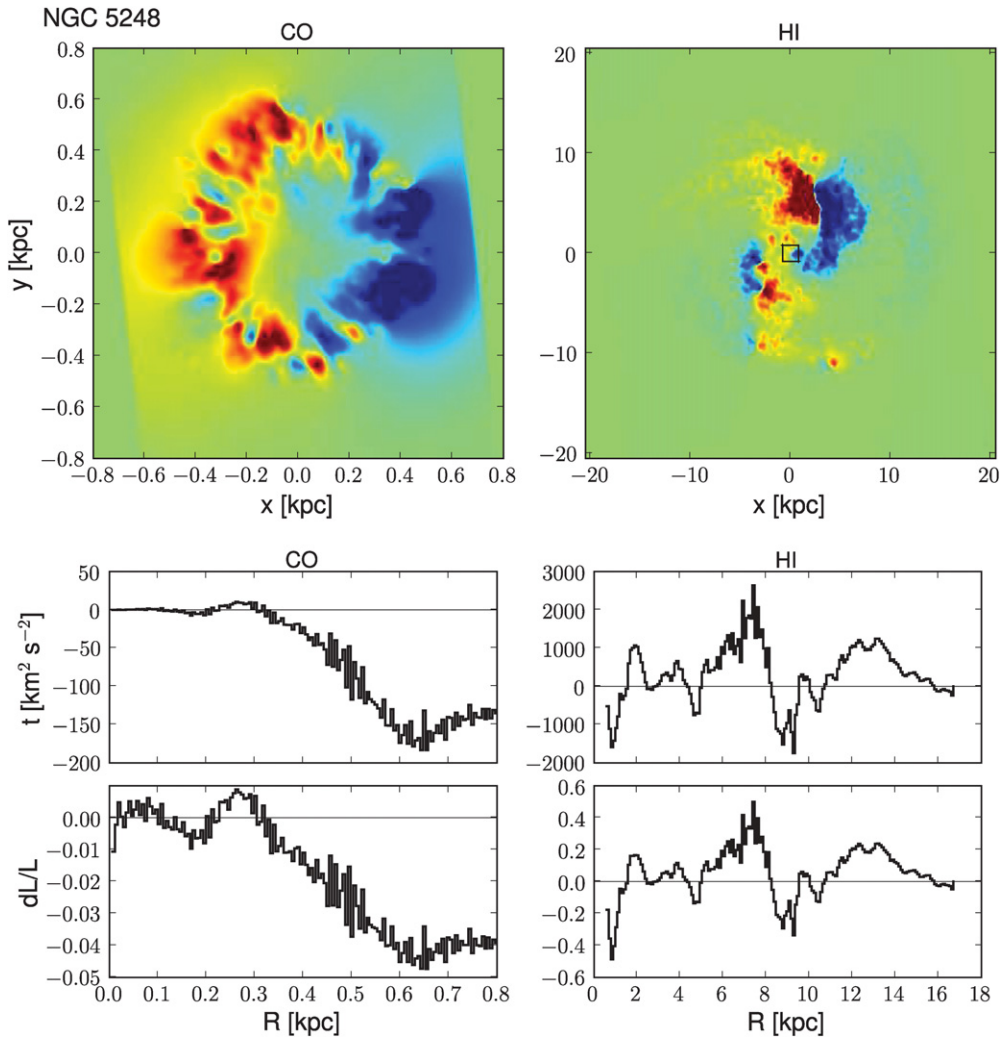

Figure 11. (Continued)

the disk. This contradiction can be possibly explained by a coupling of dynamical modes, e.g., of a spiral and a bar or an oval potential. Thus, the orbital paths of the gas may change in comparison to the orbits of a single dynamical mode and allow the transport of gas across the CR. A similar case has been evolved for NGC 4579 which shows a transportation of gas inward across the CR of the bar, but in this case, due to (morphological) decoupling of bar and spiral pattern on different spatial scales S. García-Burillo et al. (2008, in preparation).

With regard to the CR of a spiral pattern, most of our galaxies with spirals (NGC 3627, NGC 4321, NGC 5248) show a correlation between CR radius of the spiral and a reversal of inflow/outflow of gas due to gravitational torques. Only for NGC 6951 no correlation is found. Instead a significant outflow due to gravitational torques occurs at the CR radius of the spiral, suggesting that the bar potential is still acting at this radius and may overlap with the one of the spiral pattern. Further, the OLR of the bar (18.6 kpc) does not overlap with the CR of the spiral and, thus, seems to substantiate the dominance of the bar for NGC 6951. Also for NGC 3368, NGC 4736, and NGC 7217, which have none or only very weak stellar spiral arms, the gravitational torque is dominated by a bar or oval potential.

Summarizing, gravitational torques can be very efficient in transporting the gas from the outer disk to the center at ∼100 pc. Due to a dynamical coupling of bar and spiral arms, the gas can bridge even resonances such as the CR of a bar (which could act as a natural barrier for further gas inflow).

5.3. Comparison between Gravitational and Kinematic Derived Gas Flows

5.3.1. Estimation of Radial Motion

In general, one would expect that gas inflow/outflow should also be recognizable in the velocity field of a galaxy. In practice, to determine radial gas flow from the line-of-sight velocity alone is very ambitious and controversial (for an overview see Wong et al. 2004). The main reason is that the dominant contributor to noncircular motions (see the following section) in a bar or spiral potential seems to be elliptical streaming which cannot be used by itself to derive net inflow/outflow without further assumptions. One of the most promising attempts to derive radial gas motion was conducted by Wong et al. (2004) using the variations of the first- and third-order sine coefficients (s_1 and s_3) as a function of radius to provide a basic approach to diagnose various types of noncircular motions (see for more details Wong et al. 2004): warp streaming (i.e., motion out of the plane of the disk; correlation between s_1- and s_3-term, with a slope $ds_3/ds_1 > 0$), elliptical or spiral streaming (anticorrelation between s_1- and s_3-term, with $ds_3/ds_1 < 0$), and radial inflow

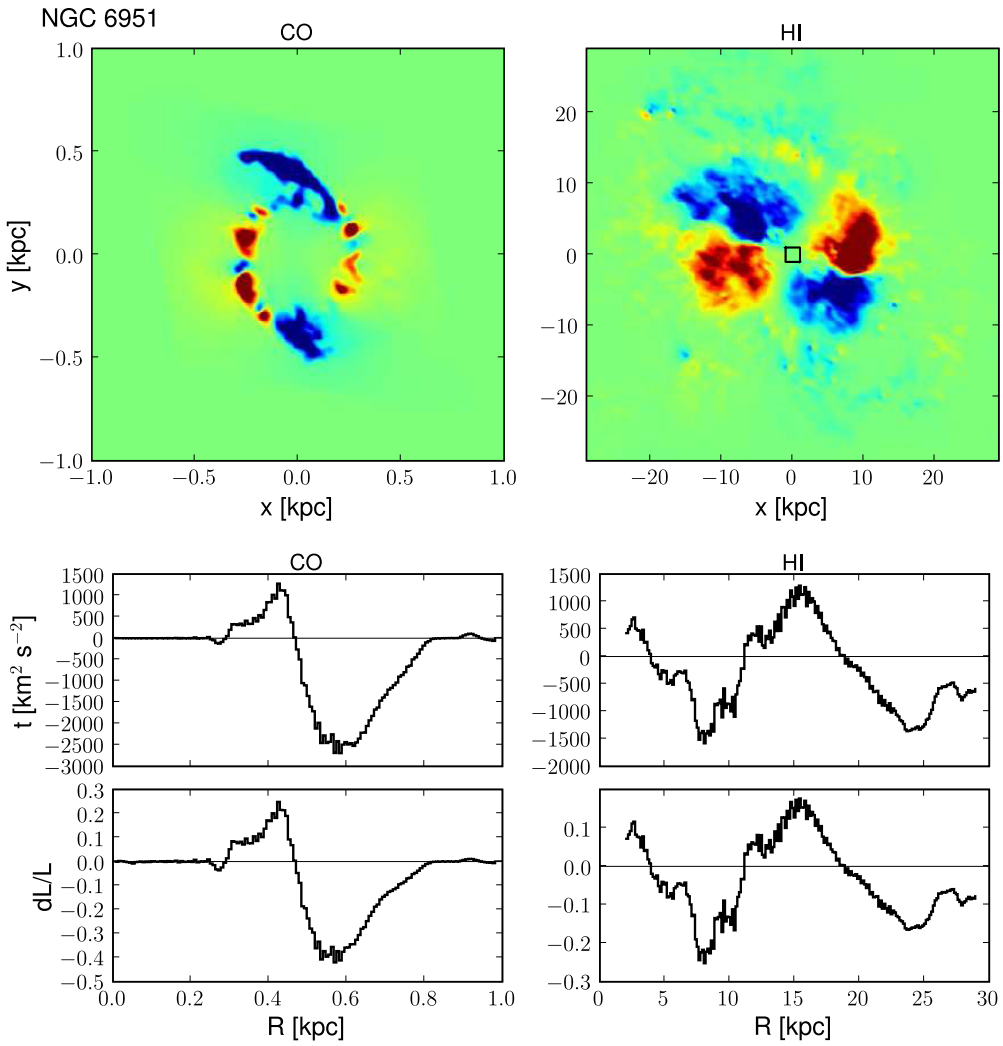

Figure 11. (Continued)

($s_1 \gg s_3$). Note that these criteria are very idealized and do not permit a clear distinction between the models when applied to real galaxies. However, to definitely test whether this method can clearly identify radial gas motion or not, we have compared the radial gas flows derived from our velocity fields (see Section 3.2) with the inflow/outflow rates due to gravity torques (see Section 4.4).

We have used the following convention (following the method of Wong et al. 2004): if the s_1-term is interpreted as radial gas flow (for $s_1/s_3 \gg 1$), a positive (negative) sign of the s_1 amplitude corresponds to gas outflow (inflow) for a counter-clockwise rotating galaxy. We derived the sense of rotation for our galaxies by presuming that spiral arms seen in the optical images are always trailing. In order to have a consistent label-

Table 9
Gravitational Torque Analysis

Source	$\langle dL/L \rangle$		$\langle \lvert dL/L \rvert \rangle$		$dM_{\rm HI}/dt$	$dM_{\rm mol}/dt$	$R_{\rm max,HI}$	$R_{\rm max,CO}$
	H I	CO	H I	CO	($M_\odot$ yr^{-1})	($M_\odot$ yr^{-1})	(kpc)	(kpc)
NGC 3368	0.02	−0.50	0.12	0.55	0.04	−11.11	13.0	0.35
NGC 3627	−0.00	0.16	0.26	0.24	−0.10	50.13	6.0	0.75
NGC 4321	0.01	0.02	0.10	0.10	−0.18	1.03	18.0	1.2
NGC 4736	0.02	0.01	0.03	0.09	0.06	−0.01	8.5	0.62
NGC 5248	0.06	−0.02	0.13	0.02	0.49	−22.96	20.5	0.8
NGC 6951	−0.04	−0.05	0.09	0.10	−0.16	−4.29	29.0	1.0
NGC 7217	−0.01	−0.02	0.03	0.03	−0.01	−2.37	15.2	1.4

Notes. Overview of the transferred angular momentum and averaged transferred gas masses over the entire gas disk for the center (molecular gas traced by CO) and the outer disk (atomic gas traced by H I). A positive (negative) sign corresponds to a net outflow (inflow). The averaged transferred angular momentum $\langle dL/L \rangle$ over the entire gas disk is listed in Columns 2 and 3 and the mean value of the absolute angular momentum transfer within the disk in Columns 3 and 4. The net mass inflow/outflow rates $dM(R)/(dt)$ (in units of $M_\odot$ yr^{-1} pc^{-1}) out to the maximum disk radius (Columns 8,9) are listed in Column 6 (7) for the atomic (molecular) gas.

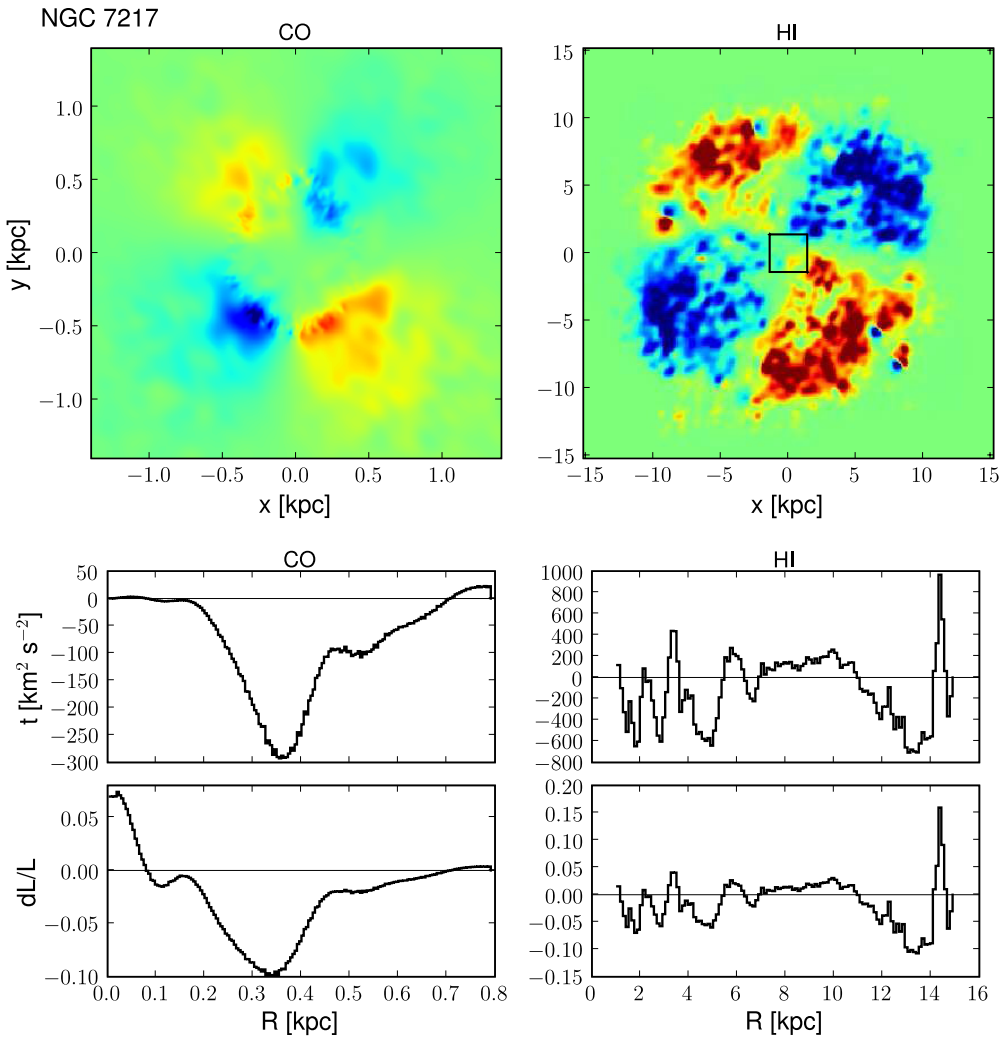

Figure 11. (Continued)

ing we defined $s_1^* = s_1$ $(-s_1)$ for counterclockwise (clockwise) rotation, so that $s_1^* < 0$ corresponds to gas inflow (see third panel of Figure 3). In the following, we discuss some candidate regions for inflow/outflow: NGC 3627 and NGC 4321 exhibit a significant negative s_1 term at 0–0.15 kpc and 0.2–0.8 kpc, respectively, which indicates radial inflow at these scales. In contrast, we found for these regions significant outflow rates from our gravitational torque analysis. Further, the outer disk of NGC 6951 shows a significant negative s_1 term (indicates inflow) at (15–18) kpc, while the torque analysis reveals significant outflow ($dL/L = 0.1$). Summarizing, we found no correlation between the candidate radial flow regions from our kinematic study and the inflow/outflow caused by gravitational torques. Thus, we conclude in agreement with other studies (e.g., Wong et al. 2004) that the noncircular terms are predominantly caused by elliptical streaming motions and cannot be used as indicator alone for possible radial inflow/outflow of gas.

5.3.2. Streaming Motions versus Radial Inflow/Outflow

As an alternative to radial gas motion where the gas looses or gains angular momentum, gas clouds with streaming motion can follow under certain assumptions closed orbits and no angular momentum is transferred when collisional shocks and other nonlinear effects are excluded. For instance, if the principal axes of an elliptical orbit are aligned with those of a stellar bar, the phase shift between the bar and the gas is zero and hence no inflow will occur at all, but still strong streaming motions are present. To produce a net inflow/outflow a phase shift between the gas and the potential is required. Streaming motions are present in $m = 2$ perturbation such as in a barlike potential where the gas follows elliptical closed orbits or in a two arm spiral density wave where a phase shift occurs that varies as a function of radius. This collisionless orbit approximation can be simple described by first order Fourier terms (Franx et al. 1994). In a realistic treatment the nonlinear effects will contribute additional Fourier terms and elliptical streaming motions may overlap with radial gas flow.

To estimate a possible dependence of streaming motion on pure inflow/outflow rates, we have conducted the following study. If we assume that the noncircular motions derived from our kinematic harmonic decomposition are dominated by elliptical streaming, it is possible to compare the amplitude of noncircular motions $v_{nc}/v_{\rm rot}$ as tracer for elliptical streaming with the amplitude of angular momentum transport caused by gravitational torques $\langle |dL/L| \rangle$ as a function of radius (see Figure 13). Note that the absolute scales are not really expected to be similar as they quantify different physical measurements, but indicate the significance of the values obtained with each method.

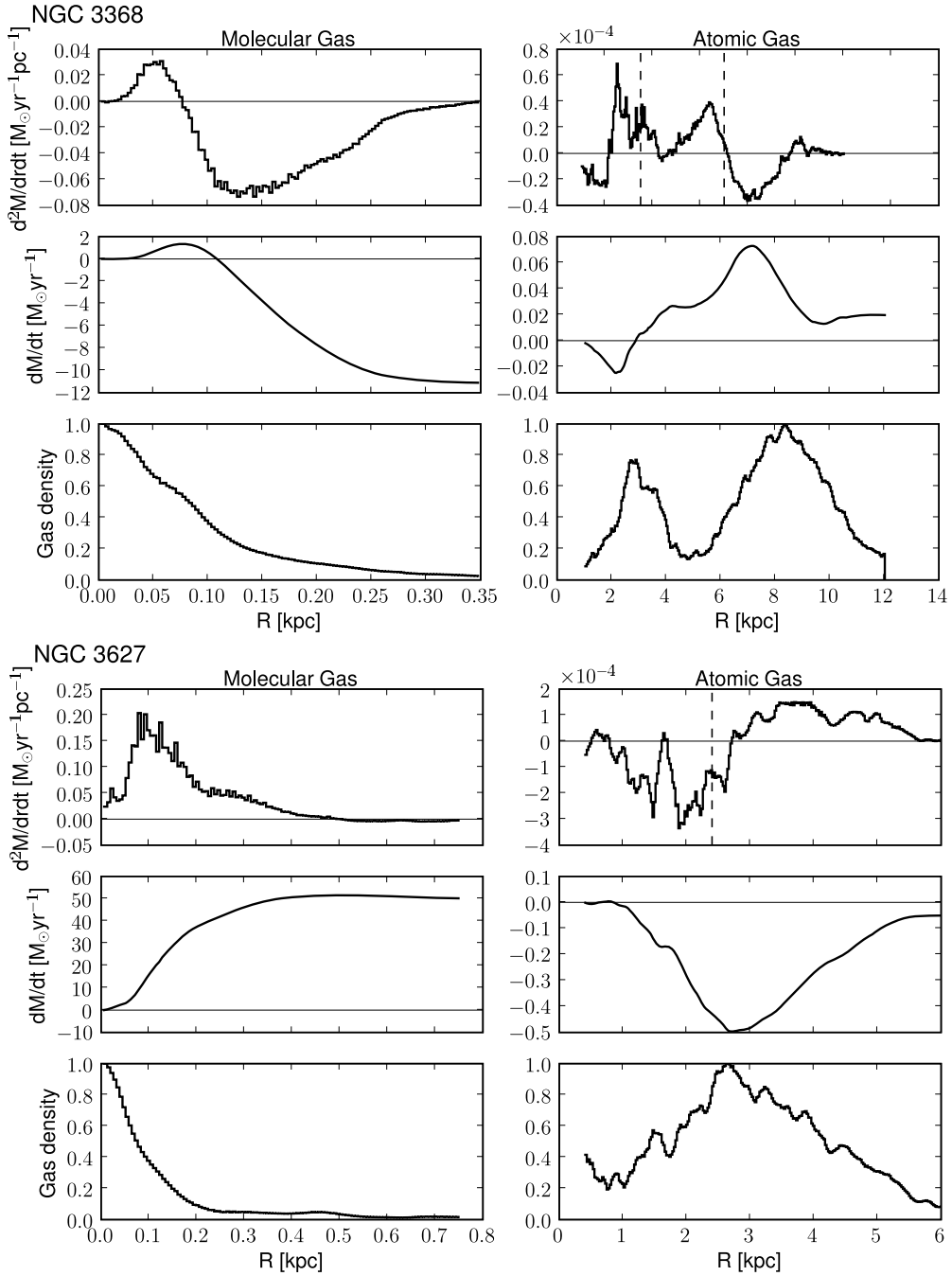

Figure 12. Overview of the mass flow rates for the molecular (left panels) and atomic gas (right panels). The upper panels present the mass flow rate of gas per unit length while the central panels show the cumulative mass flow rate of gas out to a given radius. The molecular and atomic gas densities (bottom panels) are normalized to the maximum density. The vertical dashed line indicates the CR radius of single density wave pattern (bar or spiral), if present, derived from the stellar density phase shift method (see Section 4.3).

On average, we find that the amplitude of angular momentum exchange derived from our torque analysis ($v_{nc}/v_{\rm rot} = 0.09$ for H I and $v_{nc}/v_{\rm rot} = 0.16$ for CO) is similar to the amplitude of noncircular motions obtained from our kinematic analysis ($v_{nc}/v_{\rm rot} = 0.09$ for H I and $v_{nc}/v_{\rm rot} = 0.26$ for CO). In more detail, $v_{nc}/v_{\rm rot}$ seems to be larger for the center as $\langle|dL/L|\rangle$ for most of our galaxies, except for NGC 3368 and NGC 6951. For the outer disk $\langle|dL/L|\rangle$ is larger than $v_{nc}/v_{\rm rot}$, at least for those galaxies with a bar. Galaxies without a bar (NGC 4736 and NGC 7217) exhibit very weak gravitational torques and hence small values of $\langle|dL/L|\rangle$. Interestingly, noncircular motions in unbarred galaxies have roughly the same amplitude for the outer disk than barred galaxies.

The peaks in the amplitude of noncircular motions to the amplitude of inflow/outflow seem to be correlated as a function of radius for some galaxies: center and outer disk of NGC 3368, outer disks of NGC 3627, NGC 4321, NGC 4736, and NGC 6951. Hence one might infer that noncircular motions are not pure elliptical streaming motions, but include to some extent radial motion as well. On the other hand, we found also cases with significant streaming motions but negligible inflow/outflow rates (e.g., for NGC 4736 and NGC 7217). Thus, our

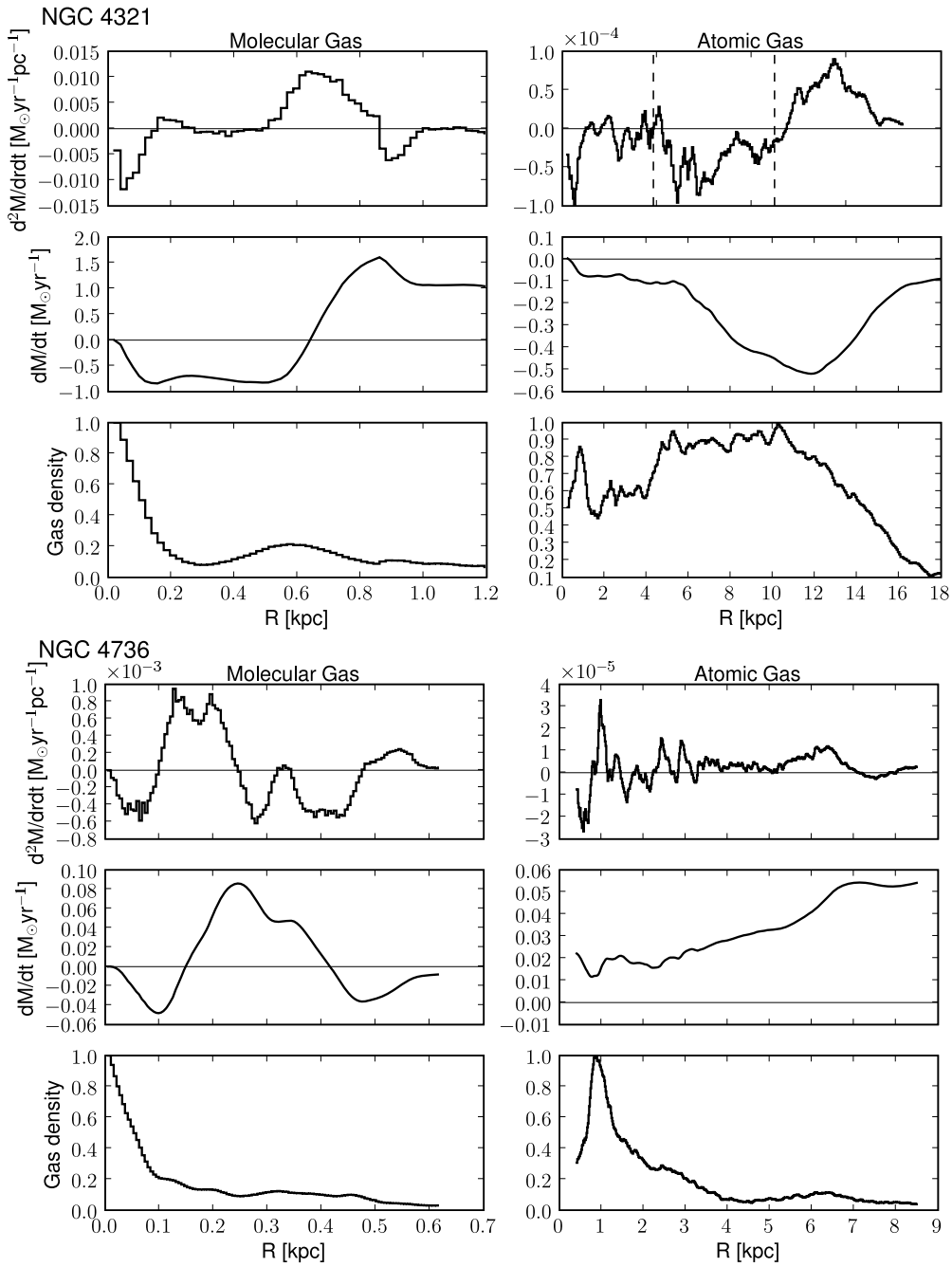

Figure 12. (Continued)

study demonstrates that signatures for streaming motions alone can not be used as reliable tracers for inflow/outflow which requires a phaseshift between the gas and the gravitational potential.

5.4. Implications for AGN Fueling

The fueling of AGN requires transportation of gas from large kpc scales down to the inner pc. To bring the gas to the center the angular momentum of the gas must decrease by orders of magnitude. Several types of gravitational instabilities, such as bars, nested bars, and spiral density waves have been proposed that might combine to transport gas from large kpc scales down to the very center (e.g., Shlosman et al. 1990; Combes 2003; Wada & Koda 2004). Inflow of gas is expected to occur mainly inside the CR radius, transporting the gas toward the ILR, where the gas might accumulate and start to form clumps of star formation. To test this scenario we have compared the gas inflow/outflow rates to the dynamical behavior of the gas at the resonances. Our results suggest for some galaxies of our sample (NGC 3368, NGC 4321, and NGC 6951) that the CR radius of the bar is overcome by gravitational torques, most likely due to a coupling of several pattern speeds (e.g., spiral arms plus bar wave pattern). Thus, the gas reservoir inside the CR can be refueled by gas from the outer disk. However, a generalization of such a scenario is not possible and detailed case studies are required to disentangle the underlying mechanisms. For example, S. García-Burillo et al. (2008, in preparation) find

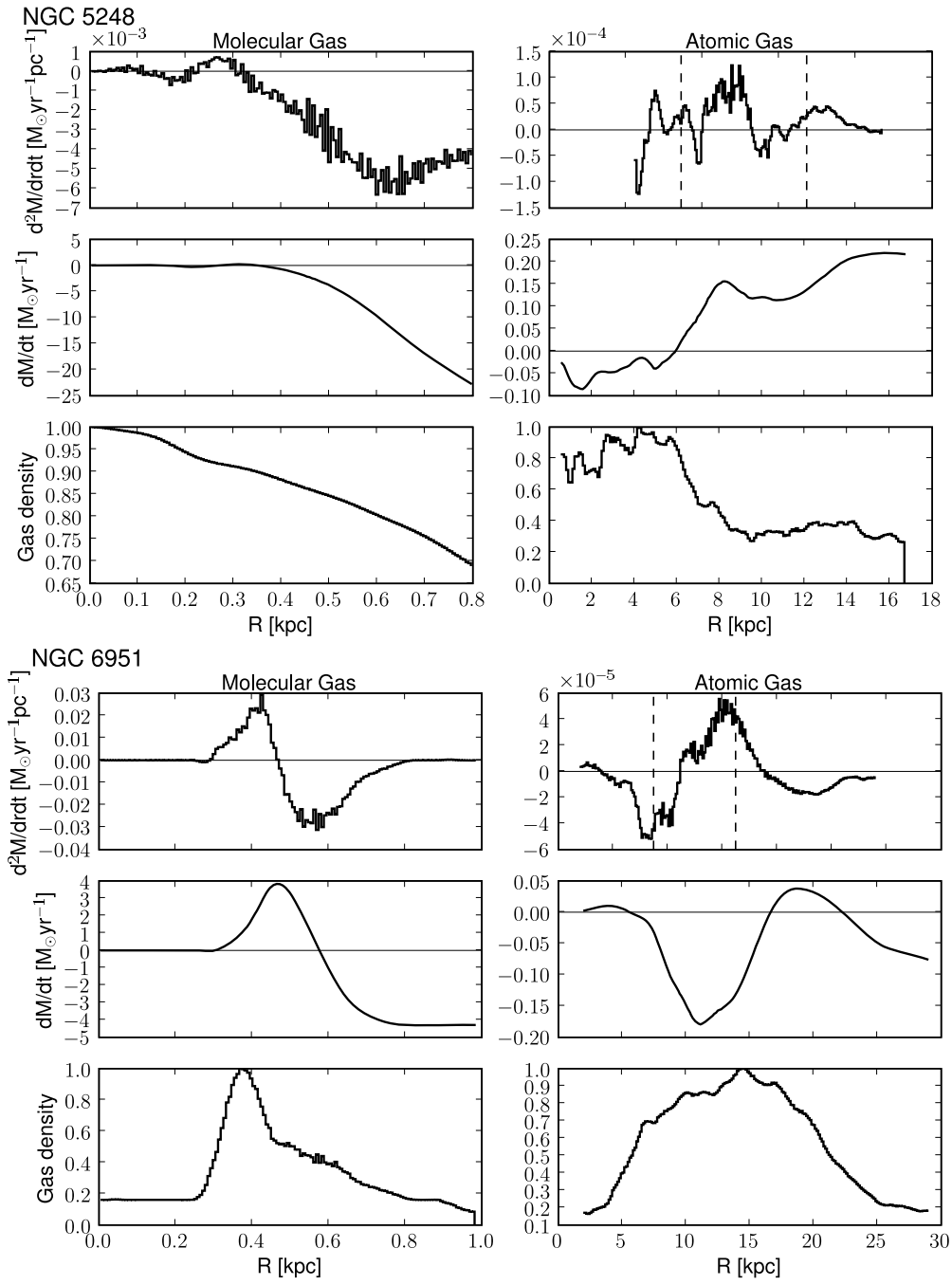

Figure 12. (Continued)

for NGC 4579 that a decoupling of bar and spiral patterns on different spatial scales allows the gas to efficiently populate the UHR region inside corotation of a bar and thus explain how the CR barrier can be crossed.

For the central disk, we found that the integrated gravitational torques indicate net outflow (two galaxies) and inflow (five galaxies) in our galaxies. In particular, NGC 3627 (Seyfert 2 type) shows a large gas outflow ($dL/L = 0.5$) inside the inner 0.4 kpc, suggesting a redistribution of the total angular momentum of the gas in ∼2.5 rotational periods at this radius ($\backsimeq 2.4 \times 10^7$ yrs). Interestingly, the kinematic analysis reveals also a large amplitude of noncircular motions ($dv_{nc}/v_{\rm rot} = 0.8$) at scales of $R \leqslant 0.15$ kpc which may substantiate this scenario.

These findings are similar to other studies of the gas flow for the molecular gas disk: a gravity torque study for NGC 6574 using CO as tracer (Lindt-Krieg et al. 2008) has shown that gas is flowing inward down to a radius of 400 pc which overlaps with a high nuclear gas concentration suggesting that the gas has been piling up at this location quite recently, since no starburst has been observed yet. An analysis of the torques exerted by the stellar gravitational potential on the molecular gas in four other (NUGA) galaxies found a mostly positive torque inside $r < 200$ pc and no inflow on these scales suggesting that viscous torques may act as fueling mechanism as well (García-Burillo et al. 2005). An explanation of this variety of morphologies might be related to timescales (García-Burillo

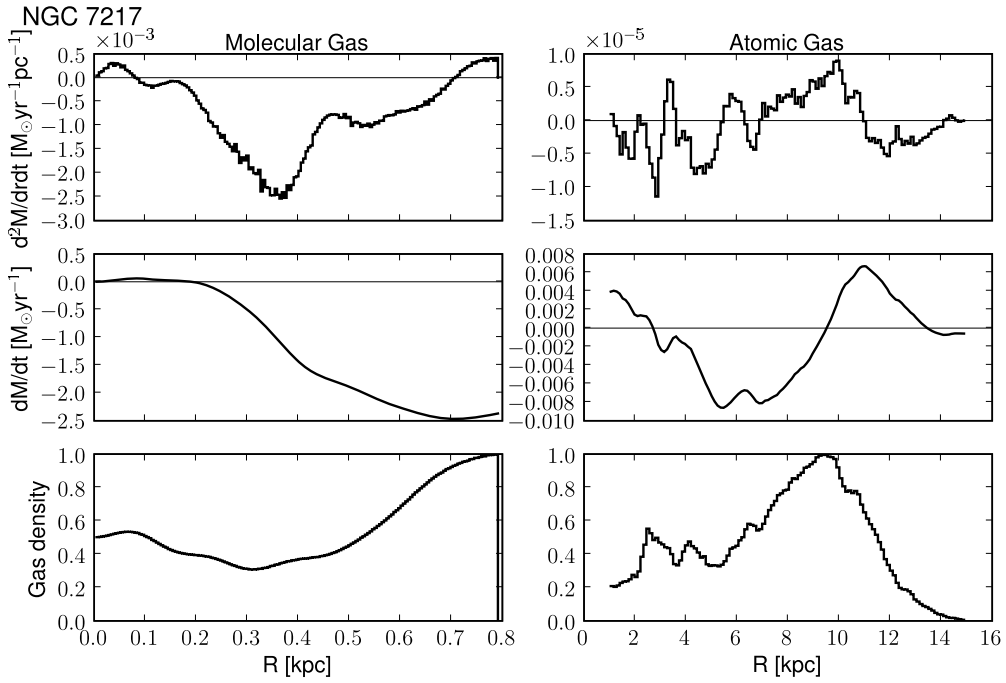

Figure 12. (Continued)

et al. 2005). In this scenario the activity in galaxies is related to that of bar instabilities, expecting that the active phases are not necessarily coincident with the phase where the bar has its maximum strength. The resulting implication is that most AGN probably occur between active accretion episodes of the galaxy disk. Evidence for such a scenario was found by Hunt et al. (2008) for NGC 2782 where molecular gas inside the ILR of the primary bar, transported by a second nuclear bar, suggests that the gas is fueling the central starburst, and in a second step might directly fuel the AGN.

The integrated gas mass transfer rates in the center range from 0.01–50 $M_\odot$ yr^{-1} based on our assumptions (see Section 4.1) and are sufficient enough to preserve AGN activity which requires typical mass accretion rates of 0.01–0.1 $M_\odot$ yr^{-1} for LINER and Seyfert activity. However, to bridge the last 100 pc to the AGN other mechanisms than gravity (e.g., viscous torques) have to play a major role, since no significant gravity torques are present at these scales (see also García-Burillo et al. 2005).

6. SUMMARY

We studied the gas flow in seven nearby galaxies to quantify the gas flow toward the center in AGN galaxies. On the basis of high angular resolution CO and H I spectroscopic data and NIR images we calculated the gravitational torques and inflow rates as a function of radius and location within the galaxies. Besides the two-dimensional gravitational torques, we applied for this study a variety of methods including a harmonic decomposition of the residual velocity field, and the Canzian and phase-shift methods to identify dynamical resonances. Our study shows that gas redistribution is very effective within the galaxy disks due to gravitational torques indicating that spiral disks are very dynamic systems that undergo strong radial evolution on timescales of a few rotation periods (e.g., $\sim 5 \times 10^8$ yrs at a radius of 5 kpc). The main results are summarized as follows:

1. Gravitational torques are very efficient in transporting the gas from the outer disk to the center (~100 pc). Typical rates for cold gas angular momentum transport per rotation are 10% of the total angular momentum at a given radius. The transported gas mass rates range from 0.01 to 50 $M_\odot$ yr^{-1}.
2. Dynamical resonances such as the CR of a bar pattern, which could act as a barrier for gas transport, are apparently easily overcome by the gas flows that are induced by gravitational torques. A possible explanation is the presence of several patterns with different speeds (e.g., bar and spiral wave pattern) that combine and allow the gas to overcome the standard CR barrier of a single pattern.
3. The transport of angular momentum, and thus, the inflow/outflow rates, are larger for the central (<1 kpc) than for the outer disk (1–20 kpc), suggesting stronger gravitational torques induced by bars in the center of galaxies.
4. In our sample the dominant dynamical mode is $m = 2$ (e.g., bar, oval, two-armed spiral arms) and has roughly the same orientation across the entire radial range for the outer disk than for the center (except for NGC 4736).
5. Our gas flow maps indicate the presence of nested bars within larger bars for three out of seven galaxies (NGC 3368, NGC 3627, and NGC 4736) with offsets in the PAs of 25°–60° to the major axes of the large-scale bars.
6. No kinematic signs for unidentified nonaxisymmetric mass distributions (that are not evident in the NIR images) are found in the torque maps.
7. Noncircular motions seem to correlate only in a few cases with the torque-derived inflow/outflow as function of radius, and are thus not a reliable tracer of real in/outflow.
8. No correlation is found between the candidate radial flow regions from our kinematic study and the inflow/outflow caused by gravitational torques. This might be explained by the fact that the noncircular terms from our residual velocity field are predominantly caused by elliptical motions.
9. The change in flow direction of the gas caused by gravitational torques can be used to determine the CR radius

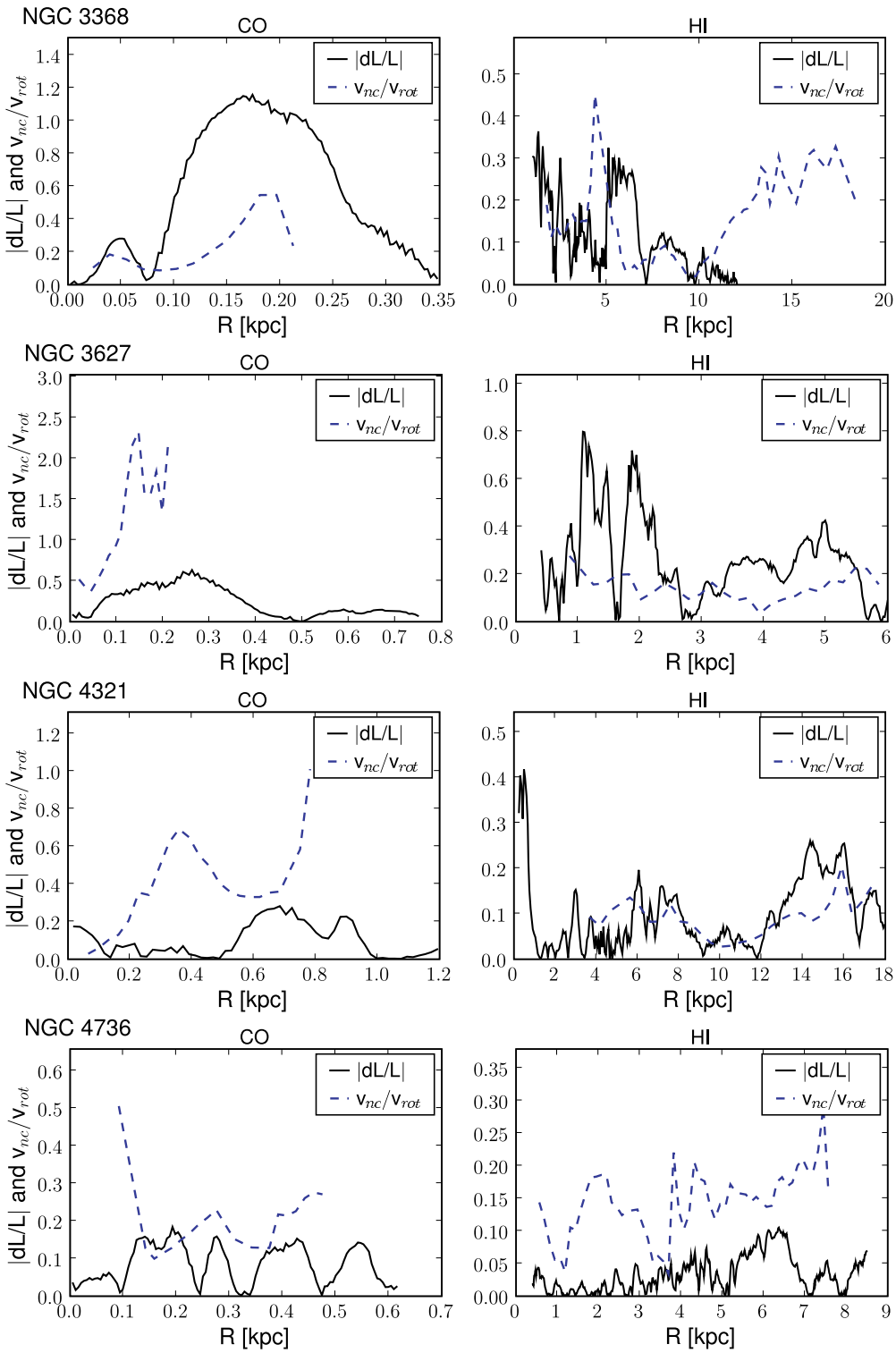

Figure 13. Comparison between the absolute value of angular momentum transport per rotation $|dL/L|$ derived from our torque analysis (see Section 4.4) with the fraction of noncircular to rotation velocity $v_{nc}/v_{\rm rot}$ from the harmonic decomposition of the velocity field (see Section 3.2). As noncircular motions are very likely dominated by elliptical streaming this comparison can be interpreted as elliptical streaming versus inflow/outflow as a function of radius. Values of $v_{nc}/v_{\rm rot}$ with error bars larger than three (two) times the median of the data set are not displayed for H I (CO).

(A color version of this figure is available in the online journal.)

similarly to other methods (Canzian, stellar density potential phase shift, bar length). In particular, this method may be applicable in case that several pattern speeds combine.

10. For the very center (0–0.1 kpc) no significant gas transport is found toward the AGN due to gravitational torques. Thus, other mechanisms such as viscous torques must be important for fueling the AGN at this scale.

The authors thank the anonymous referee for helpful comments. A special thanks goes to Anthony Baillard for providing

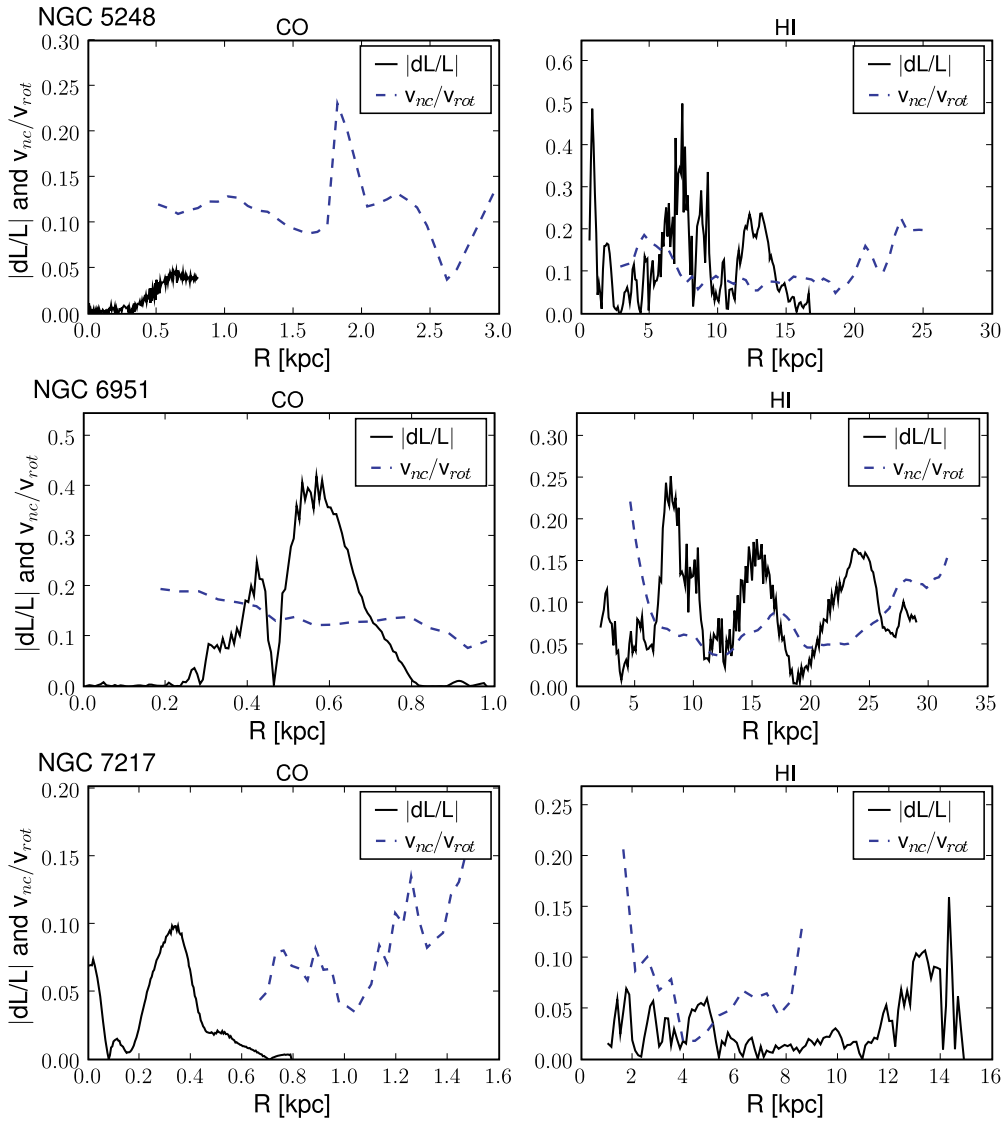

Figure 13. (Continued)

and assisting us with the tool NFIGI for the removal of foreground stars. We are grateful to the National Radio Astronomy Observatory (NRAO) for their support during this project. The NRAO is operated by Associated Universities, Inc., under cooperative agreement with the National Science Foundation. This work is also based on observations carried out with the IRAM Plateau de Bure Interferometer. IRAM is supported by INSU/CNRS (France), MPG (Germany) and IGN (Spain). CGM is grateful for financial support from the Royal Society and Research Councils U.K. SH is supported by the German DFG under grant number SCHI 536/2-1.

REFERENCES

Aaronson, M. 1977, PhD thesis, Harvard University
Athanassoula, E. 1992, MNRAS, 259, 345
Athanassoula, E. 2003, MNRAS, 341, 1179
Barnaby, D., & Thronson, H. A., Jr. 1992, AJ, 103, 41
Barnes, E. I., & Sellwood, J. A. 2003, AJ, 125, 1164
Beck, R. 2004, Ap&SS, 289, 293
Beck, R., Ehle, M., Shoutenkov, V., Shukurov, A., & Sokoloff, D. 1999, Nature, 397, 324
Begeman, K. G. 1989, A&A, 223, 47
Blitz, L. 1996, in IAU Sump. 170, CO: Twenty-Five Years of Millimeter-Wave Spectroscopy, ed. W. B. Latter et al. (Dordrecht: Kluwer), 11
Boone, F., et al. 2007, A&A, 471, 113
Canzian, B. 1993, ApJ, 414, 487
Canzian, B., & Allen, R. J. 1997, ApJ, 479, 723
Combes, F. 2001, in Advanced Lectures on the Starburst-AGN, ed. I. Aretxaga, D. Knuth, & R. Mujica (Singapore: World Scientific), 223
Combes, F. 2003, ASP Conf. Ser. 290, Active Galactic Nuclei: from Central Engine to Host Galaxy (San Francisco, CA: ASP), 411
Combes, F., et al. 2004, A&A, 414, 857
Dumas, G. 2007, PhD thesis, Astrophysics Research Institute Centre de Recherche Astrophysique de Lyon - Observatoire de Lyon
Dumas, G., Mundell, C. G., Emsellem, E., & Nagar, N. M. 2007, MNRAS, 379, 1249
Emsellem, E., Fathi, K., Wozniak, H., Ferruit, P., Mundell, C. G., & Schinnerer, E. 2006, MNRAS, 365, 367
Englmaier, P., & Shlosman, I. 2000, ApJ, 528, 677
Englmaier, P., & Shlosman, I. 2004, ApJ, 617, L115
Eskridge, P. B., et al. 2002, ApJS, 143, 73
Fathi, K. 2004, PhD thesis, Rijksuniversiteit Groningen
Franx, M., van Gorkom, J. H., & de Zeeuw, T. 1994, ApJ, 436, 642
Friedli, D., & Martinet, L. 1993, A&A, 277, 27
Garcia-Burillo, S., Combes, F., & Gerin, M. 1993, A&A, 274, 148
García-Burillo, S., Combes, F., Schinnerer, E., Boone, F., & Hunt, L. K. 2005, A&A, 441, 1011

García-Burillo, S., Sempere, M. J., Combes, F., Hunt, L. K., & Neri, R. 2000, A&A, 363, 869
García-Burillo, S., et al. 2003, in ASP Conf. Ser. 290, Active Galactic Nuclei: From Central Engine to Host Galaxy (San Francisco, CA: ASP), 423
Greisen, E. W. 2003, in Information Handling in Astronomy - Historical Vistas, ed. A. Heck (Dordrecht: Kluwer), 109
Haan, S., Schinnerer, E., Mundell, C. G., García-Burillo, S., & Combes, F. 2008, AJ, 135, 232
Helfer, T. T., Thornley, M. D., Regan, M. W., Wong, T., Sheth, K., Vogel, S. N., Blitz, L., & Bock, D. C.-J. 2003, ApJS, 145, 259
Heller, C. H., & Shlosman, I. 1994, ApJ, 424, 84
Heller, C., Shlosman, I., & Englmaier, P. 2001, ApJ, 553, 661
Ho, L. C., Filippenko, A. V., & Sargent, W. L. W. 1997, ApJ, 487, 579
Hunt, L. K., et al. 2008, A&A, 482, 133
Jogee, S. 2006, in Physics of Active Galactic Nuclei at all Scales, ed. D. Alloin, R. Johnson, & P. Lira (Berlin: Springer), 143
Jogee, S., Knapen, J. H., Laine, S., Shlosman, I., Scoville, N. Z., & Englmaier, P. 2002, ApJ, 570, L55
Jogee, S., Scoville, N., & Kenney, J. D. P. 2005, ApJ, 630, 837
Jogee, S., Shlosman, I., Laine, S., Englmaier, P., Knapen, J. H., Scoville, N., & Wilson, C. D. 2002, ApJ, 575, 156
Junqueira, S., & Combes, F. 1996, A&A, 312, 703
Kewley, L. J., Groves, B., Kauffmann, G., & Heckman, T. 2006, MNRAS, 372, 961
Knapen, J. H. 2005, in AIP Conf. Proc. 783, The Evolution of Starbursts, ed. S. Hüttenmeister (Berlin: Springer), 171
Knapen, J. H., Beckman, J. E., Heller, C. H., Shlosman, I., & de Jong, R. S. 1995b, ApJ, 454, 623
Knapen, J. H., Beckman, J. E., Shlosman, I., Peletier, R. F., Heller, C. H., & de Jong, R. S. 1995a, ApJ, 443, L73
Knapen, J. H., de Jong, R. S., Stedman, S., & Bramich, D. M. 2003, MNRAS, 346, 333
Knapen, J. H., Shlosman, I., & Peletier, R. F. 2000, ApJ, 529, 93
Krajnović, D., Cappellari, M., de Zeeuw, P. T., & Copin, Y. 2006, MNRAS, 366, 787
Laine, S., Shlosman, I., Knapen, J. H., & Peletier, R. F. 2002, ApJ, 567, 97
Lindt-Krieg, E., Eckart, A., Neri, R., Krips, M., Pott, J.-U., García-Burillo, S., & Combes, F. 2008, A&A, 479, 377
Lynden Bell, D. 1969, Nature, 223, 690
Lynden Bell, D., & Kalnajs, A. J. 1972, MNRAS, 157, 1
Maciejewski, W. 2002, Ap&SS, 281, 325
Maciejewski, W. 2004a, MNRAS, 354, 883
Maciejewski, W. 2004b, MNRAS, 354, 892
Maciejewski, W., & Sparke, L. S. 2000, MNRAS, 313, 745
Martini, P., & Pogge, R. W. 1999, AJ, 118, 2646
Martini, P., Regan, M. W., Mulchaey, J. S., & Pogge, R. W. 2003, ApJ, 589, 774
Mulchaey, J. S., Regan, M. W., & Kundu, A. 1997, ApJS, 110, 299
Mundell, C. G., & Shone, D. L. 1999, MNRAS, 304, 475
Mundell, C. G., et al. 2007, New Astron. Rev., 51, 34
Quillen, A. C., Frogel, J. A., & Gonzalez, R. A. 1994, ApJ, 437, 162
Quillen, A. C., Frogel, J. A., Kenney, J. D. P., Pogge, R. W., & Depoy, D. L. 1995, ApJ, 441, 549
Rautiainen, P., Salo, H., & Laurikainen, E. 2008, MNRAS, 388, 1803
Rees, M. J. 1984, ARA&A, 22, 471
Schinnerer, E., Böker, T., Emsellem, E., & Lisenfeld, U. 2006, ApJ, 649, 181
Schinnerer, E., Eckart, A., Tacconi, L. J., Genzel, R., & Downes, D. 2000, ApJ, 533, 850
Schoenmakers, R. H. M., Franx, M., & de Zeeuw, P. T. 1997, MNRAS, 292, 349
Schoenmakers, R. H. M. 1999, PhD thesis, Rijksuniversiteit Groningen
Shlosman, I. 2003, Active Galactic Nuclei: From Central Engine to Host Galaxy, Vol. 290, 427
Shlosman, I., Begelman, M. C., & Frank, J. 1990, Nature, 345, 679
Shlosman, I., Frank, J., & Begelman, M. C. 1989, Nature, 338, 45
Shlosman, I., & Heller, C. H. 2002, ApJ, 565, 921
Shlosman, I., & Noguchi, M. 1993, ApJ, 414, 474
Shu, F. H., Tremaine, S., Adams, F. C., & Ruden, S. P. 1990, ApJ, 358, 495
Simões Lopes, R. D., Storchi-Bergmann, T., de Fátima Saraiva, M., & Martini, P. 2007, ApJ, 655, 718
Sparke, L. S., & Sellwood, J. A. 1987, MNRAS, 225, 653
Spekkens, K., & Sellwood, J. A. 2007, ApJ, 664, 204
Solomon, P. M., & Barrett, J. W. 1991, Dynamics of Galaxies and Their Molecular Cloud Distributions, Vol. 146, 235
Trachternach, C., de Blok, W. J. G., Walter, F., Brinks, E., & Kennicutt, R. C., Jr. 2009, AJ, 136, 2720
van der Hulst, J. M., Terlouw, J. P., Begeman, K. G., Zwitser, W., & Roelfsema, P. R. 1992, in APS Conf. Ser. 25, Astronomical Data Analysis Software and Systems I, ed. D. M. Worrall, C. Biemesderfer, & J. Barnes (San Francisco, CA: ASP), 131
van der Kruit, P. C., & Searle, L. 1982, A&A, 110, 61
van der Kruit, P. C., & Searle, L. 1982, A&A, 110, 79
Wada, K., & Koda, J. 2004, MNRAS, 349, 270
Wainscoat, R. J., Freeman, K. C., & Hyland, A. R. 1989, ApJ, 337, 163
Walter, F., Brinks, E., de Blok, W. J. G., Bigiel, F., Kennicutt, R. C., Jr., Thornley, M. D., & Leroy, A. 2008, AJ, 136, 2563
Wong, T., Blitz, L., & Bosma, A. 2004, ApJ, 605, 183
Young, J. S., & Scoville, N. Z. 1991, ARA&A, 29, 581
Zhang, X. 1996, ApJ, 457, 125
Zhang, X., & Buta, R. J. 2007, AJ, 133, 2584
Zhang, X., Wright, M., & Alexander, P. 1993, ApJ, 418, 100